



Western Michigan University  
ScholarWorks at WMU

---

Dissertations

Graduate College

---

12-2018

## Assessing Land Deformation and Sea Encroachment in the Nile Delta: A Radar Interferometric and Modeling Approach

Esayas Gebrekidan Gebremichael  
Western Michigan University, esagkn@gmail.com

Follow this and additional works at: <https://scholarworks.wmich.edu/dissertations>



Part of the Geology Commons

---

### Recommended Citation

Gebremichael, Esayas Gebrekidan, "Assessing Land Deformation and Sea Encroachment in the Nile Delta: A Radar Interferometric and Modeling Approach" (2018). *Dissertations*. 3371.  
<https://scholarworks.wmich.edu/dissertations/3371>

This Dissertation-Open Access is brought to you for free and open access by the Graduate College at ScholarWorks at WMU. It has been accepted for inclusion in Dissertations by an authorized administrator of ScholarWorks at WMU. For more information, please contact [wmu-scholarworks@wmich.edu](mailto:wmu-scholarworks@wmich.edu).



ASSESSING LAND DEFORMATION AND SEA ENCROACHMENT IN THE NILE  
DELTA: A RADAR INTERFEROMETRIC AND MODELING APPROACH

by

Esayas Gebrekidan Gebremichael

A dissertation submitted to the Graduate College  
in partial fulfillment of the requirements  
for the degree of Doctor of Philosophy  
Geosciences  
Western Michigan University  
December 2018

Doctoral Committee:

Mohamed Sultan, Ph.D., Chair  
Alan Kehew, Ph.D.  
Michelle Kominz, Ph.D.  
Richard Becker, Ph.D.

Copyright by  
Esayas Gebrekidan Gebremichael  
2018

## ACKNOWLEDGMENTS

First and foremost, I would like to thank God for all the blessings in my life and for giving me the strength and patience to successfully complete my study.

I would like to extend my utmost and sincere gratitude to my advisor Dr. Mohamed Sultan for all his guidance, encouragement, and relentless support throughout my study at Western Michigan University. I am very grateful to Dr. Richard Becker for his suggestions, advice, and recommendations to make this research a success. I also would like to thank my committee members, Dr. Alan Kehew and Dr. Michelle Kominz, for their support in this research and throughout my time as a graduate student at Western Michigan University.

This research was supported by the U.S.–Egypt Science and Technology (S&T) Joint Fund from the US Agency for International Development and administered by the National Science Foundation (Award Number: 1103843). I would like to thank the European Space Agency for providing the Envisat ASAR scenes (Project ID: C1F.12455), the German Aerospace Center for the TanDEM-X digital elevation model (Proposal ID: DEM\_HYDR0540), and the Nevada Geodetic Laboratory and SONEL data assembly center for the GPS data.

## Acknowledgement - Continued

Last, but certainly not least, I would like to express my heartfelt thanks to my wife Tsion, our daughter Abigail, other family members and friends, and to my colleagues and friends at the ESRS lab for their exceptional support and patience.

Esayas Gebrekidan Gebremichael

# ASSESSING LAND DEFORMATION AND SEA ENCROACHMENT IN THE NILE DELTA: A RADAR INTERFEROMETRIC AND MODELLING APPROACH

Esayas Gebrekidan Gebremichael, Ph.D.

Western Michigan University, 2018

Many of the deltas of the world are experiencing land deformation, subsidence or uplift of landmass, due to natural or anthropogenic causes, or a combination of both processes and causes. These deltaic settings are densely populated and border some of our world's largest water bodies (oceans and seas). The land deformation, especially the subsidence component, when combined with the climate change-induced sea level rise, coastal erosion, and other anthropogenic drivers, will undoubtedly impact the population and economy of coastal areas of deltas. For the Nile Delta of Egypt, the land deformation processes and the factors that control the deformation processes were investigated using an integrated approach (remote sensing, geology, hydrogeology, and geodesy). Moreover, the impact of sea level rise and land deformation on the coastal areas and communities was assessed by simulating sea encroachment scenario and measuring ongoing deformation.

Persistent scatterer interferometric analyses were conducted on a stack of 84 Envisat ASAR scenes spanning 7 years (2004 to 2010) over the entire Nile Delta of Egypt and surroundings (area: 40,416 km<sup>2</sup>) to monitor the ongoing spatial and temporal land deformation, identify the factors controlling the deformation, and model the interplay between sea level rise

and land subsidence to identify areas and populations threatened by sea encroachment by the end of the 21<sup>st</sup> century. Findings include: (a) general patterns of subsidence (average rate:  $-2.4$  mm/yr) in the northern delta, near-steady to slight subsidence in the southern delta (average rate:  $0.4$  mm/yr), separated by a previously mapped flexure zone (minimum width:  $20\text{--}40$  km) undergoing uplift (average rate:  $2.5$  mm/yr); (b) high subsidence rates (up to  $-8.9$  mm/yr) over the north-central and northeastern delta (area:  $\sim 4815$  km<sup>2</sup>), possibly due to compaction of recent ( $<3500$  years old), thick ( $>5$ m) silt and clay-rich Holocene sediments; (c) the terminus and bifurcation points of the now defunct distributaries of the Nile where thick accumulation of compressible sediments are anticipated also show high subsidence rates (up to  $-7.8$  mm/yr); the paleo-distributaries were delineated using high-resolution digital elevation model ( $10$  m horizontal resolution) extracted from  $195$  high-resolution ( $1:25,000$  scale;  $0.5$  m contour interval) topographic map sheets, ; (d) high subsidence rates (up to  $-9.7$  mm/yr) in areas where the highest groundwater extraction rates were reported in southern delta (Menoufia governorate) and in reclaimed desert land in the western delta (Beheira governorate); (e) high subsidence rates (up to  $-9.7$  mm/yr) over onshore gas fields, notably the Abu Madi gas field, where high gas extraction rates have been recorded; (f) using extracted deformation rates, high-resolution TanDEM-X digital elevation model, a eustatic sea level rise of  $0.4$  m, and applying a bathtub inundation model, an estimated  $2660$  km<sup>2</sup> in northern delta will be inundated by year  $2100$ .

## TABLE OF CONTENTS

ACKNOWLEDGMENTS .....	ii
LIST OF TABLES .....	vi
LIST OF FIGURES .....	vii
CHAPTER	
1. INTRODUCTION .....	1
1.1. Dissertation Roadmap.....	1
1.2. River Deltas .....	3
1.3. The Nile Delta.....	5
1.4. Geological History of the Nile Delta .....	6
1.4.1 Eonile Phase.....	7
1.4.2 Paleonile Phase .....	8
1.4.3 Protonile Phase.....	9
1.4.4 Prenile Phase.....	9
1.4.5 Neonile Phase.....	10
1.5. Hydrogeology of the Nile Delta.....	12
1.5.1 Nile Delta Aquifer.....	12
1.5.2 Coastal Aquifer .....	12
1.5.3 Moghra Aquifer .....	12
1.5.4 Fissured Carbonate Aquifer .....	13
1.6. Statement of the Problem.....	14
2. LAND DEFORMATION AND SEA ENCROACHMENT IN DELTAS: APPROACHES, RESULTS, AND LIMITATIONS .....	16



## Table of Contents - Continued

### CHAPTER

2.1	Introduction.....	16
2.2	Land Deformation in Deltas: Methods, Results, and Limitations .....	16
2.3	Sea Encroachment on Coastal Areas in Deltas: Approaches, Results, and Limitations .....	19
2.4	Objectives of the Research and Approaches.....	21
3.	DATA AND METHODS.....	23
3.1.	Introduction.....	23
3.2.	Land Deformation Analysis.....	23
3.3.	Mapping Paleochannels .....	43
3.4.	Impact of Sea Level Rise on Coastal Areas and Communities .....	45
4.	RESULTS AND DISCUSSION .....	51
4.1	Introduction.....	51
4.2	Paleochannel Delineation using High-Resolution DEM .....	51
4.3	Land Deformation Processes and Controlling Factors .....	54
4.3.1	Regional Deformational Patterns Caused by Natural Processes.....	55
4.3.2	Local Deformational Patterns Caused by Anthropogenic Factors.....	64
4.4	Sea Level Rise .....	67
5.	MODEL EVALUATION AND LIMITATIONS .....	74
5.1	Introduction.....	74
5.2	Model Evaluation, Limitations, and Assumptions.....	74
6.	CONCLUSIONS AND FUTURE DIRECTIONS.....	78
7.	REFERENCES.....	81

## LIST OF TABLES

1. The five main Nile River phases and other events that shaped the Nile River and the formation of the Nile Delta (Said, 1993).....8
2. The estimated areal extent of the projected inundated areas in the Nile Delta throughout the investigated period (2010 – 2100) using a bathtub model and decadal time steps. .... 73

## LIST OF FIGURES

1. Location map of the Nile Delta including the two current active branches of the Nile River (Rosetta and Damietta) and other major water bodies (Lake Manzala and Burullus), and the flanking eastern and western deserts. The inset shows the location of the Nile Delta (outlined by white box) within Egypt. ....	7
2. Geologic map for the Nile Delta and surroundings (modified from El Bastawesy et al. 2016) showing the distribution of the Quaternary sediments within the Nile Delta, and older Tertiary deposits on its margins (in the Eastern and Western deserts).....	10
3. Main aquifer systems in Egypt (Abdel-Shafy and Kamel, 2016).....	13
4. Overview of past, current, and future spaceborne SAR missions (UNAVCO, 2018).....	25
5. A summary sketch of repeat-pass (shown as 1 <sup>st</sup> pass and 2 <sup>nd</sup> pass data acquisition times on the sketch) InSAR technique (also known as Differential SAR Interferometry (DInSAR) showing how deformation estimates are calculated after a major (e.g., earthquake) land deforming event (Garthwaite et al., 2015). ....	26
6. Environmental Satellite (Envisat) SAR image of the northern Nile Delta region. Urban areas appear bright as a result of high backscatter signal while vegetated areas and water bodies (Lake Manzala and the Mediterranean Sea) appear in moderate to dark black color due to poor backscatter return.....	27
7. SAR interferometric imaging geometry (Jung et al., 2014) .....	28
8. SAR image coregistration procedure (Zou et al., 2009).....	30
9. A wrapped complex interferogram of the April 6, 2009, L'Aquila earthquake (central Italy) event produced from interferometric analysis of two (repeat-pass) Envisat ASAR images acquired before (February 2, 2009) and after (April 12, 2009) the event. Each pixel contains the difference (in phase value) between the phases of the two Envisat ASAR images. The interferogram product was generated using the Delft Object-oriented Radar Interferometric (DORIS) software (Kampes, 1999). ....	32

## List of Figures—Continued

10. A wrapped interferogram (in radar geometry) of the April 6, 2009, L'Aquila earthquake event after the removal of phase contributions from different sources (e.g.  $\phi_{noise}$ ,  $\phi_{topography}$ ). A maximum deformation of nearly 23 cm (shown in white box) along the satellite's line of sight is calculated from this product. .... 33
11. Optical Imagery portraying the atmospheric conditions at the time of Envisat ASAR image acquisition. The imagery was acquired by the Medium Resolution Imaging Spectrometer (MERIS) sensor which is one of the sensors onboard of the Envisat satellite. Figure (a) shows a stable (less convective) troposphere (cloud) state of the atmosphere while the ASAR imagery was acquired. Figure (b) shows cloudy atmospheric conditions at the time of ASAR image acquisition. .... 34
12. A cartoon depicting the variation in phase response from (a) distributed scatterer pixel, and (b) a persistent scatterer pixel. Different image acquisitions from different orbit tracks produce an erratic phase response (bottom figure in (a)). A dominant single persistent scatterer, on the other hand, produces a stable phase response under varying conditions (Hooper, 2006). .... 35
13. (a) Nile Delta and surrounding regions with the footprints of the descending satellite tracks that cover the study area (b) Spatial baseline–time plot for the descending tracks 479, used in this study. Master scenes are shown in red dots while other SAR images are shown in dark blue color. (c) Same as (b) above, but for track 207. (d) Same as (b) above, but for track 436..... 38
14. Persistent Scatterer Interferometry data processing flowchart (Hooper et al., 2004; Yokha et al., 2015) ..... 40
15. Time series showing nearly 6 years (2002-2008) daily vertical component ground motion at ALEX GPS station in Alexandria (The weekly averaged deformation rate is  $0.05 \pm 0.28$  mm/yr)..... 42
16. The positions of the distributaries of earlier and current Nile river branches in the Nile Delta as per the historical versions (maps) given by Herodotus (484 - 425 B.C.), Strabo (63 B.C. – 24 A.D), Ptolemy (90 – 168 A.D.), Serapion (350 A.D.), and El-Idrisi (1099 - 1154 A.D.) (Stanley et al., 2004; Toussoun, 1922). .... 44
17. Global mean sea level rise projections through the year 2100 (Church et al., 2013) using the four Representative Concentration Pathway (RCP) model scenarios (RCP 2.6, RCP 4.5, RCP 6.0, and RCP 8.5). The highest mean sea

## List of Figures—Continued

- level rise values by the end of the 21<sup>st</sup> century were projected by the RCP 2.8 model (0.74 m) followed by RCP 6.0 (0.55 m), RCP 4.5 (0.53 m), and RCP 2.6 (0.44 m). ..... 45
18. (a) Spatial distribution of the 50 benchmark (BM) elevation points, extracted from 1941–1946 topographic maps (War Office, 1941; Egyptian Surveying Authority, 1946), plotted on a TanDEM-X digital elevation model and used for its validation and calibration. (b) A plot of fifty TanDEM-X elevation points versus benchmark elevation points showing good correlations ( $R^2 = 0.99$ ) between the two datasets and slightly lower elevations (by 4.5 cm) for the TanDEM-X data. .... 48
19. Population density estimates of the Nile Delta and surroundings from the Gridded Population data of the world ([GPWv4]; CIESIN, 2016)). The coastal cities of Alexandria, Damietta and Port Said are densely populated cities in the northern part of the study region. On the southern and central Nile Delta, dense population distribution is noted in El Mansura, Tanta, and Cairo cities. .... 50
20. Paleochannel distribution extracted from the generated DEM (shown in blue color). The dotted light blue color represents the currently active branches of the Nile (Rosetta and Damietta). The white circles are representative of the terminus of the branches of the Nile distributaries where thick accumulations of sediments are anticipated. Also shown (in pink boxes) are some of the bifurcation points emanating from the main distributaries of the Nile..... 54
21. (a) Vertical component land deformation (in mm/yr) for the Nile Delta and surroundings extracted from 84 Envisat ASAR scenes acquired (2004–2010) along 3 tracks. Negative deformation values represent downward motion (subsidence), whereas positive deformation values represent upward motion (uplift). High uplift rates correlate with the distribution of a flexure zone in central delta, whereas high subsidence rates correlate with the distribution of young, thick, clay-dominated Holocene deposits and with areas experiencing high groundwater, oil, and gas withdrawal. The spatial distribution of the currently active and defunct Nile River branches (after Wright and Coleman, 1973; Ross et al., 1978) is also shown. Interpolated distribution of total thickness of Holocene sediments (b), cumulative thickness of sand (c), silt and mud (d), and clay (e) deposits in Holocene core samples (after Stanley et al., 1996) respectively..... 56
22. X-Y plot for distance versus deformation rates (extracted from the PSI analysis) along two north-south trending profiles (A-A' and B-B') showing the uplift and subsidence deformation patterns associated with flexural isostatic

## List of Figures—Continued

deformation. A hinge line (a) separates the oceanic crust (c) from the passive continental margin (d). The subsiding oceanic crust is flanked by the flexure zone (b), an uplifting stretch of land with a minimum width of 20–40 km.....	58
23. GPS based velocity (in mm/yr) plot of the Jackson to New Orleans profile using elevation changes determined by comparing the GPS data for time interval 1934 to 1969 (Jurkowski et al., 1984). .....	59
24. The effect of progressive sediment loading at a continental margin. The increasing sediment load at the margin eventually produces a downwarp by flexure (Walcott, 1972).....	60
25. Natural gas withdrawal within the Nile Delta and off its shoreline over the past two decades (U.S. Energy Information Administration, 2014). .....	66
26. (a) The projected distribution of inundated areas (light blue colored areas) in the Nile Delta by the year 2100. The simulation is based on the RCP 2.6 model eustatic sea level rise projections and the extracted PSI-based deformation rates. (b) Social and economic impact of the sea encroachment is based on the land cover and population density datasets of the Nile Delta. The extent of the encroachment is shown in light yellow. ....	68
27. Sea encroachment in the Nile Delta (inundated areas are shown in blue color) calculated using 1 m relative sea level rise projection by the year 2100 (after Hereher, 2010). .....	69
28. Major morphologic units on the coast of the Nile Delta (Frihy et al. 2003, 2010).....	71
29. Protective sea wall with elevations of more than 2 m constructed at the Damietta promontory (Hereher, 2009). .....	72
30. East-west trending profiles showing a smooth and uninterrupted transition in deformation signal across adjacent Envisat scene tracks. (a) Tracks 479 and 207. (b) Tracks 207 and 436. The locations of the profiles are plotted on Fig. 13. ....	76

## CHAPTER 1

### INTRODUCTION

#### **1.1. Dissertation Roadmap**

This work investigates the land deformation processes and their controlling factors in river deltas using the Nile Delta of Egypt as a test site. The impact of sea level rise on the coastal areas and communities was also investigated using a combination of measured land deformation across the Nile Delta, and sea encroachment simulations. The study integrates a wide variety of datasets, techniques, and models including remote sensing, geology, hydrogeology, geographic Information system (GIS), land use and land cover, geodesy, and other relevant data. The present study reviews previous studies in land deformation processes and interrelated sea level rise impact on coastal communities in river deltas in general and the Nile Delta in particular. It points out possible limitations in the earlier approaches and applies new methodologies and approaches to tackle the research problem.

The present study is divided into six main chapters. Chapter 1 (this chapter) provides a brief summary of land deformation processes and sea encroachment problems in deltas worldwide with a special focus on the Nile Delta. Moreover, the geological and hydrogeological settings of the Nile Delta and surroundings are also described in detail. The problem statements that initiated the present research are also stated.

Chapter 2 discusses the approaches, results, and limitations of previous land deformation and sea encroachment studies in deltas worldwide including the Nile Delta of Egypt. Two main methods that are commonly used for investigating land deformation processes, age-depth relationships that are based on radiocarbon dating of organic deposits and radar remote sensing techniques, are discussed in detail in this chapter. Previous sea encroachment studies in deltas, the type of data used, the results obtained, and their limitations are also discussed in chapter 2. The detailed objectives of the present study and the approaches used to respond to the research problems are stated in this chapter.

Chapter 3 is allotted for the detailed description of the approach and datasets used for the land deformation studies of the Nile Delta using radar remote sensing technique. The delineation approaches and procedures of the now-defunct distributaries of the Nile River that have wide implications in terms of portraying the spatial distribution of sediments that control the deformation processes in the Nile Delta are explained in this chapter. The approach and datasets used to assess the impact of sea level rise on the coastal areas and communities of the Nile Delta are also explained in this chapter.

Chapter 4 discusses the results of the present study. The findings of each of the approaches used in the present study are explained in three subsections of the chapter. The evaluations and limitations of the present study are discussed in Chapter



5. The final chapter provides a summary of the findings of the present study and recommendations for future investigations in the Nile Delta.

## **1.2. River Deltas**

A river delta is a landform formed at the mouth of a river through a long-term deposition and aggradation of sediments brought by a river as it flows into other water bodies or land surfaces (Likens, 2010). The deceleration of the Holocene sea level rise initiated the formation of modern deltas 8500 and 6500 years ago. During this time, the rate of accumulation of fluvial sediments surpassed the rate of sea level decline and this eventually led to the formation of modern river deltas (Stanley and Warne, 1994).

Deltas are classified into three types depending on the dominant process that control the sediment distribution and surface geomorphology. These are river-, wave-, and tide-dominated delta systems, or others that exhibit a combination of the main processes (Galloway, 1975).

The deposition of deltaic sediments in river deltas is controlled by a combination of sediment supply (drainage characteristics, water discharge, and sediment load), the generation of accommodation space that is controlled by factors such as variations in sea level, tectonic processes, and coastal processes such as

waves and tides (Coleman and Wright, 1975; Orton and Reading 1993; Postma, 1995).

Deltas have been undergoing deformation for thousands of years due to sediment accumulation and compaction (Stanley, 1997; Törnqvist et al., 2008), isostatic lowering (Stanley, 1997; Syvitski, 2008), tectonics (Dokka, 2006), and more recently, due to anthropogenic interventions (Stanley and Warne, 1993; Carminati and Di Donato, 1999; Syvitski, 2008; Syvitski et al., 2009). The latter includes: (1) the construction of dams and reservoirs that impound sediments upstream and decrease sediment loads reaching deltas and coastal areas of the world by as much as  $1.4 \pm 0.3$  billion metric tons/yr (Syvitski et al., 2005), sediments that could have compensated in part for the subsidence, and (2) the extraction of groundwater and hydrocarbons that can increase natural deformation rates by up to an order of magnitude (Meckel et al., 2007; Syvitski, 2008).

Deltas are one of Earth's most densely populated landforms, where close to a billion citizens live, exploit their natural resources (i.e., water, vegetative cover, oil, and gas; Syvitski et al., 2009), and modify the landscape (Waltham, 2002; Erkens et al., 2015). Like most deltas of the world, the Nile Delta of Egypt is an overpopulated area, experiencing natural and anthropogenic land deformation, and its coastal areas could potentially face serious sea encroachment problems.

### **1.3. The Nile Delta**

The Nile Delta (Fig. 1, area:  $>20,000 \text{ km}^2$ ; Stanley, 2003) was formed by continuous accretion of alluvial sediments transported by distributaries of the modern Nile River during the Holocene (Sneh et al., 1986; Coutellier and Stanley, 1987; Said, 1993; Stanley, 2005), many of which were silted in, leaving the Rosetta and Damietta branches (thick blue color: Fig. 1) as the only currently active branches (Fanous et al., 1995). The two currently active branches of the Nile River have formed promontories at the terminus of the Rosetta and Damietta.

The Nile Delta is bounded by the Eastern Desert in the east, the Western Deserts on the western side, and by a stretch (225 kilometers long) of coastline along the Mediterranean Sea in the north (Fig. 1). The Nile Delta is a wave-dominated delta, where coastal currents along the northwest delta erode and deposit sediments eastward, and its shorelines portray smooth and gentle form (Nafaa and Frihy, 1993; Stanley et al., 2004). Highly populated cities such as Alexandria, Damietta, and Port Said lie on, or near, the Nile Delta coast (El Raey, 2011). During the past 5000 years, the Nile Delta coastal margin has moved northwards by as much as 50 kilometers (Stanley and Warne, 1994).

#### **1.4. Geological History of the Nile Delta**

The formation of the Nile Delta and its stratigraphy reflect the collective impacts of fluvial processes, tectonic activities, and changes in the Mediterranean Sea levels (Said, 1981). The northern and southern parts of the Nile Delta are separated by a broad (width: 4 to 8 km) series of east-west trending step faults (Harms and Wray, 1990; Stanley and Clemente, 2017) ,“hinge line”, that represents the northern termination of the pre-Miocene stable carbonate shelf onto which the recent post-Miocene deposits prograded (Harms and Wray, 1990).

Five main successive phases of the Nile River (Table 1), namely the Eonile (Miocene), Paleonile (Pliocene), Protonile (Early Pleistocene), Prenile (Middle Pleistocene), and Neonile (Holocene), resulted in the deposition of fluvial sediments that make up the Nile Delta (Said, 1993).

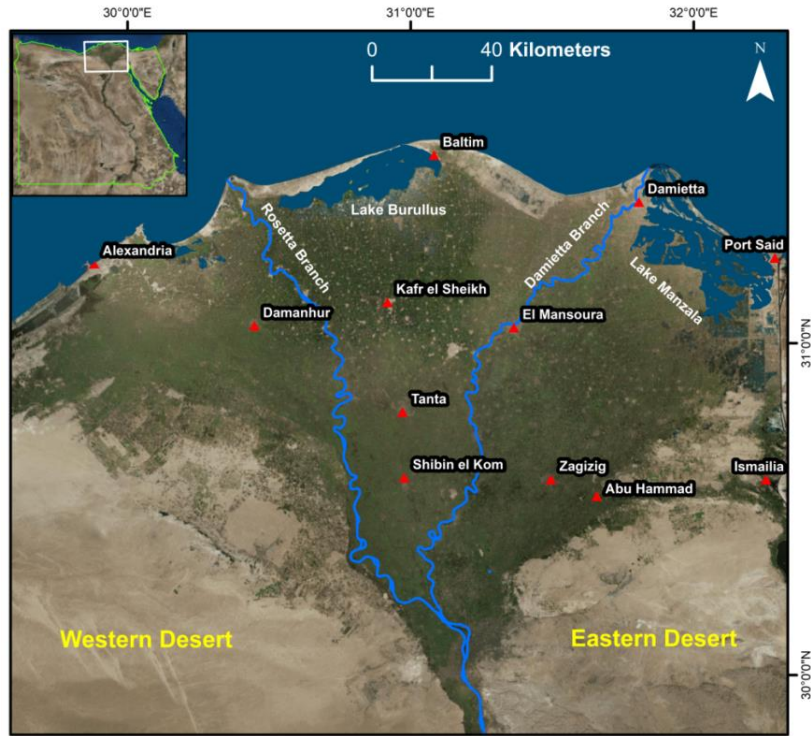


Figure 1: Location map of the Nile Delta including the two current active branches of the Nile River (Rosetta and Damietta) and other major water bodies (Lake Manzala and Burullus), and the flanking eastern and western deserts. The inset shows the location of the Nile Delta (outlined by white box) within Egypt.

#### 1.4.1 Eonile Phase

During the Eonile phase (Miocene), a deep canyon was carved beneath the modern Nile River (Roden et al., 2011). During the early Pliocene, the Eonile canyon was filled by water as a result of the rise of the Mediterranean Sea. Sandstones and limestones of the Moghra Formation were deposited during the Lower Miocene followed by the deep-marine shales of the Sidi Salem Formation (Middle-Upper Miocene). The sandstone and shale dominated Abu Madi Formation (Upper Miocene)

unconformably overlies the Sidi Salem Formation (Rizzini et al., 1978; Said, 1993; Salem et al., 2005; Tawadros, 2012).

Table 1: The five main Nile River phases and other events that shaped the Nile River and the formation of the Nile Delta (Said, 1993)

Dates (in thousand years)	River	Events
6000 – 5400	Eonile	Nile canyon forms in response to a desiccated Mediterranean.
5400 – 3300	Gulf Phase	Rising waters of the regenerated Mediterranean fill the canyon converting it into a gulf
3300 – 1800	Paleonile	Local river occupies the gulf & fills the valley with sediments
1800 – 800	Desert Phase	Egypt converted into a desert. River stops flowing
800 – 400	Prenile	First Egyptian river with an African connection established. River exceedingly competent.
400 – present	Neonile	A less competent river with an African connection dominates the scene. Ebbs & flows many times. The first (or alpha Neonile) interrupts a wet phase (400,000 – 200,000 years) followed by an erratic Nile (200,000 – 70,000 years), and then by the seasonal beta and gamma Neoniles (70,000 – 12,000 years) and finally by the modern perennial Nile (12,000 – present).

#### 1.4.2 Paleonile Phase

Towards late Pliocene, the sea retreated and the Paleonile started its northward flow from its vegetated source areas in Sudan. By the end of the Paleonile phase the Eonile canyon was filled and the morphology of the delta changed to one that is flat and sloping to the north. More sediments were deposited in the Delta during this

phase than those contributed throughout the other stages of the Nile (Rzóska, 1976). The Paleonile deposits are primarily dominated by claystone and shale belonging to the Kafr El Sheikh Formation (Said, 1981; Tawadros, 2012).

#### **1.4.3 Protonile Phase**

The beginning of the Pleistocene is marked by prolonged arid climatic conditions followed by wet pluvial periods that developed into a highly competent river (the Protonile). In the Nile Delta, Early Pleistocene sediments of the Protonile phase are composed of thick sand beds interbedded with thin clays of the El Wastani Formation (Said, 1981; Rizzini et al., 1978).

#### **1.4.4 Prenile Phase**

Around 800,000 - 700,000 years ago, a new drainage pattern developed as a result of the connection of the Nile with Ethiopian Highlights that led to the development of the Prenile. The Prenile deposited extensive successions that make up the Mit Ghamr Formation in the delta, on its floodplains, and along its margins (Said, 1993). The Mit Ghamr formation is a late Pliocene to early Pleistocene deposit dominated by sand and gravel interbedded with thin clay layers (Rizzini et al., 1978; Taniguchi and Holman, 2010). The distribution of the sediments during the Prenile outlines the modern morphology of the Nile Delta (Said, 1993).

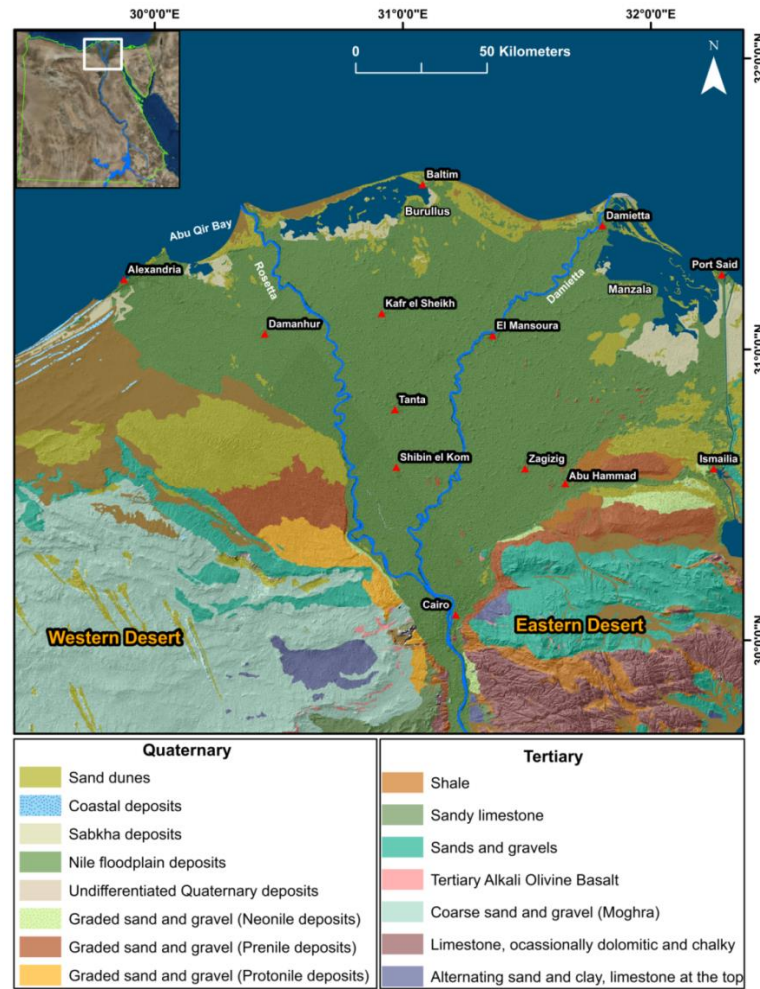


Figure 2: Geologic map of the Nile Delta and surroundings (modified from El Bastawesy et al. 2016) showing the distribution of the Quaternary sediments within the Nile Delta, and older Tertiary deposits on its margins (in the Eastern and Western deserts).

#### 1.4.5 Neonile Phase

The Neonile developed after the cessation of the flow of the Prenile some 400,000 years ago. During this phase, the connection of the Nile with the upstream (African) sources was intermittent. The Neonile went through three major phases



during its evolution. In the earliest phase, the connection of the Nile with the African sources was interrupted and the only source of water for the Nile was the episodic river systems fed by local rains. In the second phase of the Neonile phase, a weak connection with the African highlands was re-established and the poor and erratic flow coming from the African connection was supplemented by local winter rains (Said, 1993). The third and final phase of the Neonile started some 70,000 years ago and still continues to this day. This phase occurred largely during a glacial period (70,000 – 12,000 years before present). During this period weak seasonal rivers from the Ethiopian Highland sources fed the Nile with water and towards its end (20,000 – 12,000 years before present), the ice sheets retreated. The latter time was period of increasing rainfall and led to the rise of the Equatorial lakes and eventually resulted in the flow of excess water to the Nile drainage system. The modern Nile evolved some 10,000 years ago (Holocene) with the return of rain to the Ethiopian Highland and the Equatorial Lake Plateau sources (Said, 1993).

The surficial geology of the floodplains of the Nile Delta and Nile Valley is dominated by the Neonile deposited Bilqas Formation (late Neonile). The Bilqas formation consists of medium- to fine-grained Holocene sand, silt, and clays with minor peat deposits (Said, 1981; 1990; Stanley, 2005). The surficial geology of the Nile Delta and surroundings is shown in figure 2.

## **1.5. Hydrogeology of the Nile Delta**

The hydrogeological framework of the Nile Delta and immediate surroundings is dominated by four main hydrogeological units (Fig. 3).

### **1.5.1 Nile Delta Aquifer**

It is a semi-confined aquifer dominated by Quaternary deposits (sand and gravel) and is overlain by the Holocene sediments of the Neonile. The thickness of the Nile Delta aquifer varies from 200 m in the south (near Cairo) to 1000 m on the coast (RIGW, 1992). The main source of recharge for this aquifer is the Nile River (El Tahlawi et al., 2008).

### **1.5.2 Coastal Aquifer**

This is a Quaternary to Late Tertiary age aquifer system found on the northern coastal areas of the Nile Delta bordering the Mediterranean Sea (Arabi, 2012). It primarily consists of the coastal dunes and bars, calcarenites and shallow marine deposits, and wadi deposits (Abdel-Shafy and Kamel, 2016).

### **1.5.3 Moghra Aquifer**

The Moghra aquifer consists of Lower Miocene fluvio-marine sand and gravel and it is located on the western margins of the Nile Delta. The thickness of the aquifer

reaches up to 700 m. The Moghra is presumed to be a fossil aquifer but several works suggest that it might be recharged by later inflow from the Nile Delta aquifer (Allam et al., 2003; Negm et al., 2018).

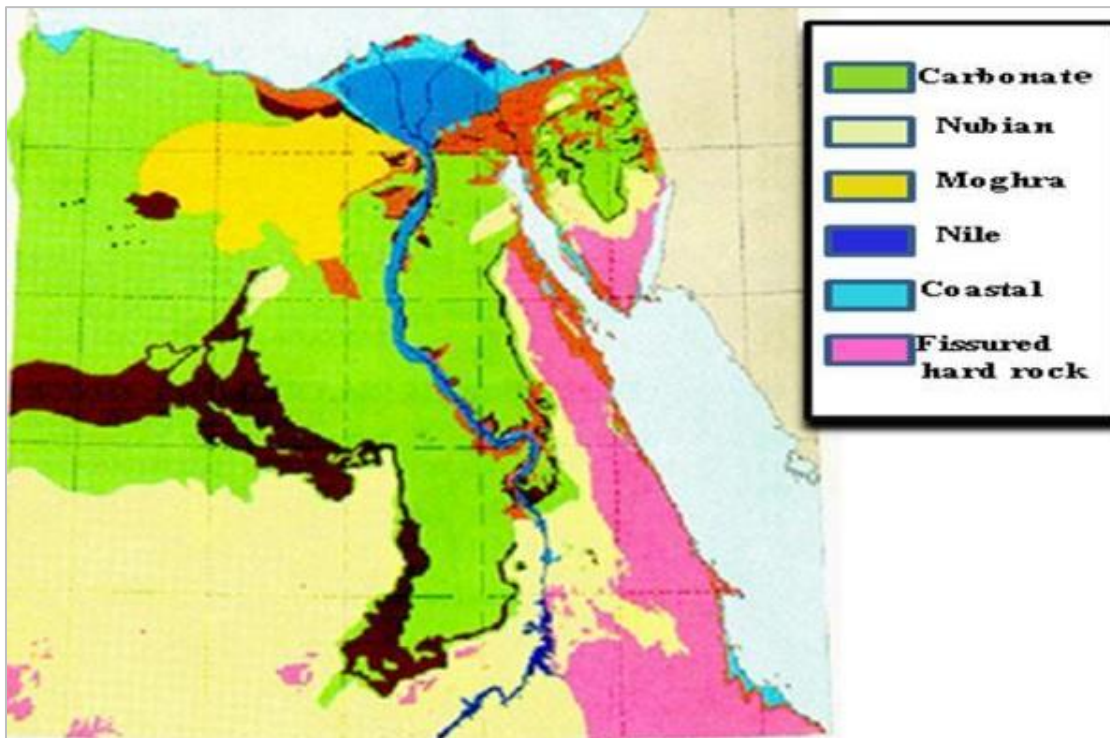


Figure 3: Main aquifer systems in Egypt (Abdel-Shafy and Kamel, 2016)

#### **1.5.4 Fissured Carbonate Aquifer**

This aquifer is assigned to the Eocene and to the Upper Cretaceous and covers more than 50% of Egypt's total area including the eastern fringes of the Nile Delta (Arabi, 2012; Negm et al., 2018). It consists of limestone, dolomite, chalk, and marl with possible local intercalations of shale (Abdalla and Scheytt, 2012)

## **1.6. Statement of the Problem**

The Nile Delta makes up only 2% of Egypt's total area but holds 41% of its total population (Hereher, 2010) estimated at 95 million in 2016 (World Bank, 2017). It includes many of Egypt's highly populated cities and the majority of its industries (Dahshan et al., 2016). It is also Egypt's food basket, containing more than 63% of its cultivated lands and the majority of its fish farms (Hereher, 2009; El-Sayed, 2016).

The onset of the 20<sup>th</sup> century witnessed the progressive construction of dams and barrages (Smith and Abdel-Kader, 1988), causing a decline in sediment accretion rates and a progressive increase in erosional processes (Fanous et al., 1995). The Aswan High Dam (completed in 1968) reduced the sediment load (sedimentation rates prior to 1964: 160 mm/century; Marriner et al., 2013) reaching the coast by more than 98% (Shalash, 1982; Smith and Abdel-Kader, 1988; Syvitski et al., 2009), and brought to a halt, the process of delta accretion and sediment replenishment that were offsetting, to some degree, the subsidence caused by isostatic subsidence (Strzepek, 1995).

Over the last three to four decades, the Nile Delta has witnessed excessive exploitation of its natural resources. Natural gas production in the Nile Delta and its offshore has been on the rise (U.S. Energy Information Administration, 2014), making this region the main natural gas producing region of Egypt (Hamza, 2009).

Groundwater extraction in the delta is also on the rise, especially in its southern (Menoufia district: 1992:  $549 \times 10^6 \text{ m}^3/\text{yr}$ ; 2004:  $654 \times 10^6 \text{ m}^3/\text{yr}$ ) and western districts (Beheira district: 1992:  $109 \times 10^6 \text{ m}^3/\text{yr}$ ; 2004:  $645 \times 10^6 \text{ m}^3/\text{yr}$ ; RIGW, 1992; Hefny and Sahta, 2004).

As stated earlier, the Nile Delta is experiencing land deformation as a result of natural and anthropogenic processes. The current and projected global sea level rise, when combined with the land deformation, could potentially have severe social and economic impacts on Egypt including, but not limited to, loss of agricultural/arable land and aquaculture resources, destruction of infrastructure, population migration, saltwater intrusion, and salinization of groundwater resources (Elsharkawy et al., 2009).

## CHAPTER 2

### LAND DEFORMATION AND SEA ENCROACHMENT IN DELTAS: APPROACHES, RESULTS, AND LIMITATIONS

#### **2.1 Introduction**

There has been a strong interest to study land deformation processes and sea encroachment impacts in river deltas worldwide. With the rise of the number of people living in these deltas and the ensuing intensive anthropogenic, the need to investigate the implications of natural and anthropogenic processes on these densely populated settings has become very critical.

This chapter discusses the key methodologies that are widely used to study land deformation (section 2.2) and sea encroachment processes (section 2.3) in river deltas and the results and limitations of the approaches. It gives emphasis on the type of dataset used, the capability of the approach in dealing with the spatial heterogeneity of the deformation process, and its ability to account for modern processes that are primarily aggravated by anthropogenic activities.

#### **2.2 Land Deformation in Deltas: Methods, Results, and Limitations**

Two main methods have been used for studying natural and/or anthropogenic land deformation of river deltas largely formed of Holocene sediments. The first involves the use of age-depth relationships that are based on radiocarbon dating of

organic deposits from core well data to estimate compaction induced subsidence (Stanley and Hait, 2000; Bird et al., 2004; Törnqvist et al., 2008; Marriner et al., 2012; Stanley and Clemente, 2017) and the second involves geodetic applications. The latter method relies on remotely sensed multi-temporal Interferometric Synthetic Aperture Radar (InSAR) and continuous Global Positioning System (GPS) datasets and techniques (Brown and Nicholls, 2015).

Estimating compaction/subsidence rates in Holocene layers using radiocarbon dating involves measuring the thicknesses of the Holocene layers from the base of a sedimentary sequence to the elevation from which a sample was taken for  $^{14}\text{C}$  dating and comparing it against uncompacted sediments with similar organic matter and grain size characteristics (age-depth relationship) (Bird et al., 2004; Marriner et al., 2012; Stanley and Clemente, 2017). Reworking processes (e.g., incorporation of older organic matter into recent sediment) within the Holocene beds in  $^{14}\text{C}$  age dated samples introduce errors/uncertainties in the age-depth extracted relationships and in the compaction estimates that are based on these relationships (Stanley and Hait, 2000; Colman et al., 2002). Stanley and Hait (2000) studied the compaction and subsidence in the Nile and Ganges-Brahmaputra deltas using  $^{14}\text{C}$  dated core samples from the Holocene layers and reported near similar anomalous age-depth relationships. This apparently fictitious similarity in the age-depth relationships was attributed to inaccuracies in the measured carbon dates that resulted from storage and remobilization of sediments (Stanley and Hait, 2000).

Using radiocarbon-dated core samples, Stanley (1990) provided estimates for average Holocene subsidence rates (up to  $-5$  mm/yr) for the Nile Delta that were caused by compaction of Holocene sediments. Although accurate, the estimated subsidence rates are less likely to represent current subsidence rates: (1) the examined wells are limited in number (87 wells) and thus, the extracted average subsidence rates might not capture the spatial and temporal heterogeneity in sediment composition, texture, and thickness; (2) the current subsidence rates account for subsidence related to natural and anthropogenic factors, whereas the Holocene average rates account for the natural factors only; and (3) there is a decline in subsidence rates with increased sediment age and compaction (Becker and Sultan, 2009), and thus the estimated average rates could be quite different from the present rates.

InSAR methods can detect surface deformation over large areas (swath width: up to 100 km) with cm to mm vertical scale precision (Bürgmann et al., 2000). Persistent Scatterer Interferometry (PSI), a subclass of InSAR, relies on identifying pixels with consistent scattering properties to quantify slow/subtle land motion. Such slow/subtle land motion was detected over river deltas (Teatini et al., 2011) using a stack of multiple radar images acquired over many years (Hanssen and Van Leijen, 2008; Hooper et al., 2012). Similarly, continuous GPS acquisitions can detect land deformation with high precision. The GPS station networks usually lack the dense



distribution of the PSI methods, making it more difficult to extract regional deformational patterns using these applications (Chaussard et al., 2013).

Earlier interferometric applications in the Nile Delta (Aly et al., 2009, 2012; Becker and Sultan, 2009; Poscolieri et al., 2011) had limited spatial coverage and/or used a small number of scenes (5 to 14 scenes; Aly et al., 2012). To the best of my knowledge, this work is the first of its kind in extracting deformational patterns across the entire length and width of a river delta using radar interferometric techniques. The largest possible stack of reliable radar scenes (26–31 scenes per track) were used in the present study to extract optimum estimates of deformation rates and apply advanced methods (Hooper et al., 2004, 2007) to better identify the locations of persistent scatterers (PS) and estimate their velocities even if they were present in partially vegetated pixels, with a low signal-to-noise ratio.

### **2.3 Sea Encroachment on Coastal Areas in Deltas: Approaches, Results, and Limitations**

The populations of many of the coastal areas of deltas worldwide are facing threats of sea water encroachment due to global warming-related sea level rise and subsidence caused by natural and anthropogenic factors (Nicholls and Cazenave, 2010). Subsidence in coastal areas can potentially amplify sea level rise-related flooding (Dixon et al., 2006; Mazzotti et al., 2009). The Intergovernmental Panel on Climate Change (IPCC) estimated the global eustatic sea level rise at 0.19 m (1.7

mm/yr) for the time period 1901 to 2010, but higher rates (3.2 mm/yr) were noted from 1993 to 2010 (Church et al., 2013).

Several studies investigated the impact of sea level rise on coastal areas of the world using projected estimates for sea level rise and available digital elevation models (DEMs) (e.g., Rowley et al., 2007; Hinkel et al., 2014), including the Nile Delta (e.g., Hereher, 2010; Zaid et al., 2014; Hasan et al., 2015; Shaltout et al., 2015; Stanley and Clemente, 2017). Examples of the commonly used DEMs in such models include the Global Land One-Kilometer Base Elevation (GLOBE), Shuttle Radar Topography Mission (SRTM) and Advanced Spaceborne Thermal Emission and Reflection Radiometer (ASTER) DEMs. The low spatial resolution and low absolute and relative accuracy of these DEMs introduce large uncertainties in the modeled inundated areas. SRTM DEMs have a resolution of 1–3 arcseconds, less than 16 m absolute vertical height accuracy and less than 10 m relative vertical height accuracy (Rabus et al., 2003; Farr et al., 2007). ASTER DEMs have a resolution of 1 arcsecond and less than 17 m absolute vertical height accuracy (Tachikawa et al., 2011; Gesch et al., 2012). SRTM and ASTER DEMs values are given in integer values and thus these DEMs cannot adequately capture sub-meter variations in digital elevations (Farr et al., 2007; Athmania and Achour, 2014); rounding surface elevations to whole numbers will produce fictitious distributions for areas threatened by sea encroachment.

The following practices can introduce additional errors in the inundation simulation outputs: (1) failure to account for land deformation contributions such as those caused by glacial unloading, uplift, and subsidence (e.g., Rowley et al., 2007; El-Nahry and Doluschitz, 2010; van de Sande et al., 2012); (2) assigning a uniform deformation rate that was derived locally across a much larger region, a practice that ignores the spatial heterogeneities in sediment composition and texture within the investigated areas and the local variations introduced by anthropogenic factors (e.g., Frihy, 2003; Hasan et al., 2015; Neumann et al., 2015), and (3) reliance on average Holocene subsidence rates that do not represent current subsidence rates (Hereher, 2010; Abdrabo and Hassaan; 2015; Hasan et al., 2015).

## **2.4 Objectives of the Research and Approaches**

The target of this research is to accomplish the following tasks: (1) estimate the temporal and spatial deformation over the entire Nile Delta and surroundings using InSAR data over a 7-year period (2004 to 2010); (2) investigate the natural and anthropogenic factors controlling the observed deformation through spatial correlation of the observed deformation with relevant spatial datasets (fluid withdrawal, distribution of paleochannels, and analysis of core well samples from earlier studies); (3) identify areas susceptible to sea encroachment by simulating (over the period 2010–2100) sea level rise over the northern Nile Delta using projected sea level rise rates, extracted deformation rates, and a high-resolution digital elevation model, and (4) compare the findings of this study over the Nile Delta with those from

earlier studies in deltas that have been undergoing deformation for thousands of years due to sediment accumulation and compaction (Stanley, 1997; Törnqvist et al., 2008), isostatic lowering (Stanley, 1997; Syvitski, 2008), tectonics (Dokka, 2006), and more recently, anthropogenic interventions (Stanley and Warne, 1993; Carminati and Di Donato, 1999; Syvitski, 2008; Syvitski et al., 2009). The latter includes: (1) the construction of dams and reservoirs which impound sediments upstream and decrease sediment loads reaching deltas and coastal area by as much as  $1.4 \pm 0.3$  billion metric tons/yr (Syvitski et al., 2005), sediments that could have compensated in part for the subsidence, and (2) the extraction of groundwater and hydrocarbons that can increase natural deformation rates by up to an order of magnitude (Meckel et al., 2007; Syvitski, 2008).

## CHAPTER 3

### DATA AND METHODS

#### **3.1. Introduction**

In this chapter, the data and methods used to respond to the research objectives of this study, stated in the previous chapter, are thoroughly explained. The first subsection discusses the remote sensing approach and datasets I used to quantify land deformation processes. The second subsection discusses the procedures used in this study to delineate the paleochannels of the Nile River. Understanding the spatial distribution and flow pattern of the paleochannels will be helpful in mapping the spatial distribution of the compressible sediments, brought about by the branches of the Nile River, in the Nile Delta that have significant impact on land deformational processes. The last subsection of this chapter discusses the approaches and datasets used in this study to investigate the social and economic impacts of sea level rise on the coastal areas and communities of the Nile Delta.

#### **3.2. Land Deformation Analysis**

##### **3.1.1 Interferometric Synthetic Aperture Radar (InSAR)**

Since the launch of the European Remote Sensing Satellite (ERS-1) in the early 1990s and the subsequent acquisition of continuous synthetic aperture radar (SAR) images over a given span of time, radar interferometry has been effectively used to measure and model the earth's topography and to detect centimeter to

millimeter-scale surface displacements on a wide spatial scale (Kampes, 2006; Smith, 2002). Since the launch of the ERS-1 satellite, several other spaceborne SAR missions operating in different microwave bands (e.g., C-band (5.6 cm wavelength), L-band (23.6 cm wavelength) such as the ERS-2 (C-band), Environmental Satellite (Envisat) (C-band), Advanced Land Observing Satellite (ALOS) (L-band), and the recently launched Sentinel constellations (Sentinel 1A and 1B, C-band) have provided a wealth of SAR data (Fig. 4).

Spaceborne SAR techniques use the forward motion of the antenna on the sensor to compensate for the small length of the actual antenna to simulate a very long antenna and hence enabling it to have a better resolution (Chan and Koo, 2008). SAR is an active imaging sensor capable of providing images regardless of the time of the day (day or night), cloud, and other weather conditions (Garello, 2010). SAR systems send electronic pulses with high power, in the along-track direction (also called azimuth direction), to the earth's surface and receive the backscattered signal that comprises the phase and amplitude information of the imaged area (Fig. 5). The raw data acquired by the SAR sensor is focused to generate a radar image. The value of each pixel in the radar image is a function of the scattering properties of the imaged earth's surface. Bright spots in the images signify targets with high backscatter signal return while dark areas in radar images correspond to weak backscatter return from flat and smooth surfaces (Fig. 6) (Moreira et al., 2013; Zhou et al., 2009).

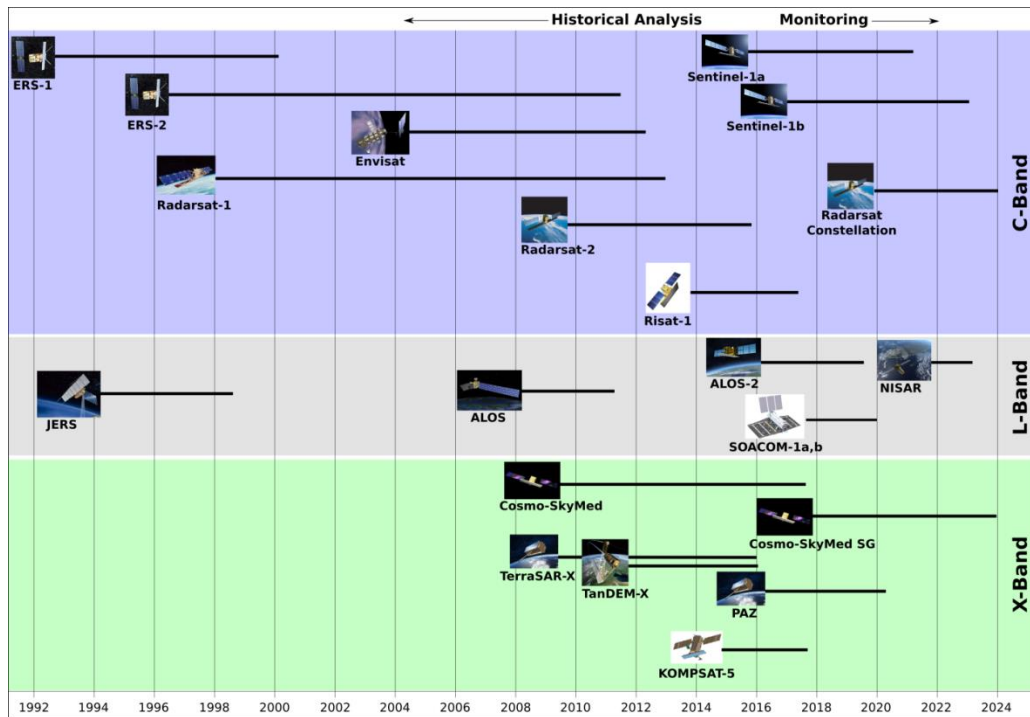


Figure 4: Overview of past, current, and future spaceborne SAR missions (UNAVCO, 2018)

InSAR is a cost-effective remote sensing technique that can be used for a wide variety of applications including quantifying crustal deformation rates and delineating faults after earthquake events (Xu et al., 2015), landslide detection (Kang et al., 2017), and investigating land subsidence processes attributed to fluid (groundwater, oil, and gas) withdrawals (Holzer and Galloway, 2005).

InSAR technique is based on radar imaging of the same surface (target) at multiple times (Fig. 5) and extraction of the phase difference between the images to

calculate distance and angular measurements (Balmer and Hartl, 1996; Hanssen, 2001; Rosen et al., 2000)

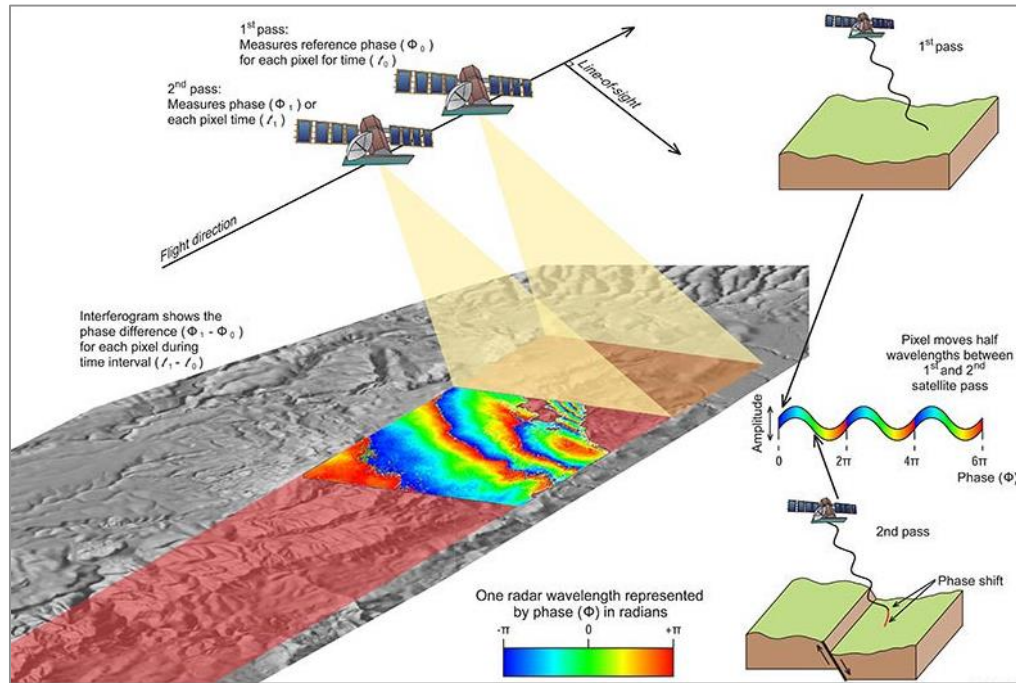


Figure 5: A summary sketch of repeat-pass (shown as 1<sup>st</sup> pass and 2<sup>nd</sup> pass data acquisition times on the sketch) InSAR technique (also known as Differential SAR Interferometry (DInSAR) showing how deformation estimates are calculated after a major (e.g., earthquake) land deforming event (Garthwaite et al., 2015).

InSAR works only if the coherence conditions of the compared SAR images are established (Hanssen, 2001). The difference in phase of two coherent SAR phase images of the same area forms an interferogram (Fig. 5). The coherent SAR images used for the generation of an interferogram can be either be radar images from a single-pass interferometric configuration in which two antennas on the same platform are used to collect radar echoes, or repeat-pass configuration in which two radar



images acquired by a single antenna at different times from a slightly different position (Fig. 5). The first scene (reference scene) is commonly called the master scene and second (repeat) image is called a slave scene. The spatial distance between the two satellite positions is called the baseline and its component perpendicular to the satellite's look direction (Line-of-Sight (LOS); Fig. 7) is called the perpendicular baseline (Hanssen, 2001; Klees and Hanssen, 2000; Zhou et al., 2009).

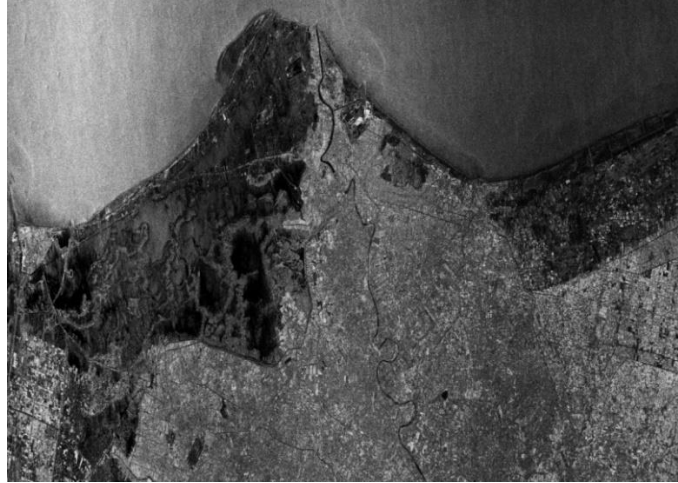


Figure 6: Environmental Satellite (Envisat) SAR image of the northern Nile Delta region. Urban areas appear bright as a result of high backscatter signal while vegetated areas and water bodies (Lake Manzala and the Mediterranean Sea) appear in moderate to dark black color due to poor backscatter return.

The interferometric phase change (difference)  $\phi$  is a function of  $\theta$  (look angle),  $\alpha$  (baseline orientation),  $B$  (baseline between the master and slave orbits),  $\Delta r$  (across-track displacement),  $\Delta x$  (along-track displacement),  $\lambda$  (radar wavelength),  $\psi$  (squint angle), and  $\delta\rho$  (the slant range distance differences between the master and slave images). Assuming that the squint angle ( $\psi$ ) is negligible due to zero Doppler

geometry, the interferometric phase change ( $\phi$ ) is summarized in the equation below (Jung et al., 2014).

$$\phi = -\frac{4\pi}{\lambda} B \cdot \sin(\theta - \alpha) + \frac{4\pi}{\lambda} \Delta r \quad (3.1)$$

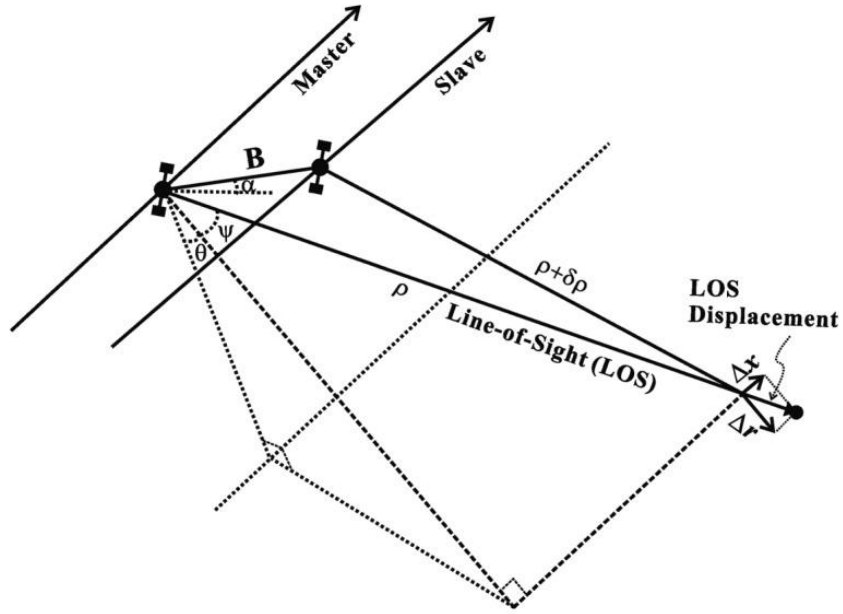


Figure 7: SAR interferometric imaging geometry (Jung et al., 2014)

InSAR Data processing procedures for quantifying land deformation processes are summarized below:

a) Selection of Interferometric Pair

The selection of interferometric pairs depends on a number of factors including the type of sensor, availability of data, specific application of the study,

coherence and correlation of the two sets of signals acquired at different times, and characteristics of the terrain and atmosphere during image acquisitions. The characteristics of the terrain such as the roughness, elevation range, type and amount of vegetation, and the intensity of anthropogenic activities are key terrain factors that should be considered during the selection of interferometric pairs (Hanssen, 2001; Zhou et al., 2009).

#### b) Image Coregistration

SAR interferometry requires a sub-pixel level matching (coregistration) between the SAR images (Fig. 8). Coregistration involves cross-correlating blocks of one SAR scene with the other (master and slave scenes) in search for offsets between the images (Li and Bethel, 2008; Yun et al., 2007). Two levels of coregistration techniques are widely used in SAR interferometry namely coarse and fine coregistration. As the name implies, coarse coregistration does not require a high level of accuracy during the coregistration (aligning) process. It typically makes the alignment to only one or two-pixel accuracy (Li and Bethel, 2008). Following the pixel level coregistration (coarse coregistration), a subpixel-to-subpixel level coregistration is performed using the output of the coarse coregistration step as input for the fine coregistration process.

### c) Interferogram Generation

Following the coregistration procedure, the two SAR images are combined to produce a SAR interferogram. Complex interferogram (Fig. 9) is formed by multiplying each complex pixel on the master image with its exact representative on the slave image (Li et al., 2004). The total phase in the generated complex interferogram is the sum of phase contributions and noise emanating from various sources including the flat-earth and topographic effects.

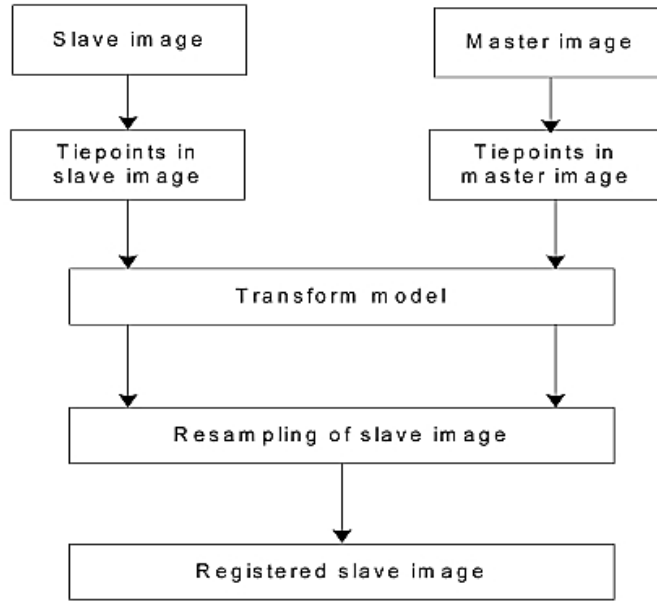


Figure 8: SAR image coregistration procedure (Zou et al., 2009)

The complex interferogram ( $\phi_{int}$ ) is:

$$\phi_{int} = \phi_{flat} + \phi_{topography} + \phi_{displacement} + \phi_{atmosphere} + \phi_{noise} \quad (3.2)$$

Where  $\phi_{flat}$  is the phase contribution of the flat earth (due to the earth's curvature),  $\phi_{topography}$  is that of topography,  $\phi_{displacement}$  (Fig. 10) is that of change due to movement of the pixel in slant-range direction (displacement),  $\phi_{atmosphere}$  is that of the atmospheric effect, and  $\phi_{noise}$  is that of the noise. The phase contribution due to the curvature of the earth (flat earth phase  $\phi_{flat}$ ) is removed using precise orbit data. The impact of topographic effect ( $\phi_{topography}$ ) can be corrected by subtracting a simulated topographic phase from a DEM (Yun et al., 2015).

The influence of the atmospheric contribution ( $\phi_{atmosphere}$ ) on the overall interferometric phase (mainly the water vapor effect) can be addressed in several ways but two main approaches are widely used. The first approach is to avoid selecting SAR images acquired during cloudy weather conditions or during where there are indications of convectivity in the troposphere. An example of comparative cloud conditions at the time of image acquisition in the Nile Delta is shown in figure 11. The state of the atmosphere (water vapor distribution) at the time of the image acquisition can be obtained either from satellite-based sources (e.g. NASA's Moderate Resolution Imaging Spectroradiometer (MODIS) instrument on the Terra and Aqua satellites) or ground-based meteorological data. The other widely used approach is the correction of atmospheric effects based on high-resolution meteorological models (Ding et al., 2008; Hanssen, 2001; Wadge et al., 2002).

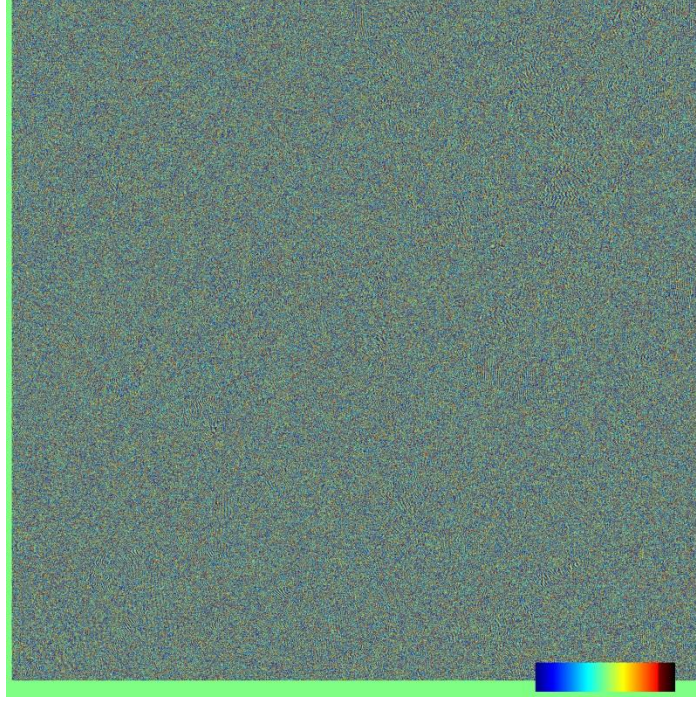


Figure 9: A wrapped complex interferogram of the April 6, 2009, L'Aquila earthquake (central Italy) event produced from interferometric analysis of two (repeat-pass) Envisat ASAR images acquired before (February 2, 2009) and after (April 12, 2009) the event. Each pixel contains the difference (in phase value) between the phases of the two Envisat ASAR images. The interferogram product was generated using the Delft Object-oriented Radar Interferometric (DORIS) software (Kampes, 1999).

Finally, the  $\phi_{noise}$  comprises phase contributions from different sources such as spatial and temporal decorrelation, and thermal noise of the SAR sensor. This phase noise can be reduced through adaptive filtering and multi-looking techniques (Chen and Xu, 2014; Liao et al., 2013; Zhou et al., 2009)

#### d) Phase Unwrapping

Phase values in the generated interferograms are given as the  $2\pi$  modulus of the absolute phase signal (Hanssen, 2001). This is the wrapped phase and it only accounts for the phase signal within once cycle and does not resolve the  $2\pi$  ambiguity of the SLC phase data. This phase ambiguity is resolved by the phase unwrapping technique and an absolute (continuous) phase value is extracted. The accuracy of the phase unwrapping procedure becomes less reliable with decreasing coherence (Kampes, 2006).

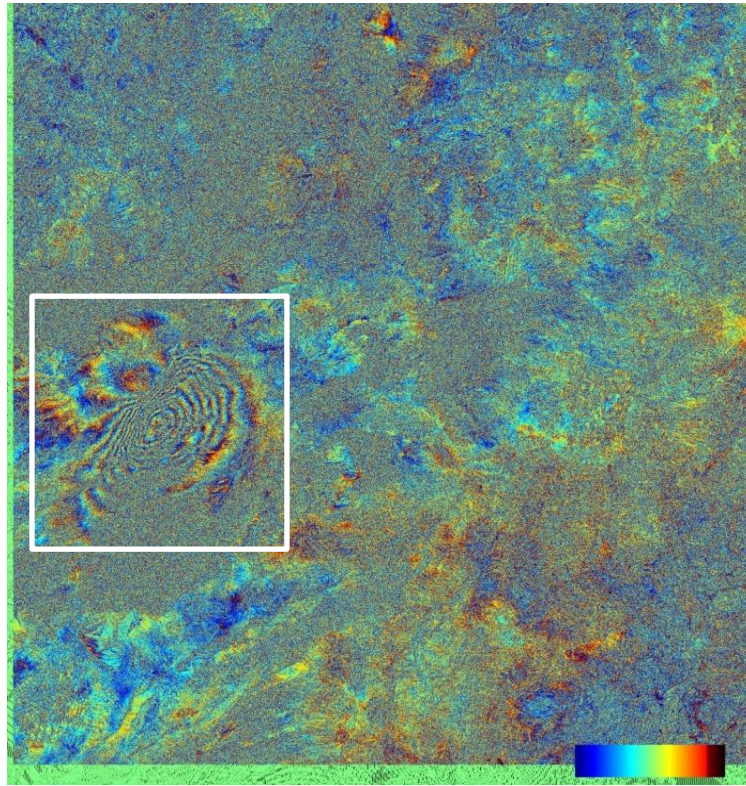


Figure 10: A wrapped interferogram (in radar geometry) of the April 6, 2009, L'Aquila earthquake event after the removal of phase contributions from different sources (e.g.  $\phi_{\text{noise}}$ ,  $\phi_{\text{topography}}$ ). A maximum deformation of nearly 23 cm (shown in white box) along the satellite's line of sight is calculated from this product.



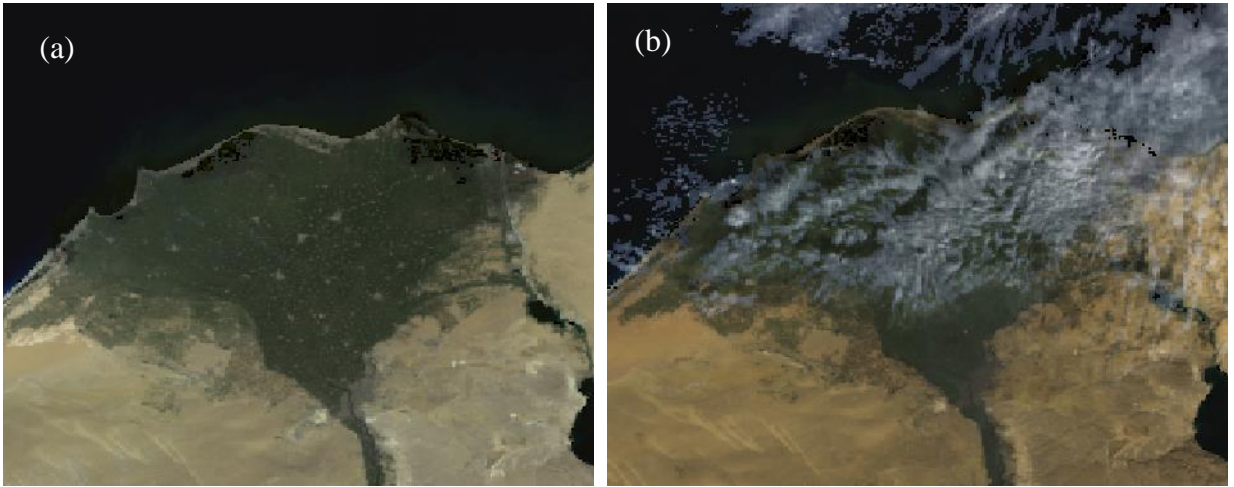


Figure 11: Optical Imagery portraying the atmospheric conditions at the time of Envisat ASAR image acquisition. The imagery was acquired by the Medium Resolution Imaging Spectrometer (MERIS) sensor which is one of the sensors onboard of the Envisat satellite. Figure (a) shows a stable (less convective) troposphere (cloud) state of the atmosphere while the ASAR imagery was acquired. Figure (b) shows cloudy atmospheric conditions at the time of ASAR image acquisition.

#### e) Phase to Displacement Conversion and Geocoding

In the phase to displacement conversion step, the unwrapped interferometric phase values are initially converted to displacement for each pixel and (the radar coordinates are) geocoded into a known map reference system/projection (Hanssen, 2001).

### 3.1.2 Persistent Scatterer Interferometry (PSI)

The PSI method was initially developed by Ferretti et al. (1999) with a target of compensating for the limitations posed by the repeat-pass InSAR, variations in



atmospheric conditions, and geometrical and temporal decorrelations (Kampes, 2006). Conventional InSAR is mostly applied to dry, and sparsely vegetated areas where the possibility of temporal decorrelation (loss of interferogram coherence) due to variation in vegetation and snow cover, and weathering processes is avoided (Ferretti et al., 2001; Zebker and Villasenor, 1992).

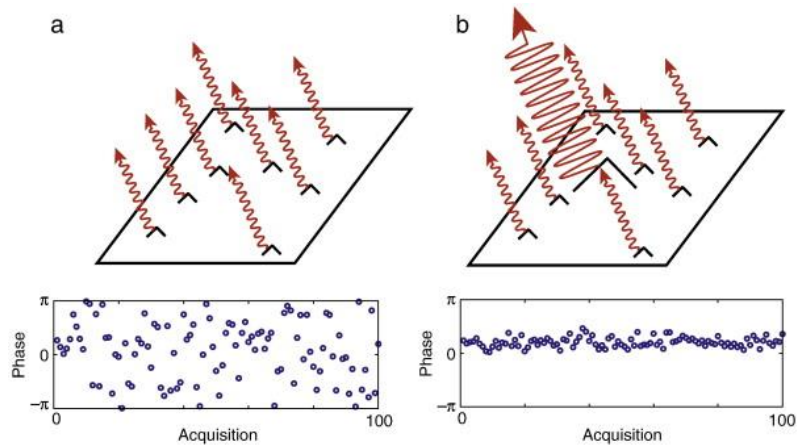


Figure 12: A cartoon depicting the variation in phase response from (a) distributed scatterer pixel, and (b) a persistent scatterer pixel. Different image acquisitions from different orbit tracks produce an erratic phase response (bottom figure in (a)). A dominant single persistent scatterer, on the other hand, produces a stable phase response under varying conditions (Hooper, 2006).

Each pixel on a radar image represents the coherent sum of many individual resolvable scatterers within the resolution cell and with the change of the orbital tracks and hence the angle of incidence during repeat-pass SAR image acquisition, the possibility of obtaining the same coherent sum from the same scatterers in a pixel

is low (Zebker and Villasenor, 1992). One of the main limitations of the repeat-pass InSAR technique is its inability to measure small amounts (changes) of deformation.

In the PSI technique, stacks of single-master interferograms are used to calculate subtle deformation changes for pixels that are identified to exhibit temporal phase stability (Garthwaite, 2015). This method avoids the limitations in conventional InSAR by analyzing pixels that show stability (Fig. 12) over a given time, called persistent scatterers (PS), and discards scatterers that show poor correlation (Hooper et al., 2004). Common PS's include roads, buildings, rock outcrops, buildings, and other manmade objects commonly available in urban areas but less outside cities (Raspini et al., 2018).

Three main methods are commonly used to detect/identify potential persistent scatterers: methods based on normalized amplitude dispersion, phase stability, and correlation (Jia and Liu, 2016). In this research, the normalized amplitude dispersion method was used for identifying and selecting persistent scatterers. The amplitude dispersion  $D_A$  is given as:

$$D_A = \frac{\sigma_A}{m_A}, \quad (3.3)$$

where  $\sigma_A$  and  $m_A$  are the standard deviation and the mean value of the backscattering intensity respectively.

In this study, the PSI technique (Hooper et al., 2004, 2007) was applied to assess and quantify land deformation in the study area. The method identifies coherent PS pixels from temporal radar scenes and follows their deformation over time (Ferretti et al., 2001). This method was preferred (Hooper et al., 2004, 2007) over others due to its ability to identify PS pixels and estimate their velocities despite their low signal-to-noise ratio, a feature caused by temporal decorrelation and commonly observed in densely vegetated areas (Hooper et al., 2004, 2007) like the Nile Delta. A high amplitude dispersion ( $D_A$ ) threshold value of 0.4 was used for the initial selection of PS points which enhances the identification of PS pixels located outside of the urban centers (Hooper et al., 2004).

One hundred twenty-five right side looking image mode (Miranda et al., 2013) descending raw scenes acquired by the Environmental Satellite's (Envisat) Advanced Synthetic Aperture Radar (ASAR) sensor were downloaded from the European Space Agency (ESA). The ASAR scenes were acquired along three tracks (479, 207, and 436) over a time span of eight years (2003 to 2010). The scenes were focused (to level 1 single look complex images) using the Repeat Orbit Interferometry Package (Buckley et al., 2000). Eighty-four (84) scenes (2004 to 2010) were then selected for PSI pre-processing level (Fig. 13) based on their temporal baseline (maximum value: 1645 days) and spatial baseline (maximum: 855 meters), as well as the mean Doppler centroid frequency difference values with respect to the master scene (Zebker and Villasenor, 1992).

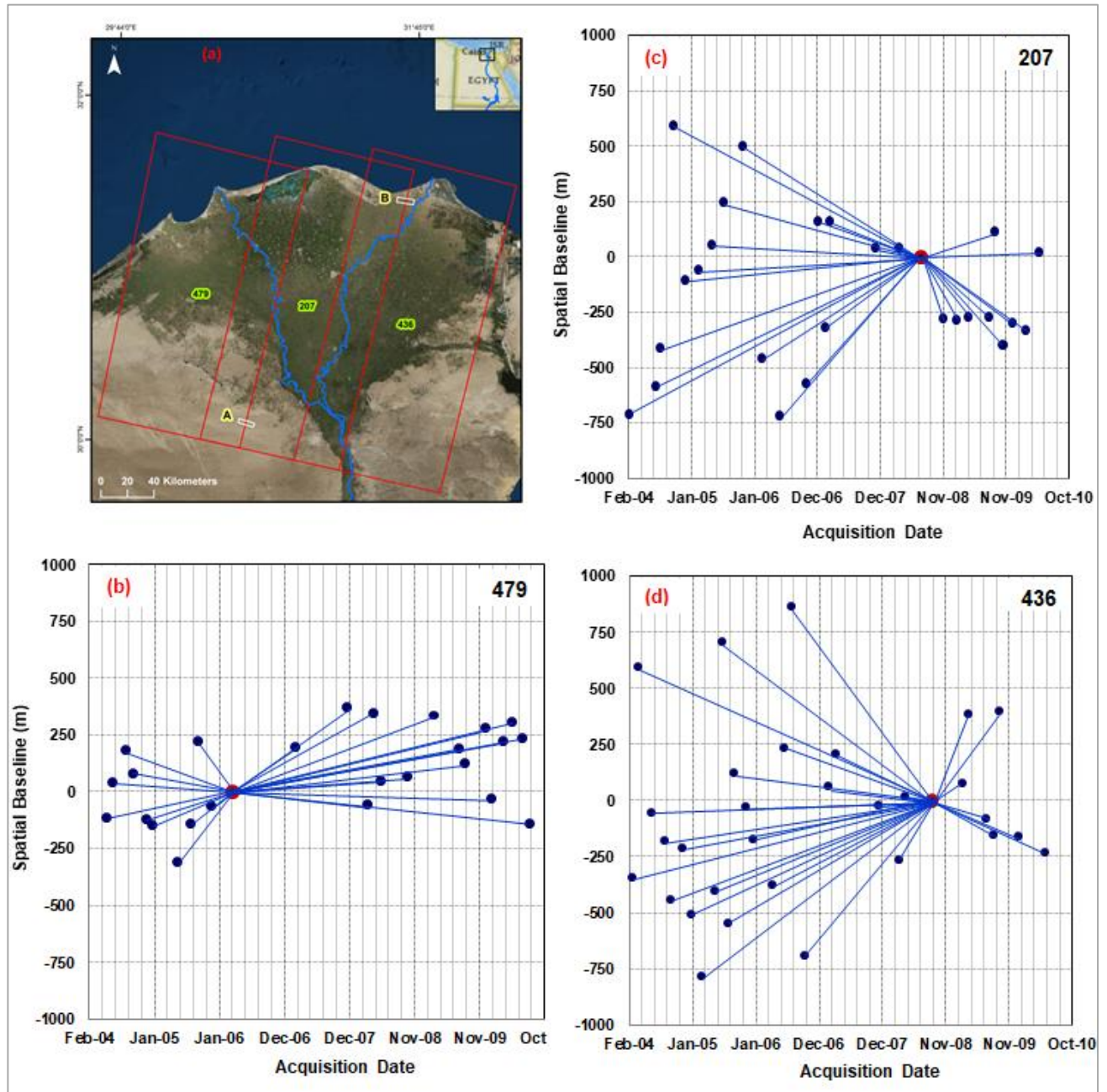


Figure 13: (a) Nile Delta and surrounding regions with the footprints of the descending satellite tracks that cover the study area (b) Spatial baseline–time plot for the descending tracks 479, used in this study. Master scenes are shown in red dots while other SAR images are shown in dark blue color. (c) Same as (b) above, but for track 207. (d) Same as (b) above, but for track 436.

In PSI pre-processing, the offset (coarse and fine coregistration) was estimated between the master scene and each of the slave scenes, as well as among the slave scenes themselves, and the scenes were realigned (resampled). A two-pass interferometry was then generated between the master scene and each of the slave scenes. The topographic phase contribution was estimated using radar coded 3 arc second SRTM DEM. Precise orbital records retrieved from the Delft precise orbits were used for orbital error estimation. The radar coded pixels were geocoded to a known reference system using orbital information and a DEM. Following the initial selection of pixels that was based on amplitude dispersion, the pixels experiencing phase stability (threshold  $> 0.3$ ) were then identified as PS points. Residual errors (e.g., spatially correlated and uncorrelated look angle–DEM related errors) were removed, unwrapped, and their deformation rates were calculated (Hooper et al., 2004, 2007). A summary of the applied PSI processing procedure is shown in figure 14.

The wet signal delay introduced by the troposphere was modeled and removed from the final deformation estimate (Bekaert et al., 2015). Weather datasets from the MERIS sensor, which measures the atmospheric conditions while the Envisat ASAR scenes are being acquired, were used for this purpose. The deformation estimates were referenced and normalized to a relatively stable permanent GPS station (ALEX) in Alexandria city (period: 2002–2008; <http://www.sonel.org>). The station measured an average deformation rate of  $0.05 \pm 0.28$  mm/yr. A second GPS station (PHLW;

<http://geodesy.unr.edu/>) located south of Cairo (period: 2000 – 2003) was used to validate the accuracy of the adopted methodology.

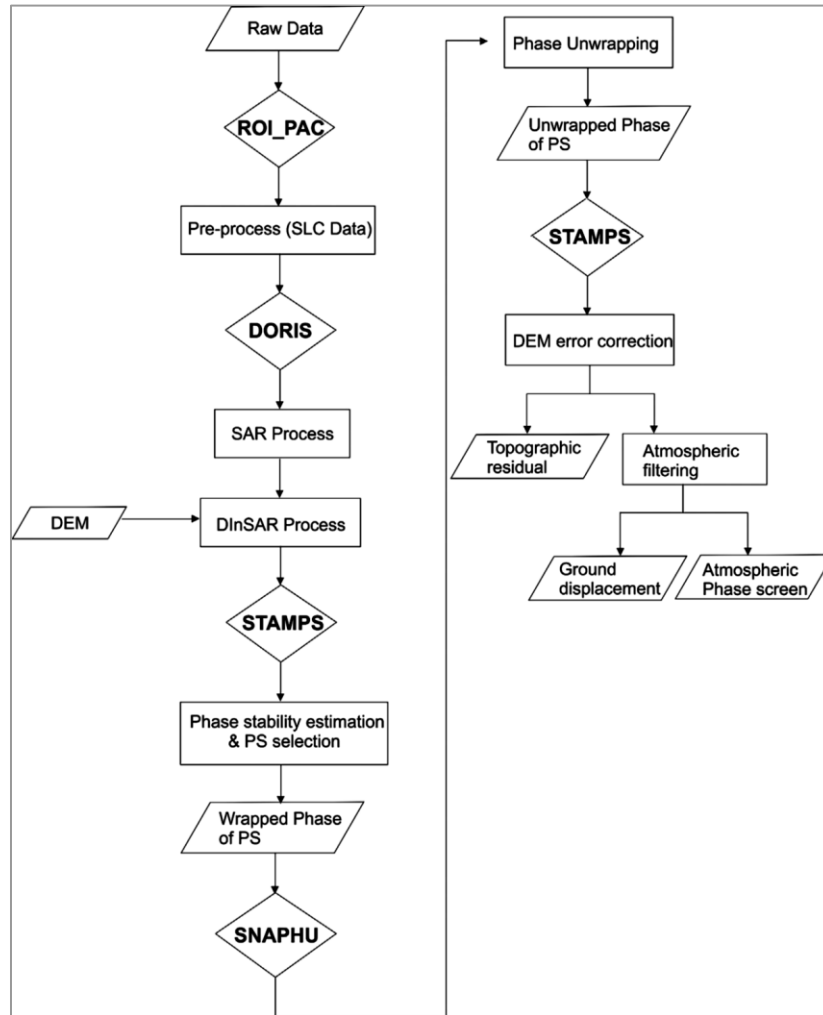


Figure 14: Persistent Scatterer Interferometry data processing flowchart (Hooper et al., 2004; Yhokha et al., 2015)

PSInSAR results are given in slant range (i.e., along line of sight; LOS). The radar LOS ( $d_r$ ) output is a three-dimensional motion comprising north ( $d_n$ ), east ( $d_e$ )

and up ( $d_n$ ) direction motion components; for a satellite orbit with heading (azimuth)  $\alpha_h$  and incidence angle  $\theta_i$ , the radar LOS is given by (Hanssen, 2001):

$$d_r = d_u \cos(\theta_i) - \sin(\theta_i)[d_n \cos(\alpha_h - 3\pi/2) + d_e \sin(\alpha_h - 3\pi/2)] \quad (3.4)$$

where  $(\alpha_h - 3\pi/2)$  refers to the angle to the azimuth direction.

Mohamed et al. (2016) stated that the horizontal velocities (motion) in the Nile Delta are small. Excluding the negligible amount of the horizontal motion from the above equation gives:

$$d_r = d_u \cos(\theta_i) \quad (3.5)$$

Subsequently, the vertical motion component is calculated to be:

$$du = (dr) / (\cos(\theta_i)) \quad (3.6)$$

Where  $d_u$  and  $d_r$  represent vertical and LOS motions respectively, and  $\theta_i$  is the incidence angle. The incidence angle of the pixels in the three tracks ranges from 16.4° to 22.9°. Figure 21a displays the results of the vertical component of the extracted land deformation rate (in mm/yr) for the Nile Delta and surroundings. Positive deformation values represent upward motion (uplift) while negative values represent downward motion (subsidence).

The PSI results for track 479 were referenced against records from the Alexandria GPS station (Fig. 15) and then used to calibrate tracks 207 and 436. Track 207 was first calibrated to track 479 and then used to calibrate track 436. Calibration of track 207 to 479 involved identification of the common PS points within the area

of overlap, the ones that are separated by no more than 10 meters apart. A buffer filter of 10 meters was adopted to compensate for displacements in PS locations that could arise from offset or coregistration-related errors between overlapping tracks. The mean for the identified populations of common scatterers was calculated (track 479: 0.35 mm/yr; track 207: 0.06 mm/yr), and the offset in the mean values (-0.29 mm/yr) was added to all PS pixels in track 207. Using the same approach, the offset between overlapping pixels in tracks 207 and 436 was estimated at -0.33 mm/yr and was added to all PS pixels of track 436.

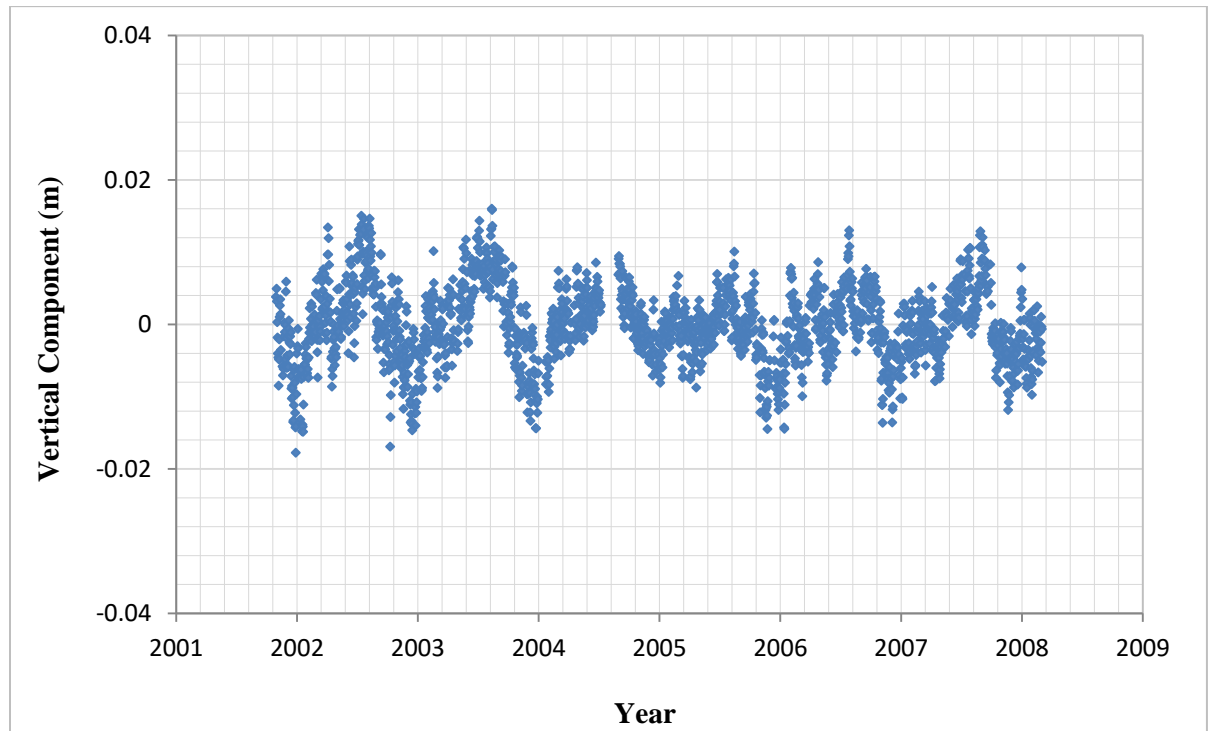


Figure 15: Time series showing nearly 6 years (2002-2008) daily vertical component ground motion at ALEX GPS station in Alexandria (The weekly averaged deformation rate is  $0.05 \pm 0.28$  mm/yr)



### **3.3. Mapping Paleochannels**

Procedures and datasets developed by El Bastawesy et al. (2016) to map the distribution of paleochannels across the entire Nile Delta and surroundings were used in the present study. El Bastawesy et al. (2016) noted that the current and defunct Nile distributaries are standing higher (by  $\sim 4$  m) than their surroundings and attributed this to the differences in the hydrological and sedimentological characteristics of the sediments making up the rivers and the surrounding floodplains. That is, the water saturated sands of the river channels are less prone to compaction compared to the silts and clays of the floodplains. Using this notion, they delineated the Saitic and Sebennitic defunct Nile River distributaries and found a good correspondence between the inferred and documented (Baynes, 1988) distribution of those paleochannels.

Earlier attempts (Ball, 1939; El Gamili et al., 2001, El Mahmoudi and Gabr, 2008; Sneh and Weissbrod, 1973; Quintanar et al., 2013; Stanley and Jorstad, 2006; Tousson, 1922) to map these paleochannels using several techniques were only successful in delineating small segments (Fig. 16) due to a variety of reasons.

In this work, the now obsolete paleochannels of the Nile River were delineated using a high-resolution digital elevation model (10 m horizontal resolution) over the delta by integrating elevation data from 195 high resolution

(1:25,000 scale; 0.5 m contour interval) topographic map sheets (Egyptian Surveying Authority, 1946) and by interpolating contour and point elevations. The generated DEM was inverted rendering the elevated river banks the appearance of valleys, and the paleochannel networks were then derived using stream delineation tools within the Spatial Analyst Toolbox of ArcGIS (El Bastawesy et al., 2013).

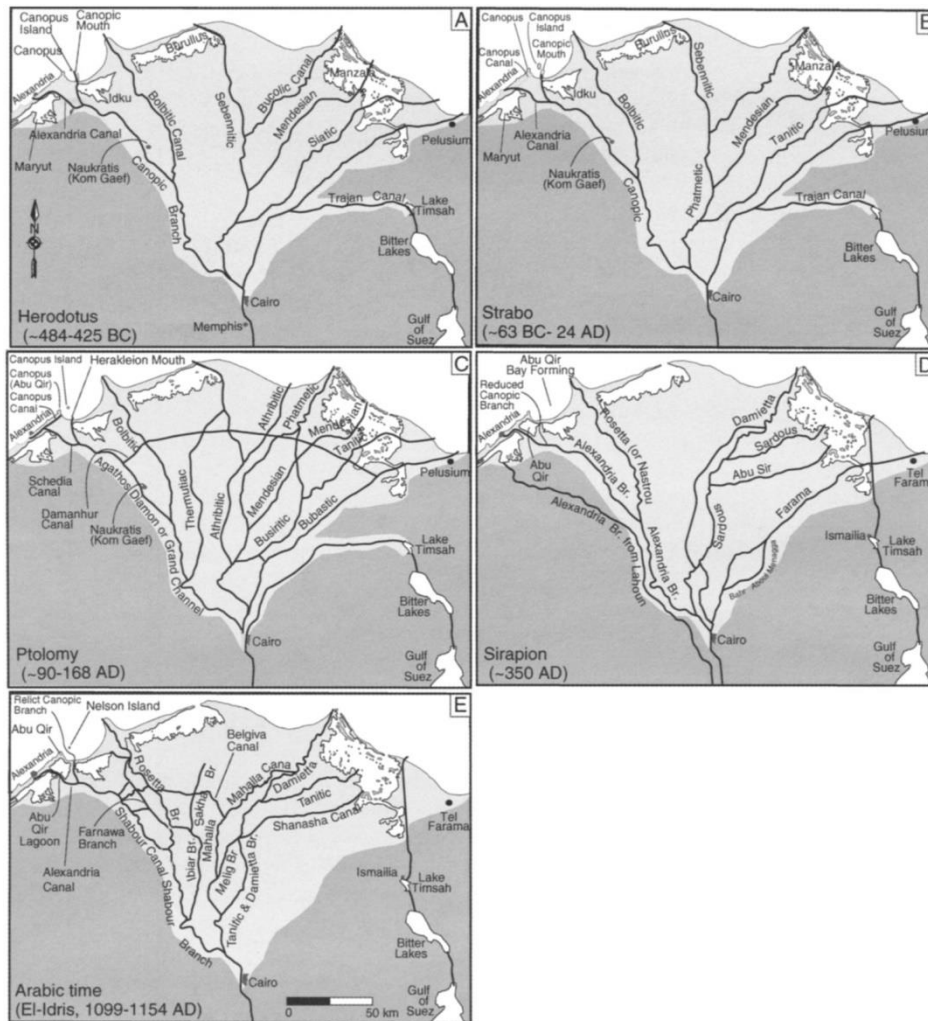


Figure 16: The positions of the distributaries of earlier and current Nile river branches in the Nile Delta as per the historical versions (maps) given by Herodotus (484 - 425 B.C.), Strabo (63 B.C. – 24 A.D), Ptolemy (90 – 168 A.D.), Serapion (350 A.D.), and El-Idrisi (1099 - 1154 A.D.) (Stanley et al., 2004; Toussoun, 1922).

### 3.4. Impact of Sea Level Rise on Coastal Areas and Communities

The impact of sea level rise on coastal areas by the year 2100 was evaluated by simulating sea encroachment scenarios using (1) deformation results from the PSI analysis, (2) projected estimates of sea level rise from the IPCC models (Fig. 17), (3) a high-resolution TanDEM-X digital elevation model, (4) land cover datasets, and (5) population density data.

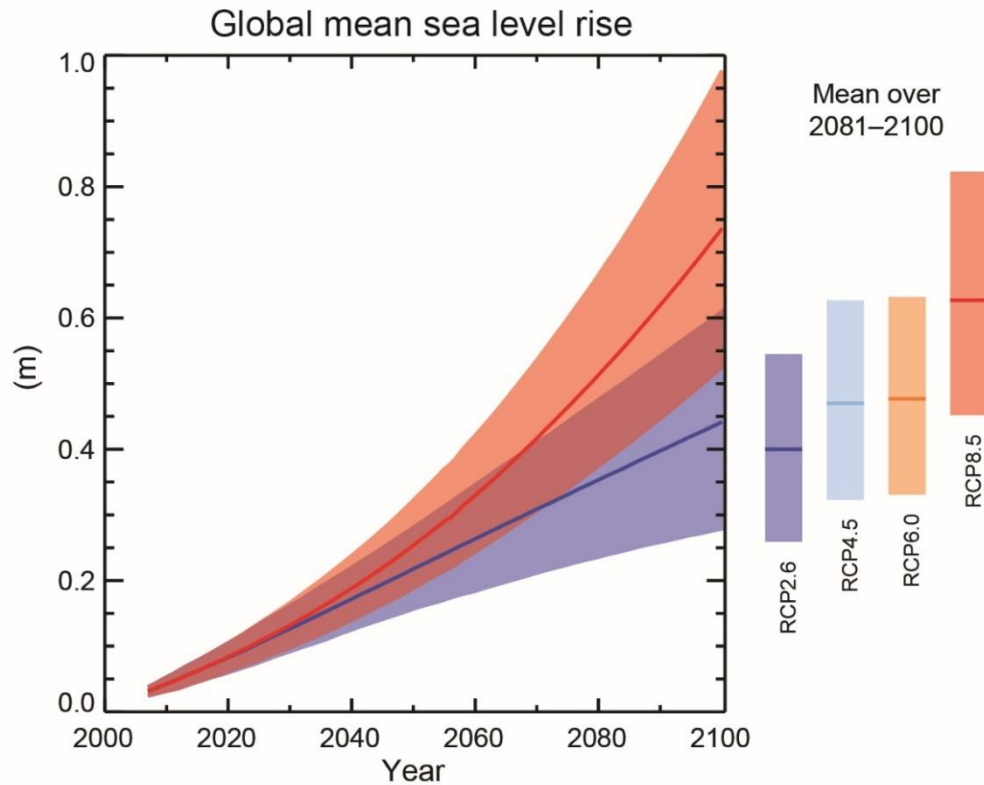


Figure 17: Global mean sea level rise projections through the year 2100 (Church et al., 2013) using the four Representative Concentration Pathway (RCP) model scenarios (RCP 2.6, RCP 4.5, RCP 6.0, and RCP 8.5). The highest mean sea level rise values by the end of the 21<sup>st</sup> century were projected by the RCP 2.8 model (0.74 m) followed by RCP 6.0 (0.55 m), RCP 4.5 (0.53 m), and RCP 2.6 (0.44 m).

Several IPCC models (Representative Concentration Pathway [RCP] models), project sea level rise–values ranging from 0.28 to 0.98 m by the end of the 21<sup>st</sup> century (Fig. 17) under varying scenarios for greenhouse gas emission, ocean warming, and melting of glaciers and ice sheets (Church et al., 2013). The Representative Concentration Pathway 2.6 (RCP2.6) which takes into consideration the recent Paris Agreement by various nations to reduce greenhouse gas emissions and other mitigation measures (Hulme, 2016) was selected. The selected model accounts for a projected eustatic sea level rise of 0.28 to 0.61 m (0.44 m average; Church et al., 2013; Van Hooideonk et al., 2013).

Digital elevation models with ten-year time steps were generated assuming that the radar-based extracted rates of deformation will persist through the end of the century. Interpolation schemes (nearest neighbor) were then adopted to fill in the gaps between the PS pixels in each of the generated DEMs. The generated DEMs and the projected sea level rise were used to construct a bathtub inundation model (Dawson et al., 2005) for the investigated period with ten-year time steps (Table 2). The model estimates the distribution of the inundated areas within the Nile Delta throughout the investigated period (2010-2100) using the following equation:

$$I_n = (DEM + D_n) + (A_n) - SLR_n \quad (3.7)$$

Where  $D_n$  and  $A_n$  represent land deformation and accretion rates in the investigated number of years ( $n$ ) respectively,  $SLR_n$  is the sea level rise in  $n$  number of years, and  $I_n$  is an elevation index. The accretion rate was assumed to be negligible; the construction of the Aswan High Dam dramatically reduced the transport of sediments to the coastal areas (Shalash, 1982; Smith and Abdel-Kader, 1988; Syvitski et al., 2009). A pixel was identified as being inundated if its index value was negative and if it was connected to the sea.

The high-resolution sub-meter (pixel spacing: 12m; absolute horizontal and vertical accuracy: <10 m; relative vertical accuracy: 2-4 m; Rizzoli et al., 2012; Riegler et al., 2015) TanDEM-X digital elevation model was acquired from the German Aerospace Center (DLR). The Ellipsoidal TanDEM-X DEM heights were converted to orthometric heights using the 2.5 minute Earth gravitational model 2008 (Pavis et al., 2012). The absolute height accuracy of the TanDEM-X DEM for the study area was validated and calibrated using 50 benchmarks (Fig. 18a) with known elevations (reported accuracy resolution: 1 cm) extracted from scanned (1:25,000 and 1:10,000 scale) 1941–1946 topographic maps (War Office, 1941; Egyptian Surveying Authority, 1946). The elevation points were selected from areas that showed negligible to no change in elevation (<0.1 mm/yr) in the PSI results. The TanDEM-X elevations correlated well (Fig. 18b) with the reference point elevations ( $R^2 = 0.99$ ), but were found to be lower by 4.5 cm; they were adjusted (increased by that amount) accordingly.

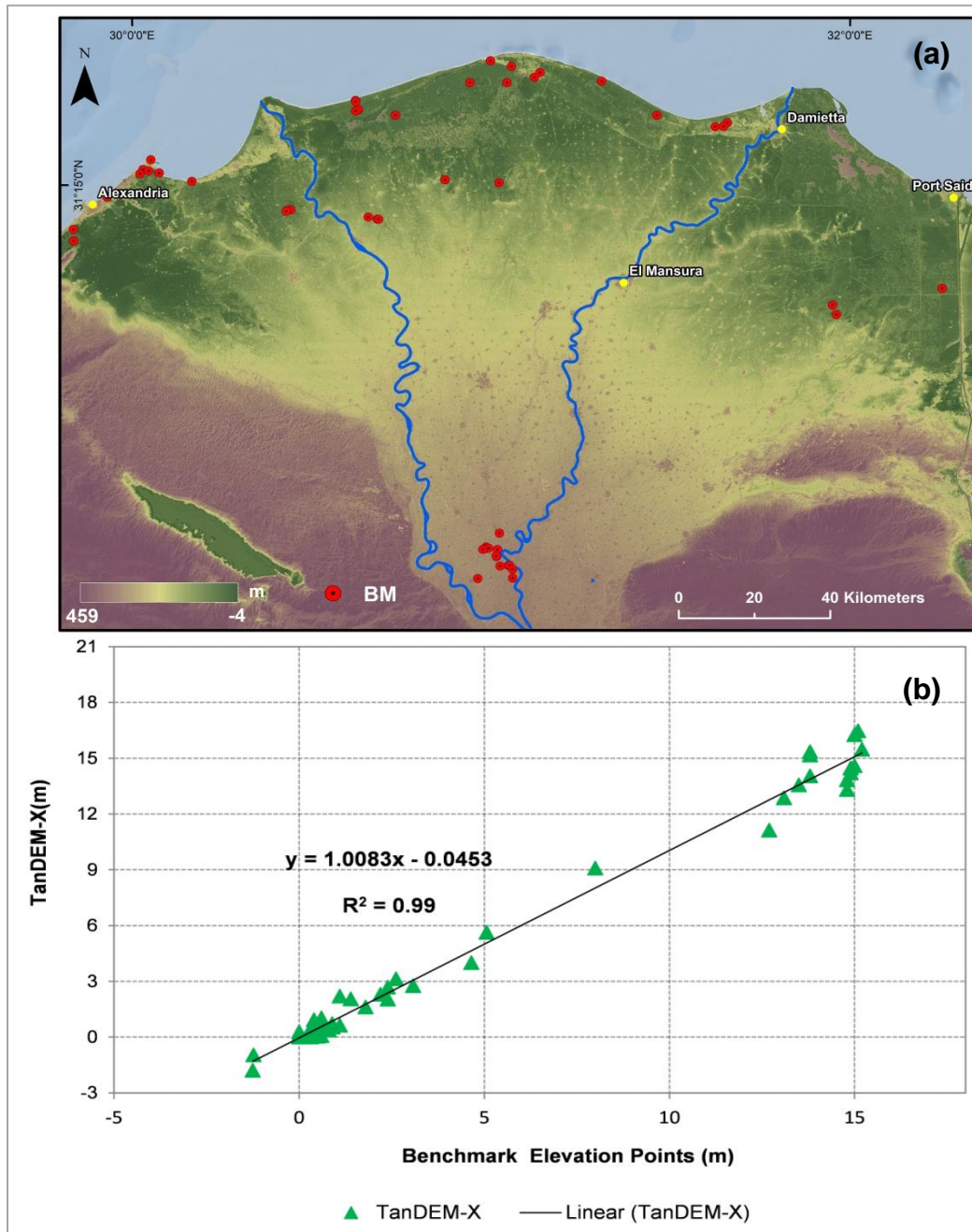


Figure 18: (a) Spatial distribution of the 50 benchmark (BM) elevation points, extracted from 1941–1946 topographic maps (War Office, 1941; Egyptian Surveying Authority, 1946), plotted on a TanDEM-X digital elevation model and used for its validation and calibration. (b) A plot of fifty TanDEM-X elevation points versus benchmark elevation points showing good correlations ( $R^2 = 0.99$ ) between the two datasets and slightly lower elevations (by 4.5 cm) for the TanDEM-X data.

Inspection of the TanDEM-X DEM reveals that the delta has a generally flat topography and low elevations that increase inland (away from the Mediterranean Sea). Only one-quarter of the Nile Delta has elevations exceeding 10 meters above mean sea level (a.m.s.l.) and over 3000 km<sup>2</sup> of its coastal and near-coastal lands (e.g., northern lakes of Manzala, Burullus and their surroundings shown in figure 1) lie below the mean sea level (Fig. 18a). Major coastal cities such as Port Said stand higher than their surroundings (Port Said city: up to 18 m a.m.s.l.; surroundings: 0-6 m a.m.s.l.).

The social and economic impacts of the projected sea level encroachment were evaluated by correlating (in a GIS environment) the sea encroachment simulation results, with land cover (Land Cover Classification System [LCCS; FAO, 2002]) and population (30 arc-seconds Gridded Population data of the World [GPWv4]; CIESIN, 2016) data (Fig. 19). The land cover classes of the FAO LCCS were regrouped into five major classes.

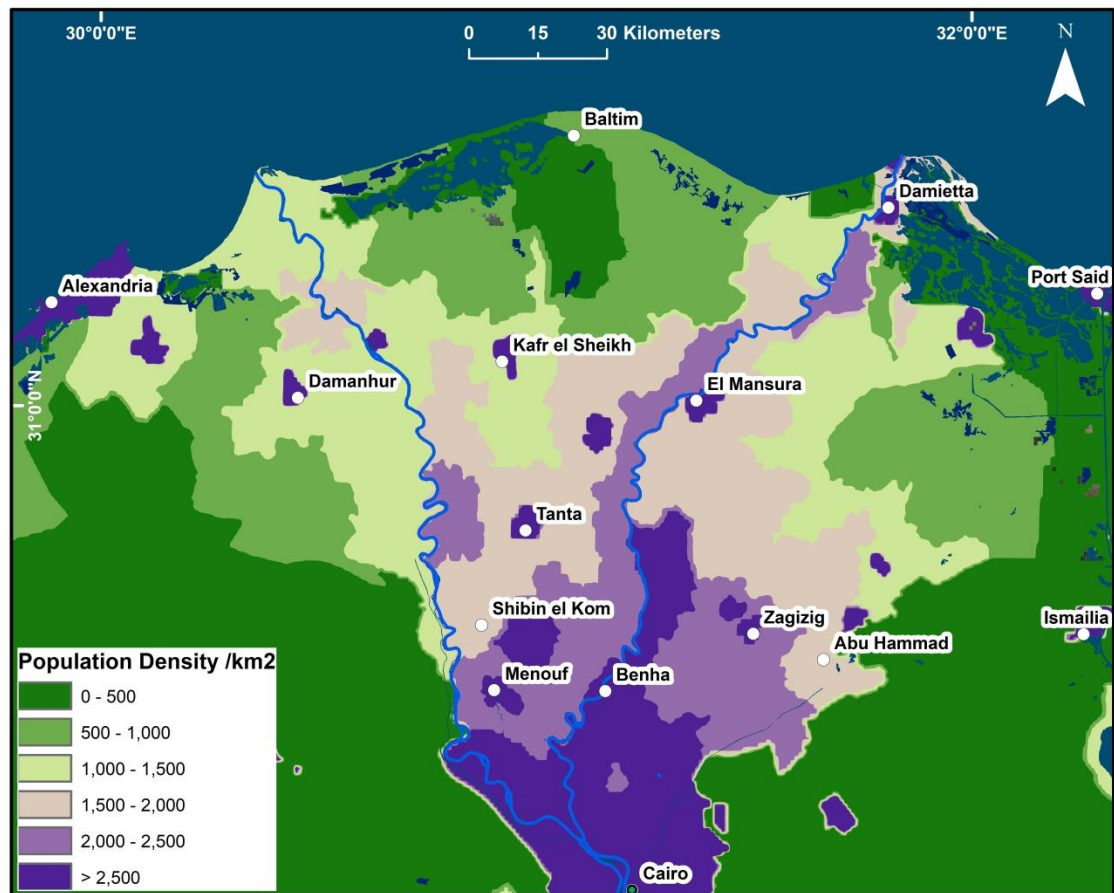


Figure 19: Population density estimates of the Nile Delta and surroundings from the Gridded Population data of the world ([GPWv4]; CIESIN, 2016)). The coastal cities of Alexandria, Damietta and Port Said are densely populated cities in the northern part of the study region. On the southern and central Nile Delta, dense population distribution is noted in El Mansura, Tanta, and Cairo cities.



## CHAPTER 4

### RESULTS AND DISCUSSION

#### **4.1 Introduction**

Deformation in deltas is a result of a combination of several drivers, although a single dominant process might account for the majority of the observed deformation. In this chapter, the land deformation of the Nile Delta is quantified using the PSI. The natural and anthropogenic processes and activities that influence the deformation processes including the spatial distribution of recent sediments via the paleochannels of the Nile River are discussed. The social and economic implications of the sea level rise are also investigated, and possible measures that could prevent the sea encroachment or lessen its impact are suggested.

The approaches adopted in this study and the findings provide better estimates for deformation rates and avoid many of the uncertainties associated with the previous approaches and estimates. Thus, my study provides more accurate delineation for areas susceptible to sea encroachment, and a better definition of factors controlling deformation.

#### **4.2 Paleochannel Delineation using High-Resolution DEM**

The DEM-derived map for the channel networks of the Nile Delta (Fig. 20) shows that the current active distributaries of the Nile River, Damietta and Rosetta,

are standing at relatively higher elevation than the surroundings. This is because of the deposition and buildup of coarser grained sediments forming natural levees on the river banks that stand higher than the surrounding floodplains (Said, 1993). Similarly, the delineated paleochannels and their bifurcations also show higher elevations compared to the surrounding floodplains.

The DEM derived paleochannels of this study match those of Wright and Coleman (1973), Ross et al. (1978), and Stanley and Clemente (2014). Using the contrast in the elevation of the Nile branches and their immediate floodplains, the now-defunct paleochannels (Canopic, Saitic, Sebennitic, Mendesian, Tanitic, and Pelusiac) that are shown in various historical documents and maps were identified (Fig. 16). The earlier maps that demonstrate the distribution of paleochannels in the Nile Delta did not adequately illustrate the spatial distribution of the defunct branches (Fig. 16). The data analysis in the present study shows a detailed and extensive network of channels that were not identified in the earlier works.

The termini of the current and former river Nile distributaries are areas of thick Holocene sediment accumulations (Stanley, 1988). In the presence of suitable geomorphological conditions, the slowing down of river flow velocities results in the deposition of distributary mouth bars and subsequent channel bifurcations (DuMars, 2002).

In the Nile Delta, thick accumulations of recent sediments have been noted on the eastern sections while the western part is underlain by relatively thin Holocene sediment deposits. This observation could be caused by the lesser number of sediment supplying Nile distributary channels in the west (Fig. 20), the general slope (gradient of flow shown by arrows in Fig. 21a) being towards the east, and coastal erosion by the E-W blowing wind (Frihy, 1988).

At the point where the Nile River loses its velocity and bifurcates into a new (distributary) channel, there is potential for sediment deposition depending on the slope and topography of the area. The flow direction analysis derived from the TanDEM-X DEM shows that the neighboring points at the bifurcation points (from the main branches or mini sub-branches shown in pink squares in figure 20) of the Mendesian, Sebennetic, and other main and minor branches of the Nile flow towards (the center of) these bifurcation points creating a favorable setting for sediment buildup and subsequently to compaction and subsidence. As stated earlier, the significance of identifying the paleochannel distribution in regards to the land deformation process in the Nile Delta relates mainly to the spatial distribution and thickness of recent sediments (further discussed in the sections below).

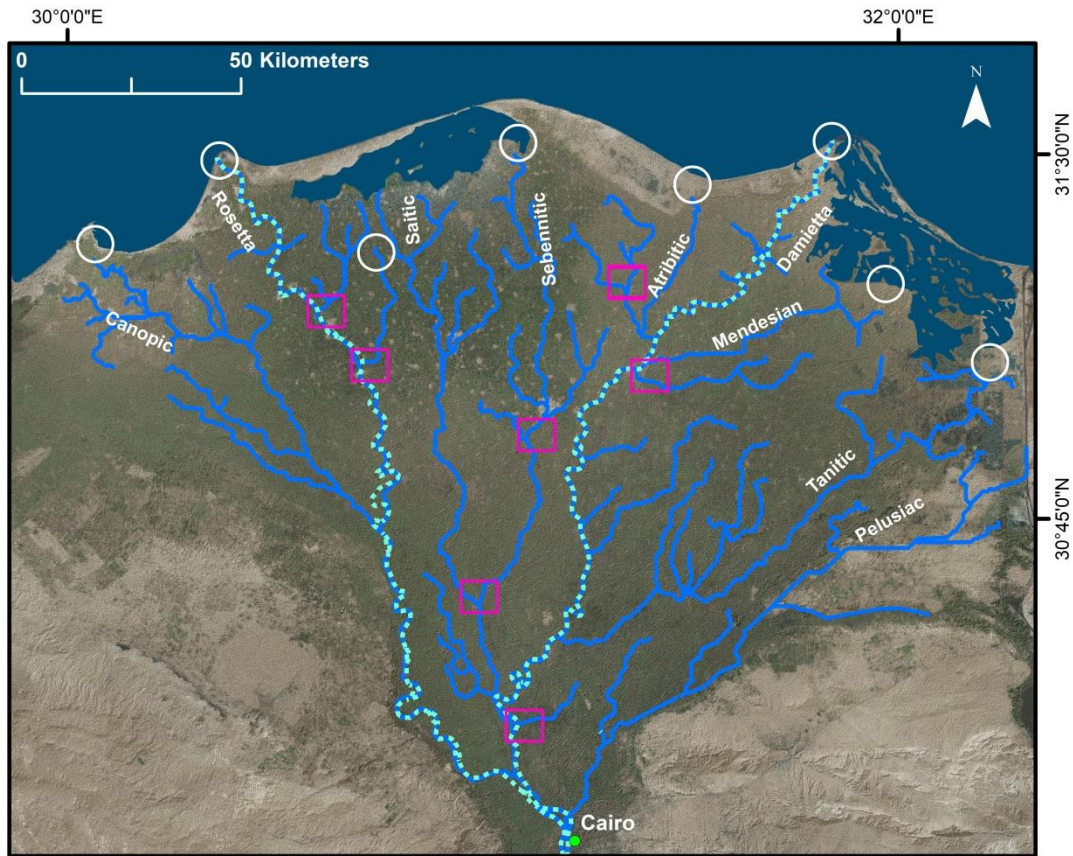


Figure 20: Paleochannel distribution extracted from the generated DEM (shown in blue color). The dotted light blue color represents the currently active branches of the Nile (Rosetta and Damietta). The white circles are representative of the terminus of the branches of the Nile distributaries where thick accumulations of sediments are anticipated. Also shown (in pink boxes) are some of the bifurcation points emanating from the main distributaries of the Nile.

### 4.3 Land Deformation Processes and Controlling Factors

The PSI analysis revealed regional deformational patterns, largely caused by natural processes and locally modified by recent anthropogenic contributions.

#### **4.3.1 Regional Deformational Patterns Caused by Natural Processes**

Regional patterns of subsidence (average rate:  $-2.4$  mm/yr; maximum rate:  $-9.8$  mm/yr) were observed in the northern sections of the delta (Fig. 21a, orange and red dots), compared to the southern delta, which shows slight to no uplift (Fig. 21a, average rate:  $0.4$  mm/yr; blue and cyan dots). Moving from north to south, a 20–40 km wide uplift zone is detected in central delta, an area that shows mean and maximum uplift rates of  $2.5$  mm/yr and up to  $7$  mm/yr, respectively (Fig. 21a). The maximum uplift rate is observed near the midpoint of the 20–40 km wide uplift zone. The northern boundary of the uplifted zone corresponds fairly well to the location of a previously mapped (Harms and Wray, 1990), east-west trending, extensively faulted, hinge line (Fig. 21a, black solid line and dotted line where inferred).

The hinge line marks the end of the passive continental margin of Africa and the beginning of the oceanic crust of the Mediterranean (Harms and Wray, 1990; Hussein and Abd-Allah, 2001). The location and extent of the hinge line was previously mapped using observations extracted from well logs, seismic reflection, gravity, and magnetic data. These studies identify the tectonic division of the region based on the depth and extent of the Moho depth/crustal thickness, crustal structures, and properties/reflection of the seismic waves (Harms and Wray, 1990; Saleh, 2012).

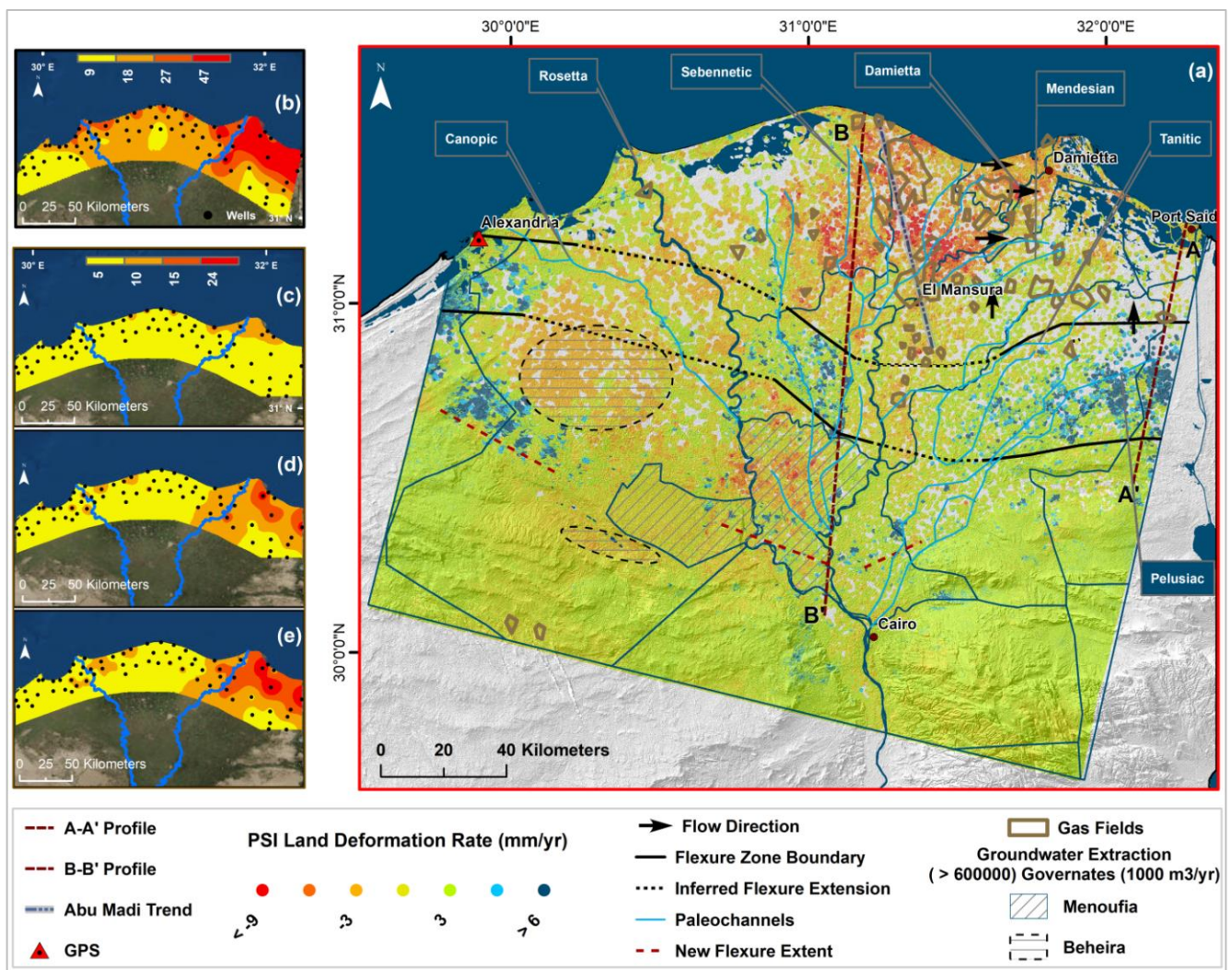


Figure 21: (a) Vertical component land deformation (in mm/yr) for the Nile Delta and surroundings extracted from 84 Envisat ASAR scenes acquired (2004–2010) along 3 tracks. Negative deformation values represent downward motion (subsidence), whereas positive deformation values represent upward motion (uplift). High uplift rates correlate with the distribution of a flexure zone in central delta, whereas high subsidence rates correlate with the distribution of young, thick, clay-dominated Holocene deposits and with areas experiencing high groundwater, oil, and gas withdrawal. The spatial distribution of the currently active and defunct Nile River branches (after Wright and Coleman, 1973; Ross et al., 1978) is also shown. Interpolated distribution of total thickness of Holocene sediments (b), cumulative thickness of sand (c), silt and mud (d), and clay (e) deposits in Holocene core samples (after Stanley et al., 1996) respectively.



Figure 22 is a plot of distance from coastline versus vertical motion (from PSI results) along two north-south trending profiles (Fig. 21a, A-A' and B-B'). The pixels north of the hinge line (towards the Mediterranean Sea) exhibit subsidence (average rates: A-A':  $-3.1$  mm/yr; B-B':  $-4.4$  mm/yr), whereas those south of the hinge line and within the uplifted zone display uplift patterns (average uplift rates: A-A':  $3.9$  mm/yr, B-B':  $1.7$  mm/yr). Moving south along the profiles, the uplifted zone gives way to a near-stable to slightly uplifted areas (A-A':  $1.4$  mm/yr; B-B':  $0.8$  mm/yr).

Similar deformational patterns have been reported for the Mississippi and Amazon Deltas based on geodetic (GPS) data analysis and modeling (Jurkowski et al., 1984; Driscoll and Karner, 1994; Blum et al., 2008). Using GPS measurements (Fig. 23), Jurkowski et al. (1984) documented three styles of deformation for the time period 1934 to 1969 along a 300 km, north-south trending profile that extends from the Gulf of Mexico coastline and New Orleans in the south to Jackson in the north (Fig. 23): (1) subsiding areas (rate:  $-7$  to  $-10$  mm/yr; width: 75 km) extending from New Orleans and areas to the south towards the gulf coast, (2) an uplifted zone (rate:  $3.4 \pm 0.5$  mm/yr; width:  $\sim 200$  km) starting some 20 km north of New Orleans and extending 20 km south of Jackson, and (3) stable areas (width:  $\sim 20$  km) near Jackson.

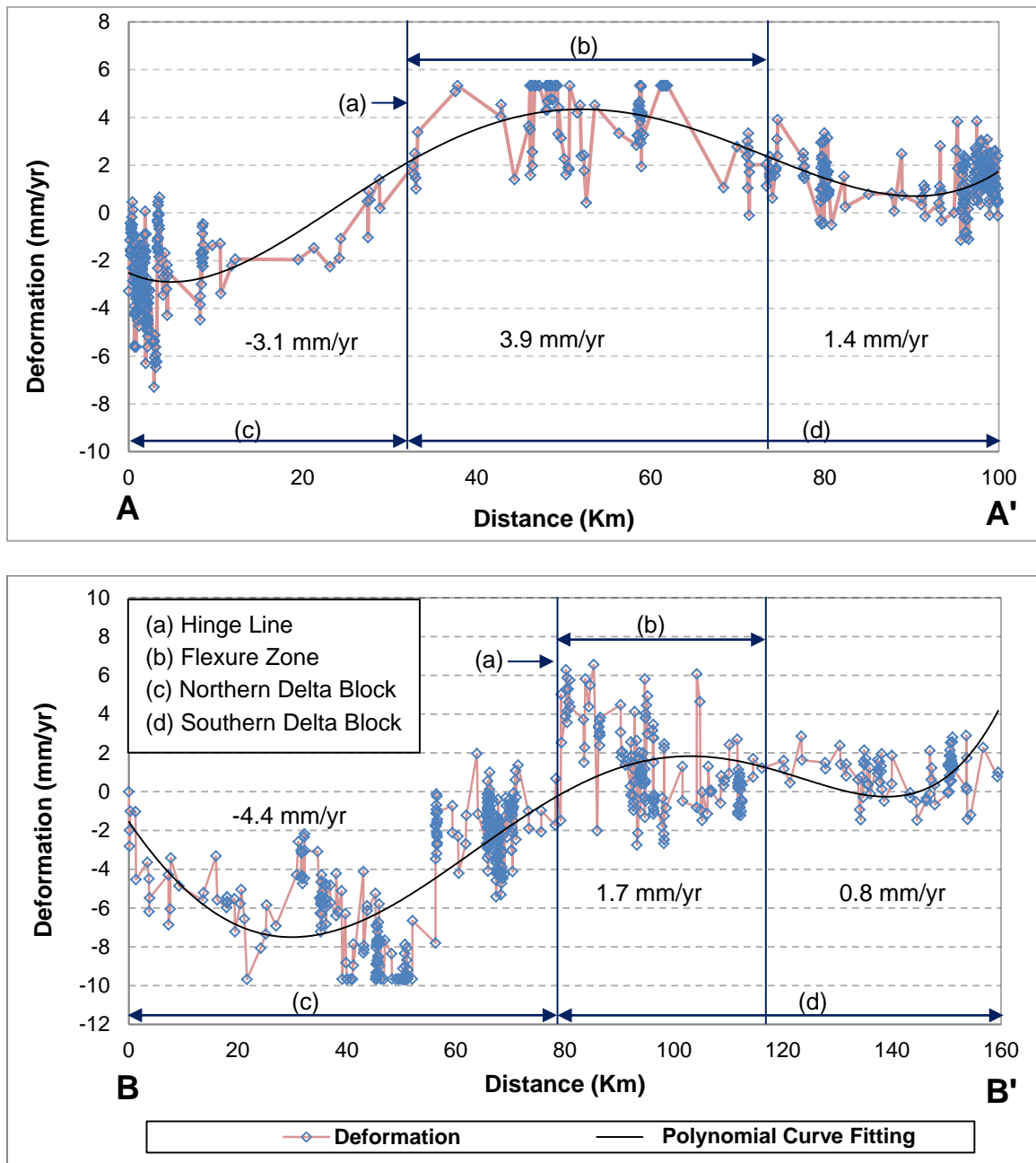


Figure 22: X-Y plot for distance versus deformation rates (extracted from the PSI analysis) along two north-south trending profiles (A-A' and B-B') showing the uplift and subsidence deformation patterns associated with flexural isostatic deformation. A hinge line (a) separates the oceanic crust (c) from the passive continental margin (d). The subsiding oceanic crust is flanked by the flexure zone (b), an uplifting stretch of land with a minimum width of 20–40 km.



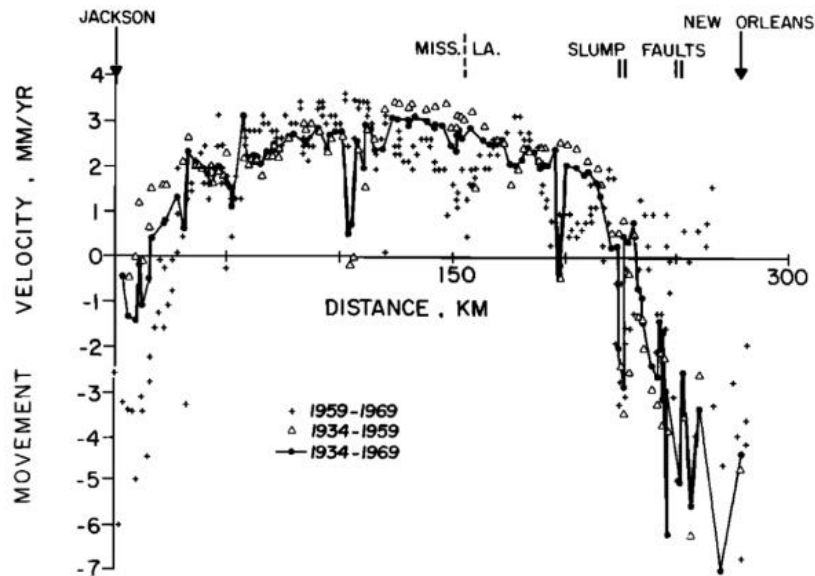


Figure 23: GPS based velocity (in mm/yr) plot of the Jackson to New Orleans profile using elevation changes determined by comparing the GPS data for time interval 1934 to 1969 (Jurkowski et al., 1984).

In the present study, the regional radar-based uplift and subsidence patterns described above is attributed to flexural isostatic deformation. In river deltas, the progressive buildup of the delta and the subsequent sediment accumulation and load at the continental margins produces a downward flexure of the lithosphere that is filled with sedimentary rocks. The sediment buildup and load on the oceanic crust eventually lead to the subsidence of the underlying crust and the uplifting of the flanking regions. The long-term subsidence process further produces an accommodation space for the prograding sediments (Fig. 24) (Walcott, 1972; Watts, 2001).

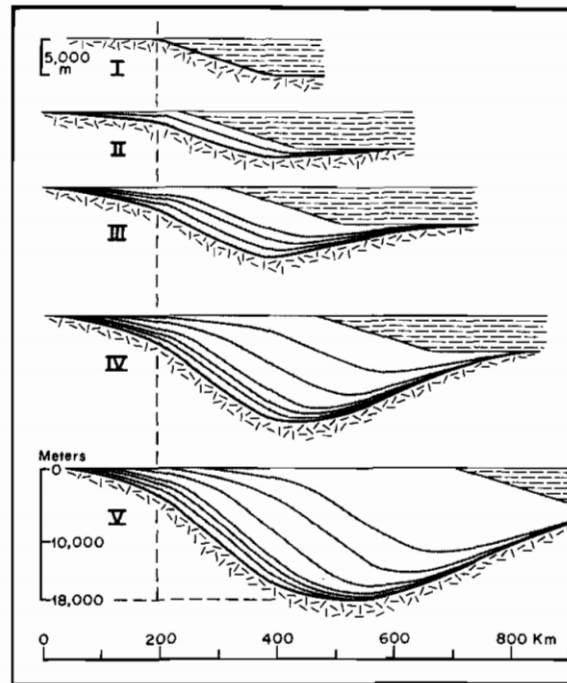


Figure 24: The effect of progressive sediment loading at a continental margin. The increasing sediment load at the margin eventually produces a downwarp by flexure (Walcott, 1972)

The passive continental margin of Africa subsided from the Jurassic Period onwards due to isostatic loading creating an accommodation space and, consequently, the deposition of relatively younger sediments on the oceanic crust (Harms and Wray, 1990; Marriner et al., 2012). In this interpretation, a hinge line separates the passive continental margin (southern delta block) from the oceanic crust (north delta block) and the subsiding oceanic crust is flanked by an uplifting stretch of land (flexure zone). As stated above, flexural isostasy models for river deltas balance subsidence in

the oceanic crust side by uplift (bulge) in the flanking regions. In this model, the lithosphere is assumed to be elastic (Walcott, 1972; Watts, 2001).

Several studies (Warne and Stanley, 1993; Abdel-Fattah and Tawfik, 2015) proposed and/or hypothesized flexural deformation in the Nile Delta, but did not provide comprehensive evidence in support of their suggestion, did not identify its mode of deformation, and did not delineate its exact spatial extent. Stanley and Warne (1993) estimated the position of the hinge line (length from the hinge line to the coast - 15 km wide in the north-central sector, 22 km in the northwestern plain, and 45 km wide in the Manzala lagoon region), through spatial correlation of the thickness of the Holocene beds and the ensuing subsidence pattern retrieved from the analysis of core samples. Areas north of the hinge line are underlain by thick Holocene sediments and show high subsidence rates (up to -5 mm/yr). Guided by the PSI-based general patterns of deformation across the entire delta in this study, the location of the hinge line was refined and delineated the areal extent of the flexure zone (Fig. 21a). The northern extension of the flexure zone was delineated as a fairly narrow zone (<3 km) that separates two contrasting deformation patterns, subsidence to the north, and uplift to the south. Mapping the southern boundary of the flexure zone is more challenging given that it does not separate highly contrasting deformational patterns as is the case with the northern boundary, and by the apparent modification of the original uplift by groundwater extraction-related subsidence. The southern boundary was mapped as a 1–3 km wide, stretch of land that separates

uplifted ( $> 4.6$  mm/yr) areas to north from near-stable ones ( $< 1.3$  mm/yr) in the south (Fig. 21a, black solid line and black dotted line where inferred) but could potentially extend as far south as the dotted purple line on the figure if all of the uplifted areas were included in the mapped flexure zone. If true, its width could reach up to 60 km.

Inspection of figure 21a also shows that the subsidence in the northern delta is not evenly distributed. High rates are observed in the northeastern sections (up to  $-8.9$  mm/yr) compared to the northwestern delta. This apparent asymmetry is attributed to variations in sediment thickness, age, and composition (Figs. 21b, 21c, 21d, and 21e). In general, the Holocene sediments in the northeastern delta are thick (average thickness in 13 wells: 31 m), and rich in their silt and clay content (average thickness in 13 wells: silt: 10.3 m; clay: 14.2 m; sand: 6 m). By comparison, their counterparts in the northwestern delta are thin (average thickness in 17 wells: 15.6 m), and largely composed of sand- and clay-sized sediments (average thickness in 17 wells: silt: 1.2 m, clay: 8.2 m; sand: 5.7 m).

The sediments in the northeastern delta ( $>5$  m thick) are apparently younger in age ( $<3500$  years) than those in the central and western delta (Becker and Sultan, 2009). Dewatering of compressible clay and silt deposits have been found to be the leading driving reasons for the observed subsidence in many areas around the world (Othman et al., 2018) and the intensity of these processes declines with increasing age

of these sediments (Marriner et al., 2012). Similar models to explain the observed subsidence in large sectors of the Nile Delta are advocated in this study.

At present, there are only two Nile channels that are active (the Rosetta and Damietta branches), but there were far more active channels—at least seven at the beginning of the Holocene (Fig. 16). Five channels (the Pelusiac, Tanitic, Mendesian, Damietta, and Rosetta branches) were active as recently as 1500 to 2500 years ago (Stanley and Warne, 1993), all of which, with the exception of the Rosetta branch, are in the northeast section of the delta (Figs. 20 and 21a). The presence of young, thick clay and silt dominated deposits in the northeastern part of the Nile Delta described above and displayed in Figures 21b, 21d, and 21e correlates well with the high subsidence rates inferred from the radar interferometric approach (Fig. 21a). These sediments were deposited by the currently active Damietta and the now-defunct younger channels. Similarly, the terminus of the now-defunct Nile distributaries (Fig. 20) where thick accumulations of recent sediments are noted also exhibit high subsidence rates. Distributary bifurcation points show higher subsidence rates (shown in pink boxes in figure 20) which is ascribed to the change in river flow dynamic that led to the deposition of compressible younger sediment along those points.

The Sebennetic branch within the north-central section of the Nile Delta existed from 7500 to 3000 B.P. and is the oldest of the Nile Delta's distributaries (Arbouille and Stanley, 1991). The Canopic branch on the northwestern extreme of

the Nile Delta dried up around the 5th century AD (Said, 2002). The increased number of channels in the eastern delta compared to the west is due to tilting (sloping) and sinking of the delta towards the northeast during the Pleistocene/Miocene that was triggered by sediment load and fault displacement; the tilting created a conducive environment for directing the Nile branches towards the northeast and caused massive deposition of sediments during the Holocene (Stanley, 1988, 1990; Said, 1990; Stanley and Warne, 1993; Siegel et al., 1995).

#### **4.3.2 Local Deformational Patterns Caused by Anthropogenic Factors**

Examination of figure 21a reveals that the general regional patterns described above were apparently modified (enhanced or reversed) locally by anthropogenic factors, namely groundwater and gas extraction. High extraction rates of groundwater, oil, and gas resources cause changes in the pore pressure and effective stress of the aquifers, leading to compression and subsidence (Feng et al., 2008).

Faced by overpopulation and increasing demands for fresh water, and food supplies and given the limited precipitation (average annual precipitation: ~50 mm; Mahmoud, 2014), and decreasing surface water resources (Hossen and Negm, 2016), Egypt has embraced a program to increase the usage of its groundwater resources to reclaim its deserts and to supplement its surface water irrigated areas within the delta. Groundwater extraction rates increased exponentially throughout the past three decades (Dawoud et al., 2005; Mohamed and Hua, 2010), a trend that is expected to

continue in the upcoming decades (Ministry of Agriculture and Land Reclamation, 2009).

The largest extraction of groundwater is reported in the Menoufia governate ( $654 \times 10^6 \text{ m}^3/\text{yr}$ ) within the delta and from the Beheira governorate ( $645 \times 10^6 \text{ m}^3/\text{yr}$ ) west of the delta (Hefny and Sahta, 2004), the area where the largest desert reclamation project was implemented. Between years 2003 and 2012,  $2100 \text{ km}^2$  were reclaimed at the western fringes of the Nile Delta using groundwater extracted from the sand and gravel-dominated Nile and Moghra aquifers; both aquifers have intercalations of clay and silt layers (Dawoud et al., 2005; El Tahlawi et al., 2008). It has been shown that intense pumping from compositionally similar aquifers produces consolidation and compaction of the compressible clay and silt units due to change in pore pressure and vertical effective stress within the aquifers and hence results in subsidence (Poland and Davis, 1969; Leake, 1990). Similar conclusions were inferred from InSAR analysis of Envisat and PALSAR (Phased Array type L-band Synthetic Aperture Radar) over two large agricultural areas in San Joaquin Valley, California, that rely intensively on groundwater from the clay- and silt-dominated Central Valley aquifer system (Faunt et al., 2015). The finding of the PSI analysis shows subsidence rates of up to  $-6 \text{ mm/yr}$  and  $-9.7 \text{ mm/yr}$  over parts of the Beheira (Fig. 21a, horizontal strips outlined by thick dotted brown line) and Menoufia (Fig. 21a, gray diagonal lines enclosed by thick dark black) governorates, respectively. The observed

accelerated subsidence rate in these two districts is attributed to the compaction of compressible sediments within the aquifers due to excessive groundwater extraction.

Natural gas withdrawal within the Nile Delta and off its shoreline has been on the rise over the past two decades (change in production between 1990–2000: 13.05 BCM; 2000–2005: 22.63 BCM; 2006–2010: 20.1 BCM; U.S. Energy Information Administration, 2014: Fig. 25), making Egypt the second largest producer of natural gas in Africa (Bahgat, 2012). The locations of the production oil and gas fields that are in operation since the mid 90's are outlined in figure 21a (Dolson et al., 2002; U.S. Energy Information Administration, 2014).

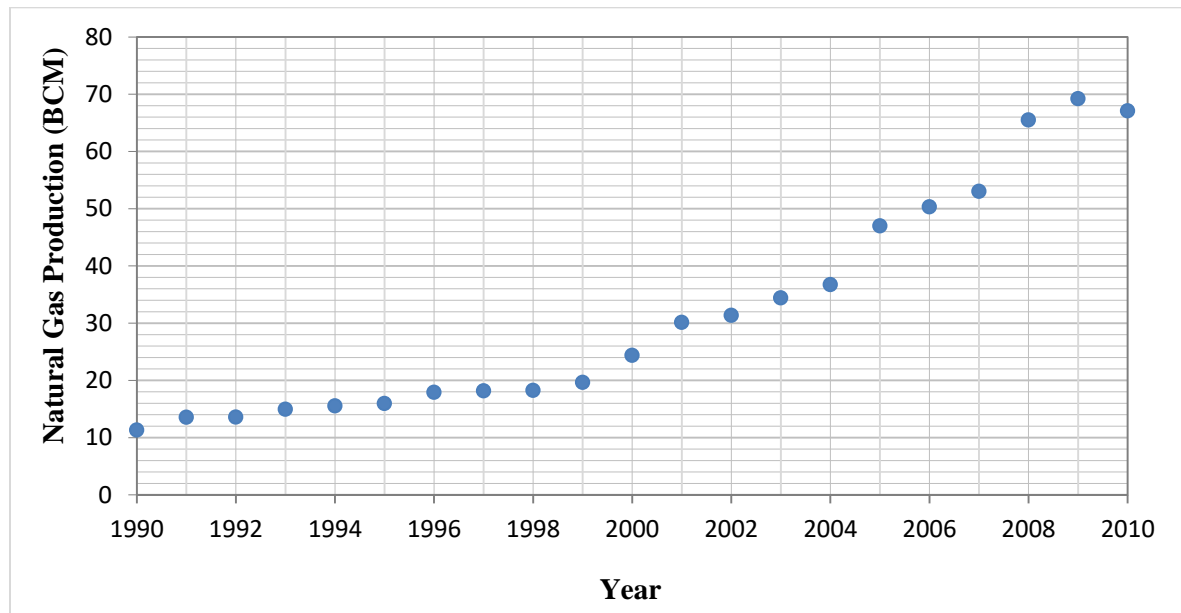


Figure 25: Natural gas withdrawal within the Nile Delta and off its shoreline over the past two decades (U.S. Energy Information Administration, 2014).



Most of the natural gas in the Nile Delta extracted from Plio-Pleistocene to Miocene age clastic reservoirs (Keshta et al., 2012; Younes, 2015). The largest gas fields in the Nile Delta mine the Abu Madi formation, a series of thick sands interbedded with thin shale (Rizzini et al., 1978; Kassab et al., 2015). Similar to the processes that initiate land deformation in high groundwater extraction regions, excessive natural gas extractions also change the pore pressure within the gas producing formations and ultimately result in subsidence (Doornhof et al., 2006). Figure 21a shows a spatial correspondence between the locations of high subsidence (up to  $-9.7$  mm/yr) and the distribution of gas fields (Fig. 21a, areas outlined by solid brown polygons) including the Abu Madi gas trend (Fig. 21a, northwest-southeast trending dotted line) in the study area.

#### **4.4 Sea Level Rise**

The approach implemented in this research applies present-day subsidence rates, accounts for the spatial variations in deformation across the entire delta, uses digital elevation models with high spatial and vertical resolution, and calibrates the satellite-based DEM against benchmark elevations.

The maximum relative sea level rise by the end of this century was estimated at about 1.3 meters if the maximum subsidence rate detected over the coastal areas ( $-9$  mm/yr) was adopted and a sea level rise of 0.44 m was considered. Assuming that the current natural and anthropogenic deformation rates will persist throughout the

21st century and that no engineering structures will be implemented to combat the sea encroachment, the simulations (Fig. 26a) show that by the year 2100, 2660 km<sup>2</sup> (13.3% of the total delta area) in the northern Nile Delta will be submerged.

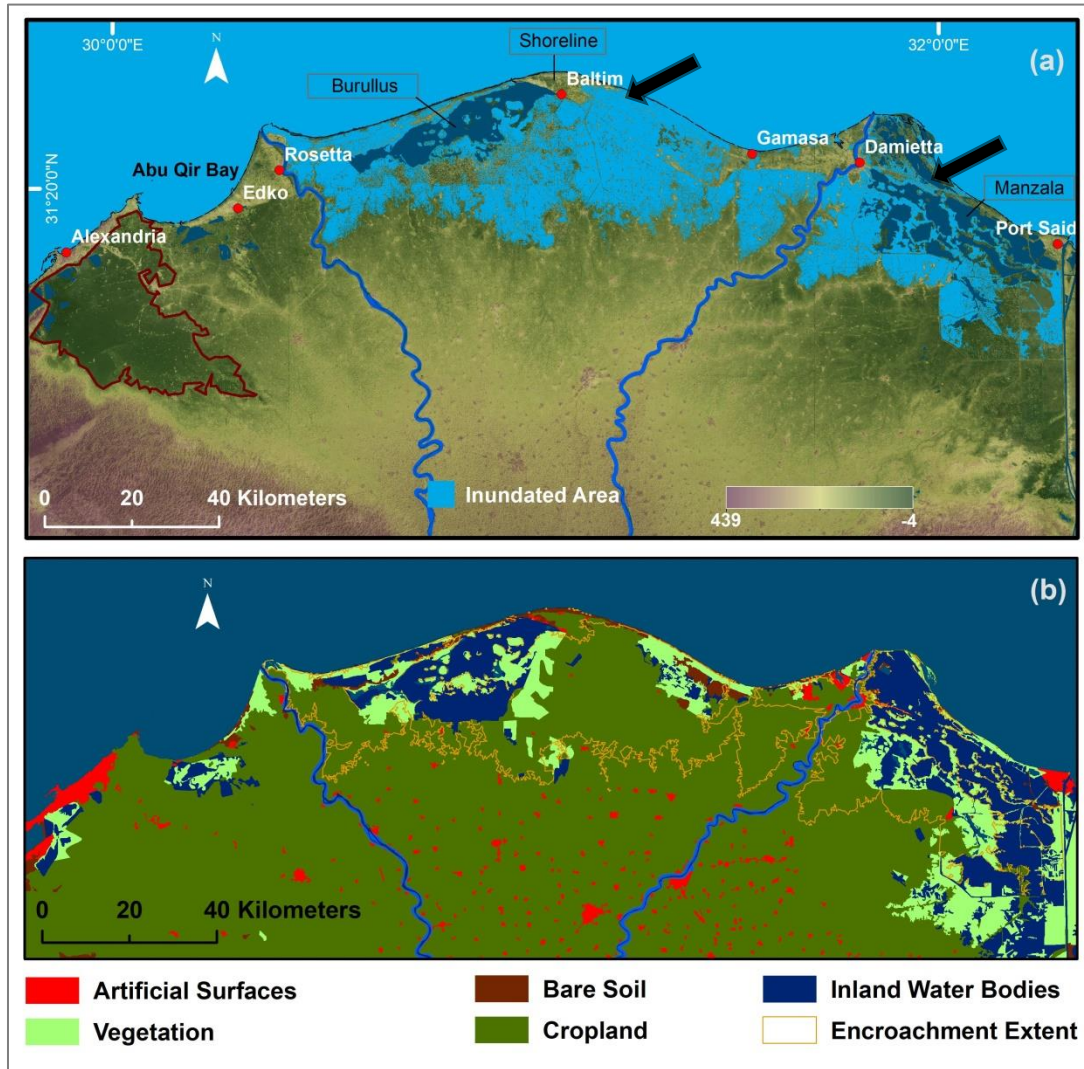


Figure 26: (a) The projected distribution of inundated areas (light blue colored areas) in the Nile Delta by the year 2100. The simulation is based on the RCP 2.6 model eustatic sea level rise projections and the extracted PSI-based deformation rates. (b) Social and economic impact of the sea encroachment is based on the land cover and population density datasets of the Nile Delta. The extent of the encroachment is shown in light yellow.

The inundated area is largely (68 %; 1798 km<sup>2</sup>) cropland and aquaculture farms (Figures 26a and 26b, 4%; 106 km<sup>2</sup>). Currently, about 2 million citizens reside within the projected inundated area (CIESIN, 2016); assuming that the current annual population growth rate of 2% (World Bank, 2017) persists throughout the 21<sup>st</sup> century, about 5.7 million people will be affected. The estimates for inundated areas in this study are less than half of those advocated by Hereher (2010). He estimated that 6,165 km<sup>2</sup> of the Nile Delta (30% of the total delta area) will be inundated, by applying an average Holocene subsidence rate of 5 mm/yr and a relative sea level rise of 1 m (Fig. 27).

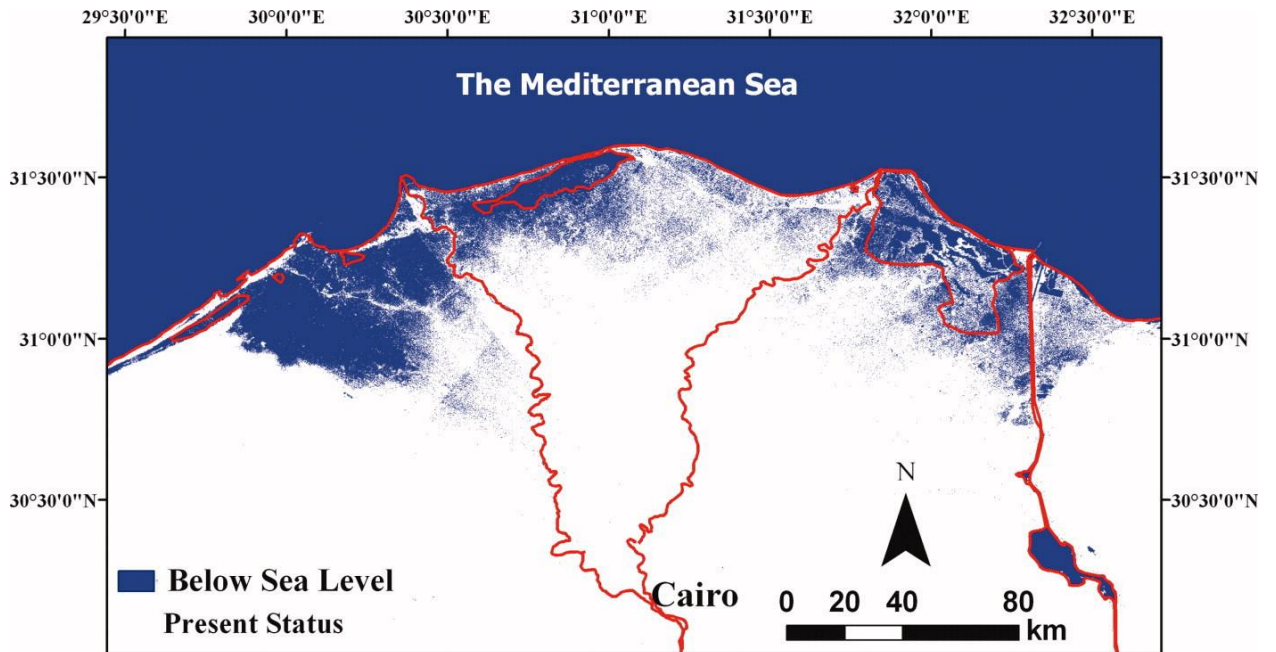


Figure 27: Sea encroachment in the Nile Delta (inundated areas are shown in blue color) calculated using 1 m relative sea level rise projection by the year 2100 (after Hereher, 2010).

Figure 26a shows that more areas will be submerged in the central and eastern delta compared to the western delta, contrary to earlier findings that did not take into consideration the spatial variability of the deformation rates and relied on coarse-resolution digital elevation models (Hereher, 2010; Hasan et al., 2015). The current elevations (from Tandem-X DEM and/or topographic sheets) of the submerged areas range from 2 m below to 3 m above sea level. Examination of the model outputs (inundated areas every ten years; Table 2) shows that sea encroachment progressed through two main inlets (Fig. 26a, black arrows), the lowlands approximately 25 km east of Baltim, and the coastal edges of Manzala lagoon (Fig. 26a). The inland progression of water in these areas was facilitated by the high subsidence rates (Fig. 21a) and the absence of natural and man-made barriers like coastal ridges, sand dunes, and artificial engineering structures.

The largest encroachment ( $\sim 1870 \text{ km}^2$ ) is expected to occur west of the Damietta branch, the area witnessing high subsidence rates (Fig. 21a, up to  $-9.7 \text{ mm/yr}$ ) presumably due to presence of thick (up to 22 m), recent, silt- and clay-rich sequences, and high gas extraction rates. Similarly, a stretch of  $780 \text{ km}^2$  along the coastal edges of the wetlands of Manzala will be submerged by the year 2100 mainly due to the moderate to high subsidence rates (Fig. 21a, up to  $-9 \text{ mm/yr}$ ), coupled with the absence of natural or artificial barriers.

The role that natural and artificial barriers play in protecting the inland lowlands from sea encroachment at present and possibly by the end of the 21<sup>st</sup> century is demonstrated in areas to the north of Baltim and northeast of Burullus, areas south of Alexandria and Abu Qir, and lowlands west of the Rosetta branch (Figs. 26 and 28).

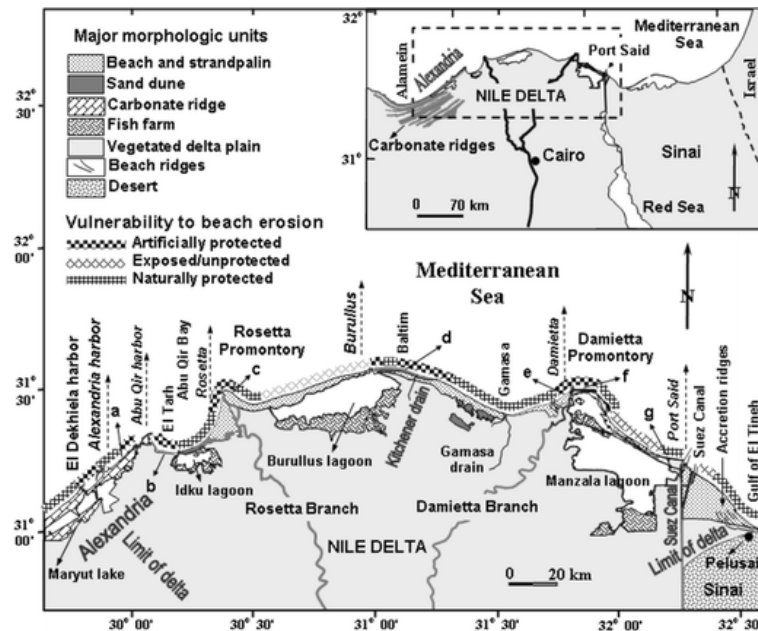


Figure 28: Major morphologic units on the coast of the Nile Delta (Frihy et al. 2003, 2010)

The areas north of Baltim are shielded from sea water inundation by a stretch of east-west trending sand dune field (width: up to 5 km, length: 25 km; minimum elevation: 5 m). Even though large swaths of land south of Alexandria and Abu Qir have elevations below sea level (Fig. 26a, brown polygons), a meager coastal tract of land ( $<10 \text{ km}^2$ ) will be affected by sea encroachment primarily due to the presence of

hard-to-erode coastal chain of carbonate ridges (at least 2 m high) and negligible to zero subsidence rates (Fig. 26a) over these ridges.

One cause of concern is the area south of Abu Qir Bay (Fig. 26a) that is dominated by Nile floodplain deposits. This part has thick Holocene deposits (up to 13 m thick) supplied by the Canopic branch and is experiencing moderate subsidence rates (up to  $-3.5$  mm/yr). There are almost no natural protective cover/elevated areas near the coast, and only an area 1 km wide with a maximum elevation of 2 m separates this large swath of lands with below-sea level elevations from the coast. The government of Egypt has constructed sea walls (Figs. 28 and 29) in some sections of this and other possible inlets (Frihy et al., 2010) but more work still needs to be done to avert this impending catastrophe.



Figure 29: Protective sea wall with elevations of more than 2 m constructed at the Damietta promontory (Hereher, 2009).

The ridge-like elevated flanks of both the Damietta and Rosetta branch have acted as hindering dams by limiting the inland progression of sea water (Fig. 26a). On the Rosetta branch, the pattern of the extent of the encroachment area mostly follows the meandering pattern of the river branch and these high flanks seem to be the reason why the flooding did not extend to the low-lying areas west of the Rosetta branch. The flood inlet/entry zones for the two major flooded areas to the east and west of the Damietta branch are quite different and are not interconnected with one another. This again shows the dam like role the elevated flanks played in this model.

Table 2: The estimated areal extent of the projected inundated areas in the Nile Delta throughout the investigated period (2010 – 2100) using a bathtub model and decadal time steps

<b>Year</b>	<b>Area affected (km<sup>2</sup>)</b>
2010	0
2020	0
2030	44
2040	97
2050	734
2060	879
2070	1360
2080	1664
2090	1789
2100	2660

## CHAPTER 5

### MODEL EVALUATION AND LIMITATIONS

#### 5.1 Introduction

Several factors affect the accuracy and reliability of the deformation rate estimation using the PSI technique as well as the sea encroachment simulation model. One such factor is the length of duration of the repeat cycle of the Envisat satellite (35 days) that contributes greatly to the temporal decorrelation of the SAR images due to thick vegetation cover in the Nile Delta. This, in turn, results in the generation of poor quality interferograms that ultimately affect the accuracy of the deformation estimate. The quality of the PSI deformation estimate will affect the accuracy of the sea encroachment simulation model. In the following section, the sources of uncertainties and the approach used to validate the accuracy of the deformation estimate, and sea encroachment simulations are discussed.

#### 5.2 Model Evaluation, Limitations, and Assumptions

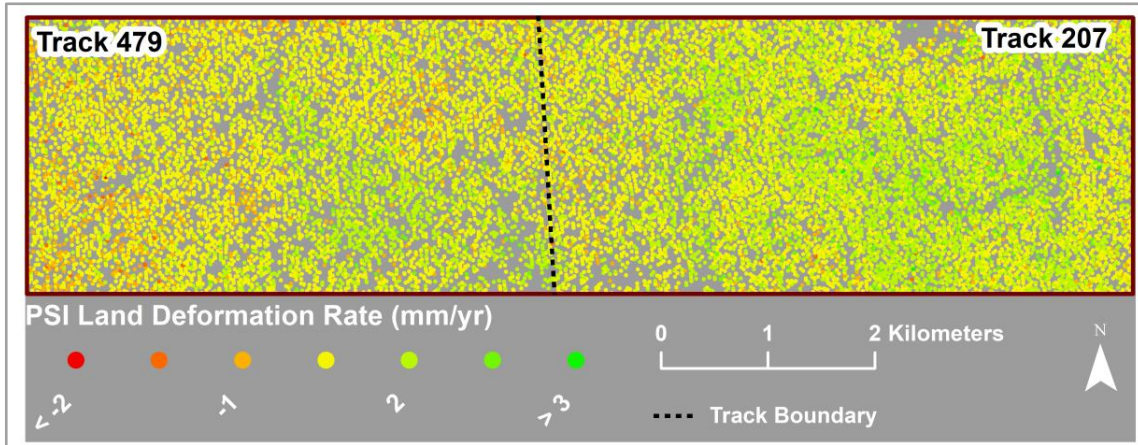
The validity of the projected inundation model results by the end of the 21<sup>st</sup> century (Fig. 26) depends on: (1) the accuracy of the extracted deformation rates, and (2) the validity of the assumption that the factors controlling land deformation at present, the extracted deformation rates, and the selected sea level rise rates will persist throughout the investigated period. To investigate the validity of the PSI analysis (Fig. 21a), the continuity of the deformation signal along east-west trending



profiles across track boundaries was checked. Specifically, from the GPS referenced track 479 to the adjacent calibrated non-overlapping parts of track 207 (Fig. 30a) and from track 207 to track 436 (Fig. 30b). The PSI results were also compared with the GPS records from the south Cairo station. Figures 30a and 30b show a smooth and uninterrupted transition across scene boundaries indicating that the adopted normalization procedures were effective. The reported deformation rates from the GPS station near Cairo and the extracted rates from the nearest two PS points were found to have similar values (deformation rates: GPS station: -1.1 mm/yr; PS points - 1.4 mm/yr, -1.1 mm/yr), further supporting the validity of the PSI results. The absence of additional GPS station records hinders precise assessment of radar-based deformation rates.

Significant variations in deformation rates throughout the investigated period are anticipated, if the deformation is caused by anthropogenic factors, and negligible variations if caused by natural drivers. The latter, but not the former variations, occur at much longer time spans (thousands to tens of thousands of years; Marriner et al., 2013). Several recent developments, including the new gas discoveries in the Nile Delta (Ghassal et al., 2016) as well as the progressive increase in groundwater extraction over the past three to four decades (Mabrouk et al., 2013) within the delta and in its surroundings suggest that the anthropogenic-related deformation is likely to intensify with time, so will the inundation in northern delta.

**(a) Box A (shown in Fig. 13a)**



**(b) Box B (shown in Fig. 13a)**

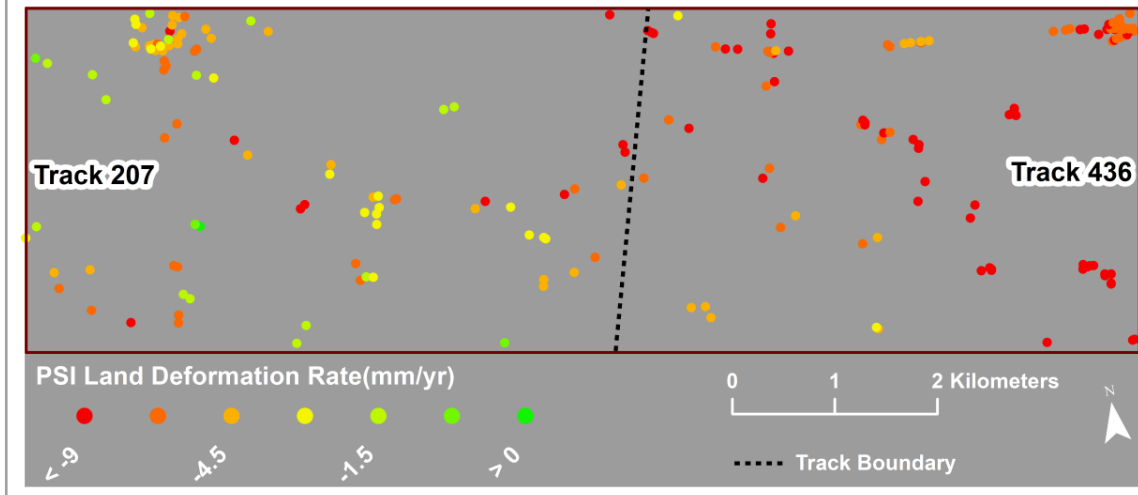


Figure 30: East-west trending profiles showing a smooth and uninterrupted transition in deformation signal across adjacent Envisat scene tracks. (a) Tracks 479 and 207. (b) Tracks 207 and 436. The locations of the profiles are plotted on Fig. 13.

A conservative rate for sea level rise estimate from the IPCC's RCP 2.6 model was adopted for simulations in the present study but with higher sea level rise scenarios (e.g., RCP 8.5 model: average:0.75 m; maximum: 0.98 by the year 2100), it

is foreseeable that additional lands will be inundated in northern delta. Another potential source of error in the methodology of the present study could arise for the interpolation of the extracted individual PS deformation ‘to fill the gaps’ in areas where no coherent PS were identified. Thus, the accuracy of the adopted approach could depend, in part, on the availability and density of PS points as well.

## CHAPTER 6

### CONCLUSIONS AND FUTURE DIRECTIONS

The PSI method was applied to a stack of 84 Envisat ASAR scenes, acquired between 2004 and 2010 over the entire Nile Delta of Egypt and surroundings, to assess the spatial and temporal land deformation across the study area. A high amplitude dispersion threshold value of 0.4 was used for the initial selection of PS points which enhances the identification of PS pixels located outside of the urban centers. The extracted deformation rates were correlated with relevant spatial datasets to constrain the natural and anthropogenic factors that could have caused the observed deformation. Moreover, the areas that are susceptible to sea encroachment by the end of the 21<sup>st</sup> century were identified and assessed the potential social and economic impacts of the projected sea encroachment using a combination of deformation estimates from the PSI analysis, a high-resolution digital elevation model, projected sea level rise values, land cover, and population density datasets. To best of my knowledge, this study is the first of its kind to investigate the deformation pattern over an entire delta, as well as to model flexural deformation and its spatial extent in river deltas using radar interferometry. The findings are summarized below:

1. Deformation in the Nile Delta is influenced by both regional natural and local anthropogenic controls that are at times superimposed on one another.

2. Regional deformation in the study area is principally controlled by natural phenomena such as isostatic adjustment and natural compaction of Holocene sediments (up to  $-8.9$  mm/yr) depending on the sediment thickness, age, and composition, yet anthropogenic factors (e.g., fluid extraction) can cause added local deformation in the region.
3. The northern and southern parts of the Nile Delta are separated by an east-west trending hinge line and a wide flexural uplift zone (minimum width: 20-40 km) that separates the highly subsiding northern block (maximum rate:  $-9.8$  mm/yr) from the stable or slightly uplifting (average rate: 0.4 mm/yr) southern delta block.
4. A maximum uplift rate of 7 mm/yr was detected within the flexural uplift zone and a gradual decrease in uplift rates was observed in areas south of the flexure zone.
5. The sea level rise impact simulation indicates that by the year 2100, 2660 km<sup>2</sup> in the northern delta will be inundated by sea water and the lives and livelihoods of nearly 5.7 million people will be affected if the extracted deformation rates persist and the mean RCP 2.6 global mean sea level rise (0.44m) was adopted. Natural (ridges, fluvial geomorphological features etc.) and artificial structures, in combination with the land deformation process, are expected to play a major role in the inland progression of sea water.

6. The continuity of the deformation rates calculated using Envisat ASAR dataset over a 7-year interval (2004 - 2010) should be reassessed using data from the recently launched (April 2014 and April 2016 Sentinel 1A and 1B respectively) Sentinel-1 missions. One major advantage the Sentinel SAR datasets have over Envisat is short temporal resolution (6-day repeat cycle for Sentinel missions in contrast to 35 days for Envisat).
7. Besides its significance in identifying the distribution of recent sediments on the terminus of the now-defunct distributaries of the Nile River, the hydrogeological, and agricultural significance of the delineated paleochannels should be investigated. Seepage of surface water to the groundwater system through buried channels/paleochannels that serve as conduits for transferring the surface water has been cited as a potential factor contributing to the rise in groundwater table and waterlogging in agricultural lands in several areas in Egypt where intense irrigation activity utilizing surface water bodies is practiced (Arnous et al., 2015; Behroozmand et al., 2017). Identifying the spatial distribution of paleochannels would be helpful in addressing this problem. The paleochannels that emanate from the Nile Delta and head towards the Eastern and Western Deserts could also represent preferred pathways for groundwater flow that could potentially be used for reclaiming desert lands.

## REFERENCES

- Abdalla, F. A., & Scheytt, T. (2012). Hydrochemistry of surface water and groundwater from a fractured carbonate aquifer in the Helwan area, Egypt. *Journal of Earth System Science*, 121(1), 109–124.  
<https://doi.org/10.1007/s12040-012-0140-7>
- Abdel-Fattah, M. I., & Tawfik, A. Y. (2015). 3D geometric modeling of the Abu Madi reservoirs and its implication on the gas development in Baltim Area (Offshore Nile Delta, Egypt). *International Journal of Geophysics*, 2015, 1-11.  
<https://doi.org/10.1155/2015/369143>
- Abdel-Shafy, H. I., & Kamel, A. H. (2016). Groundwater in Egypt issue: Resources, location, amount, contamination, protection, renewal, future overview. *Egyptian Journal of Chemistry*.
- Abdrabo, M. A., & Hassaan, M. A. (2015). An integrated framework for urban resilience to climate change—Case study: Sea level rise impacts on the Nile Delta coastal urban areas. *Urban Climate*, 14, 554–565.  
<https://doi.org/10.1016/j.uclim.2015.09.005>
- Allam, A. R., Saaf, E. J., & Dawoud, M. A. (2003). Desalination of brackish groundwater in Egypt. *Desalination*, 152(1–3), 19–26.  
[https://doi.org/10.1016/S0011-9164\(02\)01044-5](https://doi.org/10.1016/S0011-9164(02)01044-5)
- Aly, M. H., Klein, A. G., Zebker, H. A., & Giardino, J. R. (2012). Land subsidence in the Nile Delta of Egypt observed by persistent scatterer interferometry. *Remote*

- Sensing Letters, 3(7), 621–630. <https://doi.org/10.1080/01431161.2011.652311>
- Aly, M. H., Zebker, H. A., Giardino, J. R., & Klein, A. G. (2009). Permanent Scatterer investigation of land subsidence in Greater Cairo, Egypt. *Geophysical Journal International*, 178, 1238–1245. <https://doi.org/10.1111/j.1365-246X.2009.04250.x>
- Arabi, N. El. (2012). Environmental Management of Groundwater in Egypt via Artificial Recharge Extending the Practice to Soil Aquifer Treatment ( SAT ). *International Journal of Environment and Sustainability*, 1(3), 66–83. <https://doi.org/10.24102/ijes.v1i3.91>
- Arbouille, D., & Stanley, D. J. (1991). Late Quaternary evolution of the Burullus lagoon region, north-central Nile delta, Egypt. *Marine Geology*, 99(1–2), 45–66. [https://doi.org/10.1016/0025-3227\(91\)90082-F](https://doi.org/10.1016/0025-3227(91)90082-F)
- Arnous, M. O., & Green, D. R. (2015). Monitoring and assessing waterlogged and salt-affected areas in the Eastern Nile Delta region, Egypt, using remotely sensed multi-temporal data and GIS. *Journal of coastal conservation*, 19(3), 369–391.
- Athmania, D., & Achour, H. (2014). External validation of the ASTER GDEM2, GMTED2010 and CGIAR-CSI- SRTM v4.1 free access digital elevation models (DEMs) in Tunisia and Algeria. *Remote Sensing*, 6(5), 4600–4620. <https://doi.org/10.3390/rs6054600>
- Bahgat, G. (2012). The impact of the Arab spring on the oil and gas industry in North Africa—a preliminary assessment. *The Journal of North African Studies*, 17(3), 503–514.



- Ball, J. (1939). Contribution to the Geography of Egypt. Survey and Mines Department, Ministry of Finance Egypt. Government Press, Cairo.
- Bamler, R., & Hartl, P. (1998). Synthetic aperture radar interferometry Synthetic aperture radar interferometry. *Inverse Problems*, 14(4), 55.  
<https://doi.org/10.1088/0266-5611/14/4/001>
- Baynes, T. (1988). Egypt. In *The Encyclopaedia Britannica: a dictionary of arts, sciences, and general literature* (Vol. 7, pp. 705-710)
- Becker, R. H., & Sultan, M. (2009). Land subsidence in the Nile Delta: inferences from radar interferometry. *The Holocene*, 19(6), 949–954.  
<https://doi.org/10.1177/0959683609336558>
- Behroozmand, A., Teatini, P., Bjergsted Pedersen, J., Auken, E., Tosatto, O., & Vest Christiansen, A. (2017). Anthropogenic wetlands due to over-irrigation of desert areas: A challenging hydrogeological investigation with extensive geophysical input from TEM and MRS measurements. *Hydrology and Earth System Sciences*, 21(3), 1527–1545. <https://doi.org/10.5194/hess-21-1527-2017>
- Bekaert, D. P. S., Walters, R. J., Wright, T. J., Hooper, A. J., & Parker, D. J. (2015). Statistical comparison of InSAR tropospheric correction techniques. *Remote Sensing of Environment*, 170, 40–47. <https://doi.org/10.1016/j.rse.2015.08.035>
- Bird, M. I., Fifield, L. K., Chua, S., & Goh, B. (2004). Calculating sediment compaction for radiocarbon dating of intertidal sediments. *Radiocarbon*, 46(1), 421–435. <https://doi.org/10.1017/S0033822200039734>
- Blum, M. D., Tomkin, J. H., Purcell, A., & Lancaster, R. R. (2008). Ups and downs

- of the Mississippi Delta. *Geology*, 36(9), 675–678.  
<https://doi.org/10.1130/G24728A.1>
- Brown, S., & Nicholls, R. J. (2015). Subsidence and human influences in mega deltas: The case of the Ganges-Brahmaputra-Meghna. *Science of the Total Environment*, 527–528, 362–374.  
<https://doi.org/10.1016/j.scitotenv.2015.04.124>
- Buckley, S. M., Rossen, P.A., & Persaud, P. (2000). ROI\_PAC Documentation- Repeat Orbit Interferometry Package. Jet Propulsion Lab., Pasadena, CA.
- Bürgmann, R., Rosen, P. A., & Fielding, E. J. (2000), Synthetic aperture radar interferometry to measure Earth's surface topography and its deformation, *Annu. Rev. Earth Planet. Sci.*, 28, 169–209, doi:10.1146/annurev.earth.28.1.169.
- Carminati, E., & Di Donato, G. (1999). Separating natural and anthropogenic vertical movements in fast subsiding areas: The Po Plain (N. Italy) Case. *Geophysical Research Letters*, 26(15), 2291–2294. <https://doi.org/10.1029/1999GL900518>
- Chan, Y. K., & Koo, V. C. (2008). An introduction to synthetic aperture radar (SAR). *Progress In Electromagnetics Research B*, 2, 27–60.  
<https://doi.org/10.2528/PIERB07110101>
- Chaussard, E., Amelung, F., Abidin, H., & Hong, S. H. (2013). Sinking cities in Indonesia: ALOS PALSAR detects rapid subsidence due to groundwater and gas extraction. *Remote Sensing of Environment*, 128, 150–161.  
<https://doi.org/10.1016/j.rse.2012.10.015>
- Chen, Y., & Xu, H. (2014). Comparisons of Speckle Noise Filtering Methods on

- Interferometric Synthetic Aperture Radar Images. *Journal of Computers*, 9(4), 908–915. <https://doi.org/10.4304/jcp.9.4.908-915>
- Church, J. A., et al. (2013). Sea level change. *Climate Change 2013: The Physical Science Basis. Contribution of Working Group I to the Fifth Assessment Report of the Intergovernmental Panel on Climate Change*, 1137–1216. <https://doi.org/10.1017/CB09781107415315.026>
- CIESIN (Center for International Earth Science Information Network) Columbia University. (2016). Gridded Population of the World, Version 4 (GPWv4): Population Density. Palisades, NY: NASA Socioeconomic Data and Applications Center (SEDAC)[Data file]. Retrieved from <http://dx.doi.org/10.7927/H4NP22DQ>
- Coleman, J. M., & Wright, L. D. (1975). Modern River Deltas: Variability of Processes and Sand Bodies. *Deltas: Models for Exploration*. <https://doi.org/10.1306/C1EA3A50-16C9-11D7-8645000102C1865D>
- Colman, S.M., et al., 2002. Radiocarbon Dating, Chronologic Framework, and Changes in Accumulation Rates of Holocene Estuarine Sediments from Chesapeake Bay. *Quat. Res.* 57, 58–70. doi:10.1006/qres.2001.2285
- Coutellier, V., & Stanley, D. J. (1987). Late Quaternary stratigraphy and paleogeography of the eastern Nile Delta, Egypt. *Marine Geology*, 77(3–4), 257–275. [https://doi.org/10.1016/0025-3227\(87\)90116-2](https://doi.org/10.1016/0025-3227(87)90116-2)
- Dahshan, H., Megahed, A. M., Abd-Elall, A. M. M., Abd-El-Kader, M. A.-G., Nabawy, E., & Elbana, M. H. (2016). Monitoring of pesticides water pollution—

- The Egyptian River Nile. *Journal of Environmental Health Science & Engineering*, 14, 15. <https://doi.org/10.1186/s40201-016-0259-6>
- Dawoud, M. A., Darwish, M. M., & El-Kady, M. M. (2005). GIS-based groundwater management model for Western Nile Delta. *Water Resources Management*, 19(5), 585–604. <https://doi.org/10.1007/s11269-005-5603-z>
- Dawson, R., Hall, J., Sayers, P., Bates, P., & Rosu, C. (2005). Sampling-based flood risk analysis for fluvial dike systems. *Stochastic Environmental Research and Risk Assessment*, 19(6), 388–402. <https://doi.org/10.1007/s00477-005-0010-9>
- Ding, X. L., Li, Z. W., Zhu, J. J., Feng, G. C., & Long, J. P. (2008). Atmospheric effects on InSAR measurements and their mitigation. *Sensors*, 8(9), 5426–5448. <https://doi.org/10.3390/s8095426>
- Dixon, T. H., et al. (2006). Space geodesy: Subsidence and flooding in New Orleans. *Nature*, 441(7093), 587–588. <https://doi.org/10.1038/441587a>
- Dokka, R. K. (2006). Modern-day tectonic subsidence in coastal Louisiana. *Geology*, 34(4), 281–284. <https://doi.org/10.1130/G22264.1>
- Dolson, J. C., Boucher, P. J., Dodd, T., & Ismail, J. (2002). The petroleum potential of the emerging Mediterranean offshore gas plays, Egypt. *The Oil and Gas Journal*, 100(20), 32–37.
- Doornhof, D., Kristiansen, T. G., Nagel, N. B., Pattillo, P. D., & Sayers, C. (2006). Compaction and subsidence. *Oilfield Review*, 18(3), 50–68.
- Driscoll, N. W., & Karner, G. D. (1994). Flexural deformation due to Amazon Fan loading: a feedback mechanism affecting sediment delivery to margins.

- Geology, 22(11), 1015–1018. [https://doi.org/10.1130/0091-7613\(1994\)022<1015:FDDTAF>2.3.CO;2](https://doi.org/10.1130/0091-7613(1994)022<1015:FDDTAF>2.3.CO;2)
- DuMars, A. J. (2002), Distributary Mouth Bar Formation and Channel Bifurcation in the Wax Lake Delta, 88 pp., La. State Univ., Atchafalaya Bay, La.
- ESA (Egyptian Surveying Authority).(1946). Topographic Maps. Scale 1:25,000.Cairo, Egypt: Egyptian Surveying Authority.
- El Bastawesy M, Cherif OH, Sultan M. (2016) The geomorphological evidences of subsidence in the Nile Delta: Analysis of high resolution topographic DEM and multi-temporal satellite images. *Journal of African Earth Sciences* 136:252–261. <https://doi.org/10.1016/j.jafrearsci.2016.10.013>
- El Gamili, M. M., Ibrahim, E. H., Hassaneen, A. R. G., Abdalla, M. A., & Ismael, A. M. (2001). Defunct Nile branches inferred from a geoelectric resistivity survey on Samannud area, Nile Delta, Egypt. *Journal of Archaeological Science*, 28(12), 1339–1348. <https://doi.org/10.1006/jasc.2001.0761>
- El Mahmoudi A, Gabr A. (2008) Geophysical surveys to investigate the relation between the Quaternary Nile channels and the Messinian Nile canyon at East Nile Delta, Egypt. *Arabian Journal of Geosciences* 2(1):53–67. <https://doi.org/10.1007/s12517-008-0018-9>
- El Raey, M. (2011). Mapping areas affected by sea-level rise due to climate change in the Nile delta until 2100. In *Coping with global environmental change, disasters and security* (pp. 773-788). Springer, Berlin, Heidelberg.
- El Tahlawi, M. R., Farrag, A. A., & Ahmed, S. S. (2008). Groundwater of Egypt: “An

- environmental overview”. *Environmental Geology*, 55(3), 639-652.  
<https://doi.org/10.1007/s00254-007-1014-1>
- El-Nahry, A. H., & Doluschitz, R. (2009). Climate change and its impacts on the coastal zone of the Nile Delta, Egypt. *Environmental Earth Sciences*, 59(7), 1497–1506. <https://doi.org/10.1007/s12665-009-0135-0>
- El-Sayed, A.-F. M. (2016). Fish and Fisheries in the Nile Delta. *Hdb Env Chem*, 55, 495–516. <https://doi.org/10.1007/698>
- Elsharkawy, H., Rashed, H. and Rached, I. (2009). Climate Change : The Impacts of Sea Level Rise on Egypt. In: 45th ISOCARP Congress. pp.1-11.
- Erkens, G., Bucx, T., Dam, R., de Lange, G., & Lambert, J. (2015). Sinking coastal cities. *Proceedings of the International Association of Hydrological Sciences*, 372, 189–198. <https://doi.org/10.5194/piahs-372-189-2015>
- Fanos, A. M., Khafagy, A. A., & Dean, R. G. (1995). Protective works on the Nile Delta coast. *Journal of Coastal Research*, 11(2), 516–528.
- FAO (Food and Agriculture Organization of the United Nations). (2002). Multipurpose Landcover Database for Egypt—AFRICOVER. Retrieved from <http://www.fao.org/geonetwork/srv/en/main.home?uuid=ba4526fd-cdbf-4028-a1bd-5a559c4bff38>
- Farr, T. G., et al. (2007). The shuttle radar topography mission. *Reviews of Geophysics*, 45(2). <https://doi.org/10.1029/2005RG000183>
- Faunt, C. C., Sneed, M., Traum, J., & Brandt, J. T. (2016). Water availability and land subsidence in the Central Valley, California, USA. *Hydrogeology Journal*,

- 24(3), 675–684. <https://doi.org/10.1007/s10040-015-1339-x>
- Feng, Q. Y., Liu, G. J., Meng, L., Fu, E. J., Zhang, H. R., & Zhang, K. F.. (2008). Land subsidence induced by groundwater extraction and building damage level assessment - a case study of Datun, China. *Journal of China University of Mining and Technology*, 18(4), 556–560. [https://doi.org/10.1016/S1006-1266\(08\)60293-X](https://doi.org/10.1016/S1006-1266(08)60293-X)
- Ferretti, A., Prati, C., & Rocca, F. (1999). Non-Uniform Motion Monitoring Using the Permanent Scatterers Technique, in: *Second International Workshop on ERS SAR Interferometry, 'FRINGE99'*, Liège, Belgium, 10-12 Nov 1999, pp. 1-6, ESA.
- Ferretti, A., Prati, C., & Rocca, F. (2001). Permanent scatterers in SAR interferometry. *IEEE Transactions on Geoscience and Remote Sensing*, 39(1), 8–20. <https://doi.org/10.1109/36.898661>
- Frihy, O. E. (1988). Nile Delta shoreline changes: Aerial photographic study of a 28-year period. *Journal of Coastal Research*, 4(4), 597–606.
- Frihy, O. E. (2003). The Nile delta-Alexandria coast: Vulnerability to sea-level rise, consequences and adaptation. *Mitigation and Adaptation Strategies for Global Change*, 8(2), 115–138. <https://doi.org/10.1023/A:1026015824714>
- Frihy, O. E. S., Deabes, E. A., Shereet, S. M., & Abdalla, F. A. (2010). Alexandria-Nile Delta coast, Egypt: update and future projection of relative sea-level rise. *Environmental Earth Sciences*, 61(2), 253–273.
- Galloway, W. D. (1975). Process Framework for describing the morphologic and

- stratigraphic evolution of deltaic depositional systems. In *Deltas, Models for Exploration* (pp. 86–98).
- Garello, R. (2010, May). Signal and image processing applications in radar ocean observations. In *Information Sciences Signal Processing and their Applications (ISSPA), 2010 10th International Conference on* (pp. 810-818). IEEE.
- Garthwaite, M. C., Nancarrow, S., Hislop, A., Thankappan, M., Dawson, J. H., & Lawrie, S. (2015). Design of radar corner reflectors for the Australian Geophysical Observing System. *Geoscience Australia*, 3.  
<https://doi.org/10.11636/Record.2015.003>
- Gesch, D., Oimoen, M., Zhang, Z., Meyer, D., & Danielson, J. (2012). Validation of the ASTER global digital elevation model version 2 over the conterminous United States. *International Archives of the Photogrammetry, Remote Sensing and Spatial Information Sciences*, XXXIX(September), 281–286.  
<https://doi.org/10.5194/isprsarchives-XXXIX-B4-281-2012>
- Ghassal, B. I., El Atfy, H., Sachse, V., & Littke, R. (2016). Source rock potential of the Middle Jurassic to Middle Pliocene, onshore Nile Delta Basin, Egypt. *Arabian Journal of Geosciences*, 9(20). <https://doi.org/10.1007/s12517-016-2768-0>
- Hamza, W. (2009). The Nile Delta. *The Nile: Origin, Environments, Limnology and Human Use*, 75–94. [https://doi.org/10.1007/978-1-4020-9726-3\\_5](https://doi.org/10.1007/978-1-4020-9726-3_5)
- Hanssen, R. F. (2001), *Radar Interferometry Data Interpretation and Error Analysis*, 328 pp., Springer, New York.



- Hanssen, R. F., & Van Leijen, F. J. (2008). Monitoring deformation of water defense structures using satellite radar interferometry. In 13th FIG Symposium on Deformation Measurement and Analysis, 4th IAG Symposium on Geodesy for Geotechnical and Structural Engineering (p. 7). Retrieved from [http://www.fig.net/commission6/lisbon\\_2008/papers/ps03/ps03\\_04\\_hanssen\\_mc136.pdf](http://www.fig.net/commission6/lisbon_2008/papers/ps03/ps03_04_hanssen_mc136.pdf)
- Harms, J. C., & Wray, J. L. (1990). Nile Delta. In R. Said (Ed.), *The Geology of Egypt*. Balkema, Rotterdam: Netherlands.
- Hasan, E., Khan, S. I., & Hong, Y. (2015). Investigation of potential sea level rise impact on the Nile Delta, Egypt using digital elevation models. *Environmental Monitoring and Assessment*, 187(10). <https://doi.org/10.1007/s10661-015-4868-9>
- Hefny, K., & Sahta, A. (2004). Underground water in Egypt. Ministry of Water Supplies and Irrigation, Egypt. In *Annual Meeting, Egypt, Commission on Mineral and Thermal Waters, Handouts* (Vol. 25, pp. 11–23).
- Hereher, M.. (2009). Inventory of agricultural land area of Egypt using MODIS data. *Egypt J Remote Sens Space Sci*, 12, 179–184.
- Hereher, M. E. (2010). Vulnerability of the Nile Delta to sea level rise: an assessment using remote sensing. *Geomatics, Natural Hazards and Risk*, 1(4), 315–321. <https://doi.org/10.1080/19475705.2010.516912>
- Hinkel, J., et al. (2014). Coastal flood damage and adaptation costs under 21st century sea-level rise. *Proceedings of the National Academy of Sciences*, 111(9), 3292–

3297. <https://doi.org/10.1073/pnas.1222469111>

Holzer, T. L., & Galloway, D. L. (2005). Impacts of land subsidence caused by withdrawal of underground fluids in the United States. In *Reviews in Engineering Geology XVI: Humans as Geologic Agents* (pp. 87–99). [https://doi.org/10.1130/2005.4016\(08\)](https://doi.org/10.1130/2005.4016(08))

Hooper, A. (2006). Persistent scatterer radar interferometry for crustal deformation studies and modeling of volcano deformation, Ph.D. thesis, Stanford Univ., Stanford, Calif.

Hooper, A., Bekaert, D., Spaans, K., & Arikan, M. (2012). Recent advances in SAR interferometry time series analysis for measuring crustal deformation. *Tectonophysics*, 514, 1–13. <https://doi.org/10.1016/j.tecto.2011.10.013>

Hooper, A., Segall, P., & Zebker, H. (2007). Persistent scatterer interferometric synthetic aperture radar for crustal deformation analysis, with application to Volcán Alcedo, Galápagos. *Journal of Geophysical Research: Solid Earth*, 112(7). <https://doi.org/10.1029/2006JB004763>

Hooper, A., Zebker, H., Segall, P., & Kampes, B. (2004). A new method for measuring deformation on volcanoes and other natural terrains using InSAR persistent scatterers. *Geophysical Research Letters*, 31, L23611.

Hossen, H., & Negm, A. (2016). Change detection in the water bodies of Burullus Lake, northern Nile Delta, Egypt, using RS/GIS. *Procedia Engineering*, 154, 951–958. <https://doi.org/10.1016/j.proeng.2016.07.529>

Hulme, M. (2016). Commentary: 1.5 °C and climate research after the Paris

- Agreement. *Nature Climate Change*, 6(3), 222–224.  
<https://doi.org/10.1038/nclimate2939>
- Hussein, I. M., & Abd-Allah, A. M. A. (2001). Tectonic evolution of the northeastern part of the African continental margin, Egypt. *Journal of African Earth Sciences*, 33(1), 49–68. [https://doi.org/10.1016/S0899-5362\(01\)90090-9](https://doi.org/10.1016/S0899-5362(01)90090-9)
- Jia, H., & Liu, L. (2016). A technical review on persistent scatterer interferometry. *Journal of Modern Transportation*, 24(2), 153–158.  
<https://doi.org/10.1007/s40534-016-0108-4>
- Jung, H. S., Lee, W. J., & Zhang, L. (2014). Theoretical accuracy of along-track displacement measurements from multiple-aperture interferometry (MAI). *Sensors (Switzerland)*, 14(9), 17703–17724. <https://doi.org/10.3390/s140917703>
- Jurkowski, G., Ni, J., & Brown, L. (1984). Modern uparching of the Gulf coastal plain. *Journal of Geophysical Research: Solid Earth*, 89(B7), 6247–6255.
- Kampes, B. (1999). Delft Object-oriented radar interferometric software: User's manual and technical documentation, v4.02 ed.
- Kampes, B. M. (2006). Radar interferometry: Persistent scatterer technique. *Radar Interferometry: Persistent Scatterer Technique (Vol. 12)*. Springer.  
<https://doi.org/10.1007/978-1-4020-4723-7>
- Kang, Y., Zhao, C., Zhang, Q., Lu, Z., & Li, B. (2017). Application of InSAR techniques to an analysis of the Guanling landslide. *Remote Sensing*, 9(10).  
<https://doi.org/10.3390/rs9101046>
- Kassab, M. A., Teama, M. A., Cheadle, B. A., El-Din, E. S., Mohamed, I. F., &

- Mesbah, M. A. (2015). Reservoir characterization of the Lower Abu Madi Formation using core analysis data: El-Wastani gas field, Egypt. *Journal of African Earth Sciences*, 110(OCTOBER), 116–130.  
<https://doi.org/10.1016/j.jafrearsci.2015.06.008>
- Keshta, S., Metwalli, F. J., & Al Arabi, H. S. (2012). Analysis of petroleum system for exploration and risk reduction in abu Madi/Elqar'a gas field, Nile Delta, Egypt. *International Journal of Geophysics*, 2012.  
<https://doi.org/10.1155/2012/187938>
- Klees, R., & Hanssen, R. (2000). Basics of synthetic aperture radar interferometry and applications. *Nordic Geodetic Commission (NKG) Autumn School*, 169-211.
- Leake, S. A. (1990). Interbed storage changes and compaction in models of regional groundwater flow. *Water Resources Research*, 26(9), 1939–1950.  
<https://doi.org/10.1029/WR026i009p01939>
- Li, Z., & Bethel, J. (2008). Image coregistration in SAR interferometry. *Proc. Int. Arch. Photogramm., Remote Sens. Spatial Inf. ...*, XXXVII(B1), 433–438.  
Retrieved from  
[http://www.isprs.org/proceedings/XXXVII/congress/1\\_pdf/72.pdf](http://www.isprs.org/proceedings/XXXVII/congress/1_pdf/72.pdf)
- Li, Z., Zou, W., Ding, X., Chen, Y., & Liu, G. (2004). A quantitative measure for the quality of InSAR interferograms based on phase differences. *Photogrammetric Engineering & Remote Sensing*, 70(10), 1131–1137.
- Liao, M., Jiang, H., Wang, Y., Wang, T., & Zhang, L. (2013). Improved topographic

- mapping through high-resolution SAR interferometry with atmospheric effect removal. *ISPRS Journal of Photogrammetry and Remote Sensing*, 80, 72–79.  
<https://doi.org/10.1016/j.isprsjprs.2013.03.008>
- Likens, G. E. (2010). *River ecosystem ecology: a global perspective*. San Diego: Academic Press.
- Mabrouk, M. B., Jonoski, A., Solomatine, D., & Uhlenbrook, S. (2013). A review of seawater intrusion in the Nile Delta groundwater system—the basis for assessing impacts due to climate changes and water resources development. *Hydrology and Earth System Sciences Discussions*, 10(8), 10873–10911.  
<https://doi.org/10.5194/hessd-10-10873-2013>
- Mahmoud, S. H. (2014). Investigation of rainfall-runoff modeling for Egypt by using remote sensing and GIS integration. *Catena*, 120, 111–121.  
<https://doi.org/10.1016/j.catena.2014.04.011>
- Marriner, N., Flaux, C., Morhange, C., & Kaniewski, D. (2012). Nile Delta’s sinking past: Quantifiable links with Holocene compaction and climate-driven changes in sediment supply? *Geology*, 40(12), 1083–1086.  
<https://doi.org/10.1130/G33209.1>
- Marriner, N., Flaux, C., Morhange, C., & Stanley, J. D. (2013). Tracking Nile Delta vulnerability to Holocene change. *PLoS ONE*, 8(7), E69195 .  
<https://doi.org/10.1371/journal.pone.0069195>
- Mazzotti, S., Lambert, A., Van der Kooij, M., & Mainville, A. (2009). Impact of anthropogenic subsidence on relative sea-level rise in the Fraser River delta.

- Geology, 37(9), 771–774. <https://doi.org/10.1130/G25640A.1>
- Meckel, T. A., Ten Brink, U. S., & Williams, S. J. (2007). Sediment compaction rates and subsidence in deltaic plains: Numerical constraints and stratigraphic influences. *Basin Research*, 19(1), 19–31. <https://doi.org/10.1111/j.1365-2117.2006.00310.x>
- Ministry of Agriculture and Land Reclamation. (2009). Sustainable agricultural development strategy towards 2030. Retrieved from <http://extwprlegs1.fao.org/docs/pdf/egy141040E.pdf>
- Miranda, N., et al. (2013). The ENVISAT ASAR Mission: A look back at 10 years of operation. In *ESA Living Planet Symposium* (Vol. 2013, pp. 1–17).
- Mohamed, R. F., & Hua, C. Z. (2010). Regional groundwater flow modeling in Western Nile Delta, Egypt. *World Rural Observations*, 2(2), 37–42.
- Mohamed, A.-M. S., Radwan, A. M., Sharf, M., Hamimi, Z., Hegazy, E. E., Abou Aly, N., & Gomaa, M. (2016). Evaluation of the deformation parameters of the northern part of Egypt using Global Navigation Satellite System (GNSS). *NRIAG Journal of Astronomy and Geophysics*, 5(1), 65–75. <https://doi.org/http://dx.doi.org/10.1016/j.nrjag.2016.01.001>
- Moreira, A., Prats-Iraola, P., Younis, M., Krieger, G., Hajnsek, I., & Papathanassiou, K. P. (2013). A tutorial on synthetic aperture radar. *IEEE Geoscience and Remote Sensing Magazine*, 1(1), 6–43. <https://doi.org/10.1109/MGRS.2013.2248301>
- Nafaa, M. G., & Frihy, O. E. (1993). Beach and nearshore features along the

- dissipative coastline of the Nile Delta, Egypt. *Journal of Coastal Research*, 9(2), 423–433.
- Negm A.M., Sakr S., Abd-Elaty I., Abd-Elhamid H.F. (2018) An Overview of Groundwater Resources in Nile Delta Aquifer. In: . *The Handbook of Environmental Chemistry*. Springer, Berlin, Heidelberg
- Neumann, J. E., Emanuel, K., Ravela, S., Ludwig, L. C., & Verly, C. (2015). Risks of coastal storm surge and the effect of sea level rise in the Red River Delta, Vietnam. *Sustainability*, 7(6), 6553–6572. <https://doi.org/10.3390/su7066553>
- Nicholls, R. J., & Cazenave, A. (2010). Sea-level rise and its impact on coastal zones. *Science*, 328(5985), 1517–1520. <https://doi.org/10.1126/science.1185782>
- Orton, G. J., & Reading, H. G. (1993). Variability of deltaic processes in terms of sediment supply, with particular emphasis on grain size. *Sedimentology*, 40(3), 475–512. <https://doi.org/10.1111/j.1365-3091.1993.tb01347.x>
- Othman, A., et al. (2018). Use of geophysical and remote sensing data for assessment of aquifer depletion and related land deformation. *Surveys in Geophysics*, pp. 1-24. <https://doi.org/10.1007/s10712-017-9458-7>
- Pavlis, N. K., Holmes, S. A., Kenyon, S. C., & Factor, J. K. (2012). The development and evaluation of the Earth Gravitational Model 2008 (EGM2008). *Journal of Geophysical Research: Solid Earth*, 117(B4).
- Poland, J. F., & Davis, G. H. (1969). Land-surface subsidence due to the withdrawal of fluids. *Reviews in Engineering Geology*, 2, 187–270. <https://doi.org/10.1130/REG2-p187>

- Poscolieri, M., Parcharidis, I., Foumelis, M., & Rafanelli, C. (2011). Ground deformation monitoring in the greater Cairo metropolitan region (Egypt) by SAR interferometry. *Journal of Environmental Semeiotics*, 4(3), 17–45.
- Postma, G. (1995). Sea-level-related architectural trends in coarse-grained delta complexes. *Sedimentary Geology*, 98(1–4), 3–12. [https://doi.org/10.1016/0037-0738\(95\)00024-3](https://doi.org/10.1016/0037-0738(95)00024-3)
- Quintanar J, Khan SD, Fathy MS, Zalat AFA. (2013) Remote sensing, planform, and facies analysis of the Plain of Tineh, Egypt for the remains of the defunct Pelusiac River. *Sedimentary Geology* 297:16–30.  
<https://doi.org/10.1016/j.sedgeo.2013.09.002>
- Rabus, B., Eineder, M., Roth, A., & Bamler, R. (2003). The shuttle radar topography mission—A new class of digital elevation models acquired by spaceborne radar. *ISPRS Journal of Photogrammetry and Remote Sensing*, 57(4), 241–262.  
[https://doi.org/10.1016/S0924-2716\(02\)00124-7](https://doi.org/10.1016/S0924-2716(02)00124-7)
- Raspini, F., Bianchini, S., Ciampalini, A., Del Soldato, M., Solari, L., Novali, F., ... Casagli, N. (2018). Continuous, semi-automatic monitoring of ground deformation using Sentinel-1 satellites. *Scientific Reports*, 8(1).  
<https://doi.org/10.1038/s41598-018-25369-w>
- Riegler, G., Hennig, S. D., & Weber, M. (2015). WorldDEM—A novel global foundation layer. *International Archives of the Photogrammetry, Remote Sensing and Spatial Information Sciences—ISPRS Archives*, 40, 183–187.  
<https://doi.org/10.5194/isprsarchives-XL-3-W2-183-2015>



- RIGW (Research Institute of Groundwater), (1992). Hydrogeological maps of Egypt, scale 1:100,000. Cairo, Egypt: Water Research Center, Ministry of Public Works and Water Resources.
- Rizzini, A., Vezzani, F., Cococchetta, V., & Milad, G. (1978). Stratigraphy and sedimentation of a Neogene-Quaternary section in the Nile Delta area (A.R.E.). *Marine Geology*, 27(3–4), 327–348. [https://doi.org/10.1016/0025-3227\(78\)90038-5](https://doi.org/10.1016/0025-3227(78)90038-5)
- Rizzoli, P., Bräutigam, B., Kraus, T., Martone, M., & Krieger, G. (2012). Relative height error analysis of TanDEM-X elevation data. *ISPRS Journal of Photogrammetry and Remote Sensing*, 73, 30–38. <https://doi.org/10.1016/j.isprsjprs.2012.06.004>
- Roden, J., Abdelsalam, M. G., Atekwana, E., El-Qady, G., & Tarabees, E. A. (2011). Structural influence on the evolution of the pre-Eonile drainage system of southern Egypt: Insights from magnetotelluric and gravity data. *Journal of African Earth Sciences*, 61(5), 358–368. <https://doi.org/10.1016/j.jafrearsci.2011.08.007>
- Rosen, P., Hensley, S., Joughin, I. R., Li, F. K., Madsen, S. N., Rodriguez, E., & Goldstein, R. M. (2000). Synthetic aperture radar interferometry. *Proceedings of the IEEE*, 88(3), 333–382. <https://doi.org/10.1109/5.838084>
- Ross, D. A., Uchupi, E. L. A. Z. A. R., Summerhayes, C. P., Koelsch, D. E., & El Shazly, E. M. (1978). Sedimentation and structure of the Nile Cone and Levant Platform area. *Sedimentation in submarine canyons, fans and trenches:*

- Stroudsborg, Pennsylvania, Dowden, Hutchinson and Ross, 261-274.
- Rowley, R. J., Kostelnick, J. C., Braaten, D., Li, X., & Meisel, J. (2007). Risk of Rising Sea Level to Population and Land Area. *Eos, Transactions American Geophysical Union*, 88(9), 105. <https://doi.org/10.1029/2007EO090001>
- Rzóska J. (1976) The Geological Evolution of the River Nile in Egypt. In: Rzóska J. (eds) *The Nile, Biology of an Ancient River. Monographiae Biologicae*, vol 29. Springer, Dordrecht
- Said, R. (1981). *The geological evolution of River Nile*. New York: Springer-Verlag. <https://doi.org/10.1007/978-1-4612-5841-4>
- Said, R. (1990). *The geology of Egypt*. Rotterdam: A.A.BALKEMA <https://doi.org/10.1017/S0016756800019828>
- Said, R. (1993). *The River Nile: geology, hydrology and utilization*. New York: Pergamon Press.
- Said, R. (2002). Did Nile flooding sink two ancient cities? *Nature*, 415(6867), 37–38. <https://doi.org/10.1038/415037a>
- Saleh, S. (2012). 3D crustal structure and its tectonic implication for Nile Delta and greater Cairo regions, Egypt, from geophysical data. *Geodaetica et Geophysica Hungarica*, 47(4), 402–429.
- Salem, A. M., Ketzer, J. M., Morad, S., Rizk, R. R., & Al-Aasm, I. S. (2005). Diagenesis and Reservoir-Quality Evolution of Incised-Valley Sandstones: Evidence from the Abu Madi Gas Reservoirs (Upper Miocene), the Nile Delta Basin, Egypt. *Journal of Sedimentary Research*, 75(4), 572–584.

<https://doi.org/10.2110/jsr.2005.047>

Shalash, S. (1982). Effects of sedimentation on the storage capacity of the High Aswan Dam reservoir. *Hydrobiologia*, 91(1), 623–639.

<https://doi.org/10.1007/BF00000061>

Shaltout, M., Tonbol, K., & Omstedt, A. (2015). Sea-level change and projected future flooding along the Egyptian Mediterranean coast. *Oceanologia*, 57(4), 293–307. <https://doi.org/10.1016/j.oceano.2015.06.004>

Siegel, F. R., Gupta, N., Shergill, B., Stanley, D. J., & Gerber, C. (1995).

Geochemistry of Holocene sediments from the Nile Delta. *Journal of Coastal Research*, 11(2), 415–431.

Smith, L. C. (2002). Emerging applications of interferometric synthetic aperture radar (InSAR) in geomorphology and hydrology. *Annals of the Association of American Geographers*, 92(3), 385–398. <https://doi.org/10.1111/1467-8306.00295>

Smith, S. E., & Abdel-Kader, A. (1988). Coastal erosion along the Egyptian delta. *Journal of Coastal Research*, 4(2), 245–255.

Sneh A, Weissbrod T. (1973) Nile Delta: The defunct Pelusiac branch identified.

*Science* 180(4081):59–61. <https://doi.org/10.1126/science.180.4081.59>

Sneh, A., Weissbrod, T., Ehrlich, A., Horowitz, A., Moshkovitz, S., & Rosenfeld, A. (1986). Holocene evolution of the northeastern corner of the Nile Delta. *Quaternary Research*, 26(2), 194–206. [https://doi.org/10.1016/0033-5894\(86\)90104-3](https://doi.org/10.1016/0033-5894(86)90104-3)

- Stanley, D. J. (1988). Subsidence in the northeastern Nile Delta: Rapid rates, possible causes, and consequences. *Science*, 240(4851), 497–500.  
<https://doi.org/10.1126/science.240.4851.497>
- Stanley, D. J. (1990). Recent subsidence and northeast tilting of the Nile delta, Egypt. *Marine Geology*, 94(1–2), 147–154. [https://doi.org/10.1016/0025-3227\(90\)90108-V](https://doi.org/10.1016/0025-3227(90)90108-V)
- Stanley, D. J., & Hait, A. K. (2000). Holocene depositional patterns, neotectonics and Sundarban mangroves in the western Ganges-Brahmaputra delta. *Journal of Coastal Research*, 16(1), 26–39. <https://doi.org/10.2307/4300009>
- Stanley, D. J., McRea, J. E., & Waldron, J. C. (1996). Nile Delta drill core and sample database for 1985–1994: Mediterranean Basin (MEDIBA) Program. *Smithsonian Contributions to the Marine Sciences*, (37), 1–428.  
<https://doi.org/10.5479/si.01960768.37.1>
- Stanley, D. J., & Warne, A. G. (1993). Nile Delta: Recent geological evolution and human impact. *Science*, 260(5108), 628–634.  
<https://doi.org/10.1126/science.260.5108.628>
- Stanley, D. J., & Warne, A. G. (1994). Worldwide initiation of Holocene marine deltas by deceleration of sea-level rise. *Science*, 265(5169), 228–231.  
<https://doi.org/10.1126/science.265.5169.228>
- Stanley, J. (2003). Nile Delta margin : failed and fluidized deposits concentrated along distributary channels. *Géomorphologie: Relief, Processus, Environnement*, 9(4), 211–226.

- Stanley, J.-D. (1997). Mediterranean deltas: subsidence as a major control of relative sea-level rise. *Bulletin de l'Institut Océanographique Monaco, Science Series*, 3, 35–62. Retrieved from [https://repository.si.edu/bitstream/handle/10088/7447/JD\\_stanley\\_2.pdf?sequence=1](https://repository.si.edu/bitstream/handle/10088/7447/JD_stanley_2.pdf?sequence=1)
- Stanley, J.-D. (2005). Submergence and burial of ancient coastal sites on the subsiding Nile Delta margin, Egypt. *Méditerranée*, 104(104), 65–73. <https://doi.org/10.4000/mediterranee.2282>
- Stanley JD, Clemente PL. (2014) Mica and Heavy Minerals as Markers to Map Nile Delta Coastline Displacements during the Holocene. *Journal of Coastal Research* 297(5):904–921. <https://doi.org/10.2112/JCOASTRES-D-14A-00003.1>
- Stanley, J. D., & Clemente, P. L. (2017). Increased land subsidence and sea-level rise are submerging Egypt's Nile Delta coastal margin. *GSA Today*, 27(5), 4–11. <https://doi.org/10.1130/GSATG312A.1>
- Stanley JD, Jorstad TF. (2006) Short contribution: Buried Canopic channel identified near Egypt's Nile delta coast with radar (SRTM) imagery. *Geoarchaeology* 21(5):503–514. <https://doi.org/10.1002/gea.20117>
- Stanley, J.-D., Warne, A. G., & Schnepf, G. (2004). Geoarchaeological Interpretation of the Canopic, Largest of the Relict Nile Delta Distributaries, Egypt. *Journal of Coastal Research*, 20(3), 920–930. [https://doi.org/10.2112/1551-5036\(2004\)20\[920:GIOTCL\]2.0.CO;2](https://doi.org/10.2112/1551-5036(2004)20[920:GIOTCL]2.0.CO;2)
- Strzepek, K. M. (1995). As climate changes: international impacts and implications.

Cambridge: Cambridge University Press.

Syvitski, J. P. M. (2008). Deltas at risk. *Sustainability Science*, 3, 23–32.

<https://doi.org/10.1007/s11625-008-0043-3>

Syvitski, J. P. M., et al. (2009). Sinking deltas due to human activities. *Nature*

*Geoscience*, 2(10), 681–686. <https://doi.org/10.1038/ngeo629>

Syvitski, J. P. M., Vörösmarty, C. J., Kettner, A. J., & Green, P. (2005). Impact of humans on the flux of terrestrial sediment to the global coastal ocean. *Science*,

308(5720), 376–380. <https://doi.org/10.1126/science.1109454>

Tachikawa, T., et al. (2011). ASTER global digital elevation model version 2-

summary of validation results. NASA, 27 pp. Retrieved from

[http://www.jspacesystems.or.jp/ersdac/GDEM/ver2Validation/Summary\\_GDEM2\\_validation\\_report\\_final.pdf](http://www.jspacesystems.or.jp/ersdac/GDEM/ver2Validation/Summary_GDEM2_validation_report_final.pdf)

Taniguchi, M., & Holman, I. (Eds.). (2010). Groundwater response to a changing

climate. New York: CRC Press.

Tawadros, E.E. (2012) *Geology of North Africa*. CRC Press/Balkema, Taylor &

Francis Group, London, UK, 952 pp.

Teatini, P., Tosi, L., & Strozzi, T. (2011). Quantitative evidence that compaction of

Holocene sediments drives the present land subsidence of the Po Delta, Italy.

*Journal of Geophysical Research: Solid Earth*, 116(8).

<https://doi.org/10.1029/2010JB008122>

Törnqvist, T. E., et al. (2008). Mississippi Delta subsidence primarily caused by

compaction of Holocene strata. *Nature Geoscience*, 1(3), 173–176.

<https://doi.org/10.1038/ngeo129>

Toussoun, O. (1922). Mémoire sur les anciennes branches du Nil. l'Institut français d'archéologie orientale.

UNAVCO. (2018). Synthetic Aperture Radar (SAR) Satellites | Instrumentation | UNAVCO. Retrieved October 5, 2018, from <https://www.unavco.org/instrumentation/geophysical/imaging/sar-satellites/sar-satellites.html>

U.S. Energy Information Administration. (2014). International Energy Statistics. Retrieved from [https://www.eia.gov/beta/international/data/browser/#/?pa=g&c=00000000000001&ct=0&tl\\_id=3002-A&vs=INTL.3-1-EGY-BCF.A&vo=0&v=H&start=1990&end=2014](https://www.eia.gov/beta/international/data/browser/#/?pa=g&c=00000000000001&ct=0&tl_id=3002-A&vs=INTL.3-1-EGY-BCF.A&vo=0&v=H&start=1990&end=2014)

van de Sande, B., Lansen, J., & Hoyng, C. (2012). Sensitivity of coastal flood risk assessments to digital elevation models. *Water*, 4(4), 568–579. <https://doi.org/10.3390/w4030568>

Van Hooidek, R., Maynard, J. a., & Planes, S. (2013). Temporary refugia for coral reefs in a warming world. *Nature Climate Change*, 3(5), 508–511. <https://doi.org/10.1038/nclimate1829>

Wadge, G., Webley, P. W., James, I. N., Bingley, R., Dodson, A., Waugh, S., ... Clarke, P. J. (2002). Atmospheric models, GPS and InSAR measurements of the tropospheric water vapour field over Mount Etna. *Geophysical Research Letters*, 29(19), 11-1-11–4. <https://doi.org/10.1029/2002GL015159>

- Walcott, R. I. (1972). Gravity, flexure, and the growth of sedimentary basins at a continental edge. *Geological Society of America Bulletin*, 83(6), 1845–1848.
- Waltham, T. (2002). Sinking cities. *Geology Today*, 18(3), 95–100.  
<https://doi.org/10.1046/j.1365-2451.2002.00341.x>
- War Office. (1941). Alexandria, Egypt: Scale 1:100000. London: War Office.
- Warne, A. G., & Stanley, D. J. (1993). Archaeology to refine Holocene subsidence rates along the Nile Delta margin, Egypt. *Geology*. [https://doi.org/10.1130/0091-7613\(1993\)021<0715:ATRHSR>2.3.CO;2](https://doi.org/10.1130/0091-7613(1993)021<0715:ATRHSR>2.3.CO;2)
- Watts, A. B. (2001). *Isostasy and flexure of the lithosphere*. Cambridge: Cambridge University Press.
- World Bank. (2017). Population of Egypt. Retrieved from  
<https://data.worldbank.org/indicator/SP.POP.TOTL?locations=EG&page=2>
- Wright, L. D., & Coleman, J. M. (1973). Variations in morphology of major river deltas as functions of ocean wave and river discharge regimes. *American Association of Petroleum Geologists Bulletin*, 57(2), 370-398.  
<https://doi.org/10.1306/819A4274-16C5-11D7-8645000102C1865D>
- Xu, W., Dutta, R., & Jónsson, S. (2015). Identifying active faults by improving earthquake locations with InSAR data and Bayesian estimation: The 2004 Tabuk (Saudi Arabia) earthquake sequence. *Bulletin of the Seismological Society of America*, 105(2), 765–775. <https://doi.org/10.1785/0120140289>
- Yhokha, A., Chang, C. P., Goswami, P. K., Yen, J. Y., & Lee, S. I. (2015). Surface deformation in the Himalaya and adjoining piedmont zone of the Ganga Plain,



- Uttarakhand, India: Determined by different radar interferometric techniques.  
Journal of Asian Earth Sciences, 106, 119–129.  
<https://doi.org/10.1016/j.jseaes.2015.02.032>
- Younes, M. A.-A. (2015). Natural gas geochemistry in the offshore Nile Delta, Egypt.  
In Advances in Petrochemicals. <https://doi.org/10.5772/60575>
- Yun, S. H., Zebker, H., Segall, P., Hooper, A., & Poland, M. (2007). Interferogram  
formation in the presence of complex and large deformation. Geophysical  
Research Letters, 34(12). <https://doi.org/10.1029/2007GL029745>
- Yun, Y., Zeng, Q., Green, B. W., & Zhang, F. (2015). Mitigating atmospheric effects  
in InSAR measurements through high-resolution data assimilation and numerical  
simulations with a weather prediction model. International Journal of Remote  
Sensing, 36(8), 2129–2147. <https://doi.org/10.1080/01431161.2015.1034894>
- Zaid, S. M., Mamoun, M. M., & Al-Mobark, N. M. (2014). Vulnerability assessment  
of the impact of sea level rise and land subsidence on north Nile Delta region.  
World Applied Sciences Journal, 32(3), 325-342.  
<https://doi.org/10.5829/idosi.wasj.2014.32.03.14505>
- Zebker, H. A., & Villasenor, J. (1992). Decorrelation in interferometric radar echoes.  
IEEE Transactions on Geoscience and Remote Sensing, 30(5), 950–959.  
<https://doi.org/10.1109/36.175330>
- Zhou, X., Chang, N.-B., & Li, S. (2009). Applications of SAR Interferometry in Earth  
and Environmental Science Research. Sensors, 9(3), 1876–1912.  
<https://doi.org/10.3390/s90301876>

Zou, W., Li, Y., Li, Z., & Ding, X. (2009). Improvement of the accuracy of InSAR image co-registration based on tie points - A review. *Sensors*, 9(2), 1259–1281.  
<https://doi.org/10.3390/s90201259>